UNIVERSITÀ DEGLI STUDI DI PALERMO

PhD in Mechanical, Manufacturing, Management and Aerospace Innovation

New components and turbofans for green aviation

A thesis presented for the degree of
Doctor of Philosophy

PhD Candidate:
Pierantonio Lo Greco

Tutor:
Prof. Emiliano Pipitone

Co-Tutor:
Prof. Giuseppe Lombardo

Academic Years 2022 / 2024

Contents

1 Nomenclature

A_{pre} = pre-exponential factor
A = engine section area $[m^2]$
AFR = air-to-fuel ratio $[adim]$
BI = branching index
c_p = air specific heat at constant pressure $\left[\frac{\mathrm{J}}{\mathrm{K \cdot Kg}}\right]$
c'_p = combustion gasses specific heat at constant pressure $\left[\frac{\mathrm{J}}{\mathrm{K \cdot Kg}}\right]$
DZ = dilution zone
E_a = activation energy $[\frac{Kcal}{mol}]$
EI = emission index
f = fuel flow to core airflow ratio [adim]
F = thrust [N]
$fact_{scal}$ = map scaling factor [adim]
$GHSV$ = gas hourly space velocity $[h^{-1}]$
H_i = fuel lower heating value $\left[\frac{\mathrm{J}}{\mathrm{Kg}}\right]$
ID = dataset point number
k = iteration variable in scaling factor algorithm [adim]
$\dot{m}$ = mass flow rate $\left[\frac{\mathrm{Kg}}{\mathrm{s}}\right]$
Ma_0 = flight Mach number [adim]
Ma = Mach number [adim]
N = corrected rpm [rpm]
N' = shaft rpm [rpm]
n = temperature exponent $[adim]$
P = pressure $[Pa]$
P_i = static pressure at section i [Pa]
P_{ti} = stagnation pressure at section i [Pa]
PZ = primary combustion zone
PAH = polycyclic aromatic hydrocarbons
PSR = perfectly stirred reactor
PFR = plug flow reactor
R' = combustion gasses specific constant $\left[\frac{\mathrm{J}}{\mathrm{K \cdot Kg}}\right]$
RN = reactor network
SAC = single annular combustor
SZ = secondary combustion zone
SAF = sustainable aviation fuels
SMD = Sauter mean diameter $[m]$
t = residence time $[msec]$
T = temperature $[K]$
T_i = static temperature at section i [K]
T_{ti} = stagnation temperature at section i [K]
$TSFC$ = thrust specific fuel consumption $[\frac{N}{Kg \cdot h}]$
v = velocity $[\frac{m}{s}]$
VPF = variable pitch fan
W = corrected mass flow $\left[\frac{\mathrm{Kg}}{\mathrm{s}}\right]$

Y_i = mass fraction i-th specie [m]
z = flight altitude [m]
α = bypass ratio [adim]
γ = ratio between c_p and c_v of air [adim]
γ' = ratio between c_p and c_v of combustion gasses [adim]
η = adiabatic efficiency [adim]
η_{mech} = mechanical efficiency [adim]
θ = fan pitch angle [°]
θ_{NH_3} = fraction of catalyst sites occupied by NH_3 [adim]
π = total pressure ratio [adim]
τ = total temperature ratio [adim]
ρ_i = density at section i $\left[\frac{Kg}{m^3}\right]$
μ = dynamic viscosity $\left[\frac{Pa}{s}\right]$
ϕ = equivalence ratio [$adim$]

Subscripts

b = burner
byp = bypass nozzle
c = compressor
cat = catalyst
$core$ = core flow
$comb$ = combustor inlet
$cool$ = combustor cooling air
d = diffuser
DZ = combustor dilution air
e = core nozzle
f = fan
$fuel$ = fuel
HP = high pressure
$HPcompr$ = high pressure compressor
$inlet$ = catalyst inlet
LP = low pressure
$LPcompr$ = low pressure compressor
map = value referred to unscaled/original map
$outlet$ = catalyst outlet
pr = value referred to preliminary design phase
PZ = combustor primary air
t = stagnation properties
tHP = high pressure turbine
tLP = low pressure turbine
tot = intake flow
SZ = combustor secondary air
SVF = soot volume fraction

2 Introduction

The aviation industry plays a pivotal role in the global economy, facilitating the movement of people, goods, and services across vast distances. As air travel continues to grow, however, it also faces increasing scrutiny due to its environmental impact, particularly in relation to carbon emissions and fuel consumption. Among the critical factors driving this concern are the performance and emissions characteristics of turbofan engines, which are the heart of modern civil aviation propulsion systems. To address these challenges, there is an urgent need to develop innovative approaches for optimizing engine efficiency while minimizing harmful emissions. One approach that is increasingly used today is computational modeling and simulation of individual components or the entire propulsion apparatus.

In recent years, the aerospace industry has witnessed significant advancements in computational modeling and simulation technologies. These innovations have provided unprecedented opportunities to better understand and predict the complex behaviors of turbofan engines under varying operational conditions. Traditional methods for assessing engine performance and emissions have often been limited by empirical data and simplified assumptions, which do not fully capture the intricate dynamics of engine operation. However, with the advent of more sophisticated simulation models, researchers can now explore new avenues for improving engine design, fuel efficiency, and environmental sustainability.

The next generation turbofan models should allow the integration of innovative components in order to assess their impact on overall performance and emission levels. This simulation technique could significantly reduce the production costs of future engine components as it would first allow real impact assessment and component optimization at an early stage. The approach would also ensure a reduction in prototyping time. In order to be integrated into the model, components should be tested in virtual environments under suitable operating conditions. This would allow to obtain maps for each component. Maps are essentially relationships between several variables that describe the behavior of the component itself, and are used as inputs for turbofan simulation models.

Among the most interesting components for future integration in modern turbofans is certainly the variable pitch fan (VPF). The VPF has emerged as a promising innovation in turbofan engine design, offering the potential for enhanced performance and efficiency across a wide range of operating conditions. By adjusting the fan blade angle during flight, the VPF enables optimized thrust and fuel consumption, making it particularly beneficial for varying mission profiles. However, the adoption of VPF technology is not without its drawbacks. The most significant concern is the increased mechanical complexity introduced by the variable pitch mechanism, which involves additional moving parts that may increase the likelihood of mechanical failure and necessitate more frequent maintenance. These added components also contribute to a weight penalty, which can affect overall engine performance and aircraft efficiency. Moreover, the integration of VPF systems into existing engine designs presents engineering challenges, often requiring substantial redesigns and additional development costs.

Much of this thesis deals with the construction of an innovative turbofan model where the components can be represented by maps, non-linear equations or through neural, which can be trained from fluid dynamic simulations data. The thesis also proposes an efficient computational method for constructing VPF maps.

The growing environmental concerns associated with aviation emissions have driven significant efforts to reduce nitrogen oxides (NOx) released by turbofan engines. One promising

solution is the integration of Selective Catalytic Reduction (SCR) technology, widely used in automotive and industrial applications, for NOx reduction in turbofan engines. The potential use of SCR catalysts in aviation could offer a significant improvement in emission control, aligning with stringent environmental regulations and the industry's sustainability goals.

This thesis also explores the feasibility, challenges, and benefits of implementing SCR technology in modern turbofan engines for $DeNOx$ and proposed a possible turbofan catalyst design. The scope is to evaluate catalyst $DeNOx$ performance and its impact on engine performance and fuel consumption.

In Section 3, we present an effective method for developing numerical turbofan models that allows reliable steady-state turbofan performance calculations. The main difference between the proposed method and those used in various commercial algorithms, such as GasTurb, GSP 12 and NPSS, is the use of neural networks as a multidimensional interpolation method for rotational component maps instead of classical β parameter. An additional aspect of fundamental importance lies in the simplicity of implementing this method in Matlab and the high degree of customization of the turbofan components without performing any manipulation of variables for the purpose of reducing the dimensionality of the problem, which would normally lead to a high condition number of the Jacobian matrix associated with the nonlinear turbofan system (and, thus, to significant error). In the proposed methodology, the component behavior can be modeled by analytical relationships and through the use of neural networks trained from component bench test data or data obtained from CFD simulations. Generalization of rotational component maps by feedforward neural networks leads to an average interpolation error up to around 1%, for all variables. The resulting nonlinear system is solved by a combined genetic algorithm and least squares algorithm approach, instead of the standard Newton's method. The turbofan numerical model turns out to be convergent, and results suggest that the trend in overall turbofan performance, as flight conditions change, is in agreement with the outputs of the GSP 12 software.

Section 4 presents a suitable method for generating maps of variable pitch fans (VPFs) under symmetric flight conditions. This method is widely validated in the literature and also allows to simulate the presence of a possible stator, thus leading to a higher degree of accuracy in computing the maps. Unlike conventional fan maps, which are described by a set total of 4 variables, VPFs maps require a fifth variable, known as the variable pitch angle. The VPF map generated by the techniques outlined in Section 4 can thus be used in the turbofan model proposed in Section 3. This would allow to evaluate the impact of VPF, and specifically its geometric characteristics, on turbofan performance. Section 4 also briefly explains the possible advantages and disadvantages of VPFs.

The turbofan performance model is complemented by a new emissions estimation model that can correctly represent the behavior of conventional fuels and sustainable aviation fuels (SAFs). Specifically, the performance model provides part of the inputs (such as temperatures, pressures, and gas velocities) needed by the emissions model. Two different emission estimation models are developed in this thesis. The main difference between the 2 emission models lies in the level of detail of the fluid-dynamic/kinetic modeling of the combustion chamber, which plays a predominant role in determining the quantity and types of pollutants.

The Section 5 presents the first emission model. The model is built starting from literature references and qualitative considerations on single annular combustor computational fluid dynamics data. These observations enabled the construction of a network of 0-D and 1-D reactors, which mimics the behavior of combustor, turbines, and nozzle. The SAFs have

the potential to replace conventional petroleum derived fuels in long-haul flights. However, SAF chemical composition varies considerably with feedstock and production processes, which subsequently impacts combustion properties and emissions. Such variation in properties makes it necessary to use a kinetic model that can model different fuel compositions. Therefore in the present thesis, we utilize a functional group approach (*i.e.*, FGMech, Zhang and Sarathy 2021) to develop simplified kinetic mechanisms for conventional JP-8 and SAF produced by hydrotreating of fatty acids (HEFA) from camelina (CAM) oil. FGMech, which provides a lumped kinetic mechanism for fuel oxidation, was then combined with a base mechanism, a PAH mechanism, and nitrogen and sulfur chemistry, forming a complete gas-phase model. The base mechanism was selected from several literature models based on the simulation results compared to experimental data of important PAH precursors. The resulting kinetic model was applied to simulate emissions of a turbofan, with special emphasis on CO, NO_x, SO_x and soot. The predictions by the emission model were compared with experimental measurements from NASA APEX (Wey *et al.* 2006) and ACCESS (Moore *et al.* 2017) campaigns. For all the operating conditions, the results show that the emission model succeeds in accurately predicting the concentrations of most species tested. The model shows a reduction in soot emission index for CAM-HEFA, compared to JP-8, that is close to experimental data.

The Section 6 presents the second emission model. Unlike the first emission model, the second one is constructed partially using data derived from fluid dynamic simulations of the combustor. This model should accurately represent both fluido-dynamics and combustion chemical kinetics of the burner, turbine, and nozzle. The temperature and velocity fields are obtained from accurate CFD simulations performed with real combustor geometry using a single-step combustion kinetic mechanism. The fluido-dynamic domain of the combustor is first divided into multiple zones of homogeneous temperature and velocity, and then converted into a reactor network consisting of perfectly stirred reactors. The turbines and nozzles are represented by plug flow reactors. The model is validated using experimental data obtained from NASA's APEX test campaign. The results show that the model can accurately predict the molar concentrations of more than 10 pollutant species. This simulation approach allows to greatly decrease the computational effort while still maintaining detailed chemical kinetics.

The Section 7 discusses the possible architecture of a turbofan catalyst that can reduce the concentration of NO_x in the exhaust gas. The NO_x are of particular importance as they are highly damaging to human health and to ecosystems. The problem of NO_x is also becoming more pressing because of the gradual shift toward turbofans with increasingly high-performance cores, which demand higher pressures and temperatures in the combustion chamber. At present there are no effective solutions in counteracting the formation of such agents other than reducing the combustion temperature or acting on the burner design in order to reduce the formation of high temperature pockets: such solutions can cause a general drop in performance and an increase in CO_x emissions. This thesis addresses the NO_x abatement problem in a turbofan through the use of a catalyst with an innovative design, placed between the LP turbine and the core nozzle. The problem of realizing a reliable catalyst equipped turbofan simulation is solved through a recursive algorithm in which a nonlinear turbofan model built in GSP 12 turbine program interacts with an Ansys Fluent catalyst model. Results show that, for an integrated fuselage engine, the use of such a solution generally leads to a small reduction in thrust (less than 5%) and NO_x reduction (around 90%) but its applicability remains limited to near cruise condition due to $Cu-ZSM5$ catalyst

temperature constrains.

3 Non linear turbofan model

The need to develop more efficient and environmentally friendly engines is driven, on the one hand, by the trend of more stringent green regulations [1], with the EU as a pioneer in this field [2], and, on the other hand, by increasing fuel cost. Such a class of engines will use new, sophisticated, highly efficient components with operative behaviors that are significantly different from the standard components currently in use. In this scenario, new computational models, oriented to assist the design and test of new components, are of fundamental importance. Turbofan simulations have become more and more reliable and feasible over time due to the continuous increase in computing power and an increasingly multidisciplinary approach to the subjects involved, such as aerodynamics, acoustics, combustion, and materials [3]. In this thesis, we present a new effective numerical method that allows reliable steady-state turbofan performance calculations in which components are operated, generalizing the component maps data using artificial neural networks (ANNs). One of the main differences between the proposed method and the one used in various commercial algorithms, such as GSP 12 [4] and NPSS [5], is the absence of the β parameter (GSP 12) or linear piecewise (NPSS) interpolation for the interpolation of fan, compressor, and turbine maps (Table 1). The β parameter is used, in most of the formulations, as an interpolation method in gas turbine simulation programs as it allows the identification of the operating point from only two parameters (β,N) instead of four (fixed-geometry component) or five (variable-geometry components) (N,W or WN,π,η,δ), thus avoiding problems of convergence and accuracy [6]. In the case of a compressor, the linear variant of beta interpolation involves first defining a beam, more or less dense depending on the degree of accuracy required, of parallel lines (each defined by a value of β) to the surge line and then calculating the points of intersection of each of these lines with each curve at constant corrected speed. Such an intersection point identifies, from the *beta*/N coordinate pair, the corresponding values of corrected flow rate, pressure ratio, and efficiency (W, π, η). Finally, a 2D linear or higher-order interpolation is applied. In the actual implementation of the method, β interpolation was replaced by implicit equations derived by using neural networks, which were trained from four experimental datasets (associated with variables N,W or WN,π,η) divided into two sets of input data and two sets of output data. This technique can also be used to model, by ANN, any component, other than turbines or compressors, for which we have sufficient experimental or numerical data associated with the variables describing their operation. Modeling real components using maps requires a large amount of experimental data, which could have some economic and time impact: for this reason, in the present thesis, we open the possibility of performing a limited number of experimental tests (from the GSP 12 map database), which are interpolated using piecewise functions, thus allowing the identification of intermediate operating points between two experimentally detected operating points. A further relevant aspect of such a turbofan model is the possibility of adding/removing components by simply adding/removing the respective equations describing its operation (see Section 3.1.1): a model being made up of a large number of variables (more than 40) could lead to a high condition number of the Jacobian matrix associated with the system of nonlinear equations (and, thus, a significant error). However, thanks to the scaling mode introduced (in Section 3.1.8)), such errors are significantly contained and results are in good agreement with GSP 12 outputs. The proposed model uses an heuristic method (genetic algorithm, GA) combined with a gradient method (least squares, LSQ) in order to solve the turbofan problem whose components are represented by nonlinear equations or maps (Table 1). Such a combined

approach allows the mitigation of the disadvantages of both individual methods: the LSQ needs an initial guess solution close to the actual solution and has a high convergence speed, while, in contrast, the GA does not need any initial guess, but only the definition of upper and lower boundary for the solution, and has a significantly lower convergence speed [7]. The combined approach, thus, makes it possible to obtain a robust iterative algorithm with good convergence and precision. These properties are even more important when the turbofan considered is assembled with unconventional/innovative components, which makes the choice of an appropriate initial guess solution even more uncertain, moving it significantly away from that of a more conventional turbofan. Thus, the turbofan modeling method developed here can serve as a basis to simulate advanced and innovative components, such as ultra-high-bypass fans, advanced burners, variable-geometry compressors, and cooled turbines.

Table 1: Comparison between turbine simulation algorithms.

Code	**Solver**	**Interpolation Meth.**
Proposed	GA + LSQ	ANN
GSP 12	Newton Raphson	β
NPSS	Newton Raphson	linear piecewise

3.1 Methods

In Section 3.1.1, we first introduce the nonlinear equations system used for modeling the turbofan and propose equations for the rotating components obtained by feedforward neural networks. We then choose the Rolls-Royce Trent 1000 as the reference turbofan to run the off-design performance simulation and give performances in the cruise condition, which are used as input parameters for the present model (Section 3.1.2). However, unlike the classic two-spool engine architecture, in this thesis, in order to reduce the complexity a little in the implementation of the code, we opted for a configuration in which the LP turbine drives the fan only (instead of fan + LP compressor). Next, we briefly present the theoretical concepts behind genetic algorithms, least square method (Section 3.1.3), feedforward neural networks (Section 3.1.4), and their actual use in Matlab via built-in solvers. In Section 3.1.5, we highlight the parameters of population size, max generation, and crossover fraction necessary for the operation of the genetic algorithm solver and provide, for both solvers, a common expression for the objective function (fun_{obj}) whose minimization allows the performance of the turbofan to be derived. In Section 3.1.6, we illustrate the reasons behind the choice of the feedforward neural network as the network for modeling the fan, compressor, and turbine, along with a brief explanation of the training methods, the choice of the number of layers/neurons, and the performance (as measured by the MSE, mean square error) of the networks. In Section 3.1.7, we introduce an overall algorithm for calculating turbofan performance, which uses the elements illustrated in the previous sections: this algorithm is divided, for ease of understanding, into three functional blocks, which perform well-defined tasks. Finally, in Section 3.1.8, we illustrate the scaling algorithm, which provides scaling factors for the rotating component maps and a guess solution to initialize the performance calculation algorithm.

3.1.1 Turbofan Nonlinear Equations System

The turbofan model (Fig. 1), adopted as example, consists of a system of 44 nonlinear equations in 44 unknowns. These equations represent the thermodynamic model of each turbofan component in addition to other equations derived from matching relations regarding the power balances of the HP and LP shafts as well as the equality of rotation speeds of the fan and LP turbine, and the compressor and HP turbine.

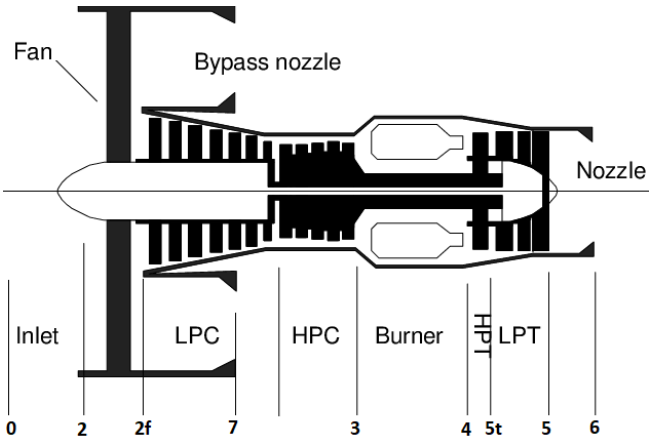

Figure 1: Turbofan main components [8].

The air intake was modeled as an adiabatic component with viscous losses defined by π_{int} (Equation (1)).

$$\begin{cases} T_{t2} = T_{t0} = T_0 \left(1 + \dfrac{\gamma - 1}{2} Ma_0^2\right) \\ P_{t2} = \pi_{int} P_{t0} = \pi_{int} P_0 \left(1 + \dfrac{\gamma - 1}{2} Ma_0^2\right)^{\frac{\gamma}{\gamma - 1}} \end{cases} \tag{1}$$

Each rotating component is described by means of two implicit relations appropriately scaled by a factor $fact_{scal}$ (see Section 3.1.8), obtained from feedforward neural networks training, in particular Equations (2) and (3) for the fan and compressor [9], and Equations (4) and (5) for the turbine (where WN is the product of the correct flow rate and the correct rpm value).

$$\begin{cases} \dfrac{W}{fact_{scal_W}} = f_{1_c}\left(\dfrac{N}{fact_{scal_N}}, \dfrac{\pi}{fact_{scal_\pi}}\right) \\ \dfrac{\eta}{fact_{scal_\eta}} = f_{2_c}\left(\dfrac{N}{fact_{scal_N}}, \dfrac{\pi}{fact_{scal_\pi}}\right) \end{cases} \tag{2}$$

$$\begin{cases} \dfrac{W}{fact_{scal_W}} = f_{1_f}\left(\dfrac{N}{fact_{scal_N}}, \dfrac{\pi}{fact_{scal_\pi}}\right) \\ \dfrac{\eta}{fact_{scal_\eta}} = f_{2_f}\left(\dfrac{N}{fact_{scal_N}}, \dfrac{\pi}{fact_{scal_\pi}}\right) \end{cases} \tag{3}$$

$$\begin{cases} \dfrac{N}{fact_{scal_N}} = f_{1_{tHP}}\left(\dfrac{WN}{fact_{scal_{WN}}}, \dfrac{\pi}{fact_{scal_\pi}}\right) \\ \dfrac{\eta}{fact_{scal_\eta}} = f_{2_{tHP}}\left(\dfrac{WN}{fact_{scal_{WN}}}, \dfrac{\pi}{fact_{scal_\pi}}\right) \end{cases} \tag{4}$$

$$\begin{cases} \dfrac{N}{fact_{scal_N}} = f_{1_{tLP}}\left(\dfrac{WN}{fact_{scal_{WN}}}, \dfrac{\pi}{fact_{scal_\pi}}\right) \\ \dfrac{\eta}{fact_{scal_\eta}} = f_{2_{tLP}}\left(\dfrac{WN}{fact_{scal_{WN}}}, \dfrac{\pi}{fact_{scal_\pi}}\right) \end{cases} \tag{5}$$

The adiabatic modeling and the total pressure relations were also applied to the fan (Equation (6)), compressor (Equation (7)), HP turbine (Equation (8)), and LP turbine (Equation (9)).

$$\begin{cases} T_{t2f} = \left[1 + \dfrac{1}{\eta_f}\left(\pi_f^{\frac{\gamma-1}{\gamma}} - 1\right)\right] T_{t2} \\ P_{t2f} = \pi_f P_{t2} \end{cases} \tag{6}$$

$$\begin{cases} T_{t3} = \left[1 + \dfrac{1}{\eta_c}\left(\pi_c^{\frac{\gamma-1}{\gamma}} - 1\right)\right] T_{t2} \\ P_{t3} = \pi_c P_{t2} \end{cases} \tag{7}$$

$$\begin{cases} P_{t5t} = \dfrac{P_{t4}}{\pi_{t_{HP}}} \\ T_{t5t} = T_{t4}\left[1 - \eta_{t_{HP}}\left(1 - \pi_{t_{HP}}^{\frac{1-\gamma'}{\gamma'}}\right)\right] \end{cases} \tag{8}$$

$$\begin{cases} P_{t5} = \dfrac{P_{t5t}}{\pi_{t_{LP}}} \\ T_{t5} = T_{t5t}\left[1 - \eta_{t_{LP}}\left(1 - \pi_{t_{LP}}^{\frac{1-\gamma'}{\gamma'}}\right)\right] \end{cases} \tag{9}$$

Further equations relate to the compressor–HP turbine (Equation (10)) and fan–LP turbine mass flow balance (Equation (11)), the compressor–HP turbine (Equation (12)) and fan–LP turbine power balance (Equation (13)), the compressor-HP turbine and fan–LP turbine speed equality (Equations (14) and (15), respectively), and the definitions of WN_{tHP} (Equation (16)) and WN_{tLP} (Equation (17)).

$$\pi_c = \frac{(1+f)N_{tHP}}{\pi_b WN_{tHP}} W_c \sqrt{\frac{T_{t4}}{T_{t2f}}} \tag{10}$$

$$\pi_f = \frac{P_r\sqrt{T_{t2f}}}{P_{t2}W_c\sqrt{T_r}}\left[W_f\left(\frac{P_{t2}}{P_r}\right)\sqrt{\frac{T_r}{T_{t2}}} - \dot{m}_{byp}\right] \tag{11}$$

$$\pi_{tHP} = \left[1 - \frac{c_p(T_{t3} - T_{t2f})}{\eta_{mec}c'_p\eta_{tHP}(1+f)T_{t4}}\right]^{\frac{-\gamma'}{\gamma'-1}} \tag{12}$$

$$\pi_{tLP} = \left[1 - \frac{c_p\left(1 + \dfrac{\dot{m}_{byp}}{\dot{m}_{core}}\right)(T_{t2f} - T_{t2})}{\eta_{mec}c'_p\eta_{tLP}(1+f)T_{t5t}}\right]^{\frac{-\gamma'}{\gamma'-1}} \tag{13}$$

$$N_c = N_{tHP}\sqrt{\frac{T_{t4}}{T_{t2f}}} \tag{14}$$

$$N_f = N_{tLP}\sqrt{\frac{T_{t5t}}{T_{t2}}} \tag{15}$$

$$WN_{tHP} = \frac{\dot{m}_{core}(1+f)N_c\sqrt{\frac{T_{t2f}}{T_r}}}{\frac{P_{t4}}{P_r}} \tag{16}$$

$$WN_{tLP} = \frac{\dot{m}_{core}(1+f)N_{tLP}\sqrt{\frac{T_{t5t}}{T_r}}}{\frac{P_{t5t}}{P_r}} \tag{17}$$

The burner was modeled as a nonlinear component and defined by the quantities π_b and η_b (Equation (18)) (where b_1 and b_2 are characteristic parameters of the burner [10]). In addition to those relations, energy balance across the burner was considered (Equation (19)).

$$\begin{cases} P_{t4} = \pi_b P_{t3} \\ \pi_b = 1 - b_1\left(\frac{\dot{m}_{core}P_{ref}}{P_{t3}}\sqrt{\frac{T_{t3}}{T_{ref}}}\right)^2\left(f\frac{T_{ref}}{T_{t3}}\right)^2 \\ \eta_b = \eta_{b_d} - \frac{b_2}{\left(\frac{\dot{m}_{core}P_{ref}}{P_{t3}}\sqrt{\frac{T_{t3}}{T_{ref}}}\right)^2\left(f\frac{T_{ref}}{T_{t3}}\right)^2} \end{cases} \tag{18}$$

$$T_{t4} = \frac{f\eta_b H_i + c_p T_{t3}}{c'_p(1+f)} \tag{19}$$

The nozzle was modeled as an isoentropic component where two regimes of operation can be distinguished depending on whether the discharge is sonic ($Ma_6 = 1$) or subsonic ($Ma_6 < 1$). Specifically, defining $r_{crit} = \left(\frac{\frac{\gamma'-1}{2}Ma_5^2+1}{1+\frac{\gamma'-1}{2}}\right)^{\frac{\gamma'}{\gamma'-1}}$ and $r = \frac{P_6}{P_{t5}}$ for the core nozzle, in the case in which $r > r_{crit}$, the outflow is subsonic and Equation (20) holds.

$$\begin{cases} r = \frac{P_6}{P_{t5}} \\ P_6 = P_0 \\ T_6 = T_5\left(\frac{P_6}{P_5}\right)^{\frac{\gamma'-1}{\gamma'}} \\ u_6 = \sqrt{\left(\frac{2\gamma'}{\gamma'-1}\right)R'T_5\left(1-\frac{P_6}{P_5}\right)^{\frac{\gamma'-1}{\gamma'}} + Ma_5^2\gamma'R'T_5} \\ Ma_6 = \frac{u_6}{\sqrt{\gamma'R'T_6}} \\ \dot{m}_{core} = \frac{\left(\frac{P_5}{R'T_5}\right)\left(\frac{P_6}{P_5}\right)^{\frac{1}{\gamma'}}\sqrt{\left(\frac{2\gamma'}{\gamma'-1}\right)R'T_5\left(1-\frac{P_6}{P_5}\right)^{\frac{\gamma'-1}{\gamma'}} + Ma_5^2\gamma'R'T_5}A_e}{(1+f)} \end{cases} \tag{20}$$

Differently, in the case in which $r < r_{crit}$, the core efflux is sonic and Equation (20) holds with the only exception that $P_6 = P_{t5} r_{crit}$. Similar equations hold for the bypass nozzle. The remaining equations define the static properties upstream of the nozzles from their total properties (Equation (21) where $i = f, c$).

$$\begin{cases} P_i = \dfrac{P_{ti}}{\left[\left(1 - \dfrac{\gamma-1}{2} Ma_i^2\right)\right]^{\left(\frac{\gamma}{\gamma-1}\right)}} \\ T_i = \dfrac{T_{ti}}{\left(1 - \dfrac{\gamma-1}{2} Ma_i^2\right)} \end{cases} \tag{21}$$

Each of the 44 equations is first brought into its homogeneous form ($f(\vec{x}) = 0$) and then normalized by dividing the homogeneous function itself by the physical quantity it represents: for this purpose, the normalization of Equation (19) is given in Equation (22).

$$f_i(\vec{x}) = T_{t4} - \frac{f\eta_b H_i + c_p T_{t3}}{c'_p(1+f)} = 0 \quad \rightarrow \quad f_{norm_i}(\vec{x}) = \frac{\left(T_{t4} - \frac{f\eta_b H_i + c_p T_{t3}}{c'_p(1+f)}\right)}{T_{t4}} = 0 \tag{22}$$

The 44 normalized equations ($f_{norm_i}(\vec{x}) = 0$) are then brought together in a nonlinear system (Equation (19)), associated with a vector of the unknowns $\vec{x}$ (which are essentially a collection of the physical quantities contained in the left-hand member of the non-normalized equations shown above).

$$\vec{F}_{norm}(\vec{x}) = \vec{0} \tag{23}$$

3.1.2 Reference Model

The engine model used as reference is the Rolls-Royce Trent 1000 and its design parameters, derived from the type certificate [11] and ICAO databank [12], served as the basis for the selected cruise quantities in Table 2a.

The knowledge of π_c, π_f, α, $\dot{m}_{tot}$, and F in cruising conditions allowed us to estimate, through an inverse preliminary performance study [13], the value of A_e and A_{byp}, which were 0.41 m^2 and 3.20 m^2, respectively; this was essentially performed by gradually varying the value of A_e until the value of thrust under cruise conditions (F_{cruise}) shown in Table 2a was obtained. Consequently, A_{byp} was also derived. In the absence of data provided by the manufacturer, component efficiencies in Table 2b and $f = \frac{1}{42}$ were assumed. In the following sections, the parameters b_1 and b_2 are assumed equal to 0, and η_{bd} is set equal to 0.96 in order to facilitate the comparison of the outputs with those of GSP 12; finally, $H_i = 43.26 \frac{KJ}{Kg}$.

Table 2: (**a**) Trent 1000 performance in cruise. (**b**) Component efficiencies in cruise.

(**a**)	
Characteristic	**Value**
π_c	32.85
π_f	1.54
π_{int}	0.98
π_b	1.00
α	9.12
$\dot{m}_{tot}$	467.00 $\frac{\text{Kg}}{\text{s}}$
F_{cruise}	63.82 KN
N'_{tLP}	2683 rpm
N'_{tIP}	11,164 rpm
N'_{tHP}	11,164 rpm
(**b**)	
η	**Value**
η_f	0.91
η_c	0.90
η_{tHP}	0.93
η_{tLP}	0.93
η_b	0.96

3.1.3 Genetic Algorithm and LSQ Solver

The need for the use of the genetic algorithm (GA) arises from the possibility that, for a given flight condition, the initial guess solution, provided by the preliminary performance analysis (Section 3.1.7), may be relatively far from the actual nonlinear system solution. A GA is a heuristic approach based on the theory of natural evolution, which has been the subject, for decades, of numerous studies concerning its use in the resolution of nonlinear systems of different complexity and size [14]. The application of the GA in the resolution of such systems passes through the definition of a fitness function (fun_{obj}) that allows the transformation of the problem itself into one of optimization. Many forms of fun_{obj} have been proposed. They range from the sum of the absolute values of the single functions [15] up to quadratic expressions [16]; however, there is no clear superiority of one over the other. In this method, the fitness function was chosen equal to $fun_{obj}(\vec{x}) = \sum_{i=1}^{n} f_{norm_i}(\vec{x})^2$, where $n = 44$ is the dimension of the solution vector $\vec{x}$ and f_{norm_i} is defined in Section 3.1.1. The genetic algorithm process starts by defining a fitness function and a genetic representation of the solution domain: usually, solutions are represented as an array of bits (0 and 1) in order to allow typical genetic operation, such as crossover and mutation, to be conducted more easily. Then, an initial population of solution (consisting of hundreds or thousands of candidate solutions) is generated, usually randomly, within given lower ($\vec{l_b}$) and upper boundaries ($\vec{u_b}$). Individual solutions are then selected through a fitness-based process, which essentially consists of choosing the solutions that best minimize fun_{obj}. The next step is to generate a pool of solutions (children) from those previously selected (parents): for this

purpose, the crossover technique is used, which consists of breeding two parent solutions in order to produce one child solution. This operation is repeated several times in order to generate a desired number of child solutions. In order to make the genetic patrimony more heterogeneous, a portion of the population is subjected to the mutation operation, which consists of changing part of the genetic patrimony of the single solution (i.e., replacing 1 with 0 and vice versa). This operation reduces the risk of premature convergence, a situation in which the solution of fun_{obj} becomes stuck in a local minimum. Similarly, a fitness function was also defined for the LSQ solver (the same one chosen for the GA algorithm). Both the LSQ and GA solvers aim to find $\vec{x}$ that minimizes $fun_{obj}(\vec{x})$, which coincides with the solution of the system of nonlinear equations. The combined use of the two techniques allows us to mitigate the disadvantages associated with the single algorithms; in fact, unlike the methods based on the local gradient of a function (LSQ), the GA has the advantage of reducing the probability of incurring a local minimum, which is very common in the case of functions with multiple local minima, at the expense of a higher computational cost.

3.1.4 Feedforward Neural Networks

In the turbofan under consideration, rotating component maps were considered, whose behaviors were generalized through ANN. In this regard, a careful review of the literature suggested, for the compressor ANN modeling, the use of feedforward neural networks consisting of a small number of layers [17] and an empirically determined number of neurons such that the MSE is minimized: in particular, a study conducted on a dataset of 54 experimental points led to an average error on the π and W_c of a compressor of about 1% [18]. In the following implementation of this method, a feedforward architecture with 5 hidden layers is adopted, in which the connections between the various nodes do not form loops, or information flows unidirectionally from input x_i to output y_i. First, the input x_i is normalized, i.e., its mean is subtracted and is, in turn, divided by the standard deviation. Then, the normalized input (x_{norm_i}) reaches a specific neuron within the first hidden layer, which multiplies it by its weight (w_{ij}) and adds it to its bias (b_{ij}); this result is filtered by an activation function, chosen here as the hyperbolic tangent sigmoid function (tansig) (Equation (24)). This process is repeated for all the inner layers until the output layer is reached. The last layer output is a normalized value (y_{norm_i}) which needs to be denormalized in order to obtain the ANN output value (y_i).

$$\begin{cases} l_1 = tansig(w_1 x_{norm_i} + b_1) \\ l_i = tansig(w_i l_{i-1} + b_i) \\ y_{norm_i} = tansig(w_6 l_5 + b_6) \\ x_{norm_i} = \dfrac{x_i - x_{mean}}{\delta_{std_x}} \\ y_i = y_{norm_i} \delta_{std_y} + y_{mean} \end{cases} \tag{24}$$

Training was performed using Levenberg–Marquardt algorithm. Networks of all the rotating components were built in Matlab with the feedforwardnet command using 5 hidden layers of different size of neurons, each listed in Table 3: the choice of this parameter stems from the need to achieve good network performance without data overfitting phenomena. All networks have 2 inputs (N e π for compressor and fan, WN e π for turbines) and 2 outputs (W e η for compressor and fan, N e η for turbines).

Table 3: Neuron count per layer.

Component Map	Neurons
Fan	6
Compressor	6
HP/LP turbine	8

3.1.5 GA and LSQ Matlab Implementation

A GA algorithm was implemented in Matlab [19] and called by the "ga" function which required the definition of several parameters such as population size, maximum generation, and crossover fraction, as shown in Table 4: in this regard, as specified in [20], we decided to maintain a high crossrate value (0.9) in order to be able to reduce the population size.

Table 4: GA options.

Feature	Value
Population size	300
Max generation	30
Crossover frac.	0.9

In the same way, the LSQ solver was invoked in Matlab by the "lsqnonlin" command [21] and required the definition of additional parameters such as the starting point ($\vec{x}_0$), $\vec{u}_b$, and $\vec{l}_b$ and the max number of iterations (set to 500).

3.1.6 Modeling Rotating Components with ANN

The database containing the rotational component maps was imported from GSP 12. Data for the individual component were then subjected to piecewise linear interpolation, via the Matlab function "interp1", which allowed the size of the individual database to be increased, maintaining a faithful representation. This last operation was necessary because neural networks require a large amount of data for their proper training. Next, data normalization was performed after estimating the mean value and standard deviation of the dataset obtained by interpolation: normalized data were then used to train a feedforward neural network. The specific configuration of the neural network was defined using the "feedforwardnet" function, while the training was carried out using the "train" function and the network parameters in Table 3. During the network testing phase, mean squared error values for each network were estimated and are reported in Table 5a; in addition to these, in order to better characterize the error on the outputs, the mean percentage errors ($\bar{x}\%$), the maximum percentage errors ($err_{max}\%$), and their standard deviations ($\sigma\%$) were calculated (Table 5b).

Table 5: (**a**) Mean squared errors for turbofan rotating components (values refer to the test dataset). (**b**) Mean percentage errors $\bar{x}\%$, max percentage errors $err_{max}\%$, and standard deviations $\sigma\%$ for the compressor, fan, and turbine output variables (values refer to the test dataset).

(**a**)

MSE	**Value**
Fan	$2.03 \cdot 10^{-4}$
Compressor	$5.14 \cdot 10^{-4}$
Turbine	$2.87 \cdot 10^{-6}$

(**b**)

error measures	W_c	η_c	W_f	η_f	N_{tHP}	η_{tHP}
$\bar{x}\%$	0.82	0.08	0.59	0.05	0.04	0.03
$\sigma\%$	1.63	0.11	1.71	0.06	0.04	0.04
$err_{max}\%$	16.47	1.13	19.63	0.58	1.19	2.56

A careful analysis reveals that the highest percentage error points tend to be located, for both the fan and the compressor, along the stall regions and more at a low to medium N (Figure 2).

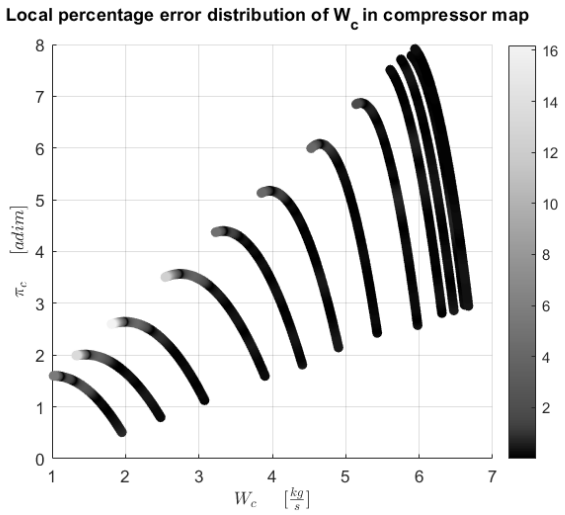

Figure 2: Compressor local error map for different N constant curves.

3.1.7 Hybrid LSQ—GA Solver

Using the elements described in the previous Sections, an algorithm for calculating the performance of a turbofan was formulated: such performances are presented in the form of operating lines on component maps and overall performance as function of f (see Section 3.2.1). This algorithm is based on the interaction of 3 functional blocks (Figure 3), which perform the specific tasks listed below:

- Preliminary design calculation (Figure 4);

- Nonlinear solution calculation (Figure 5);
- Nozzles condition check (Figure 6).

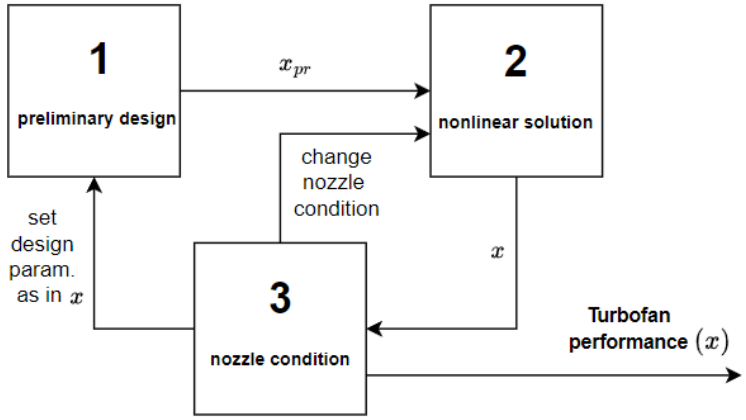

Figure 3: Interactions between the three parts of the algorithm.

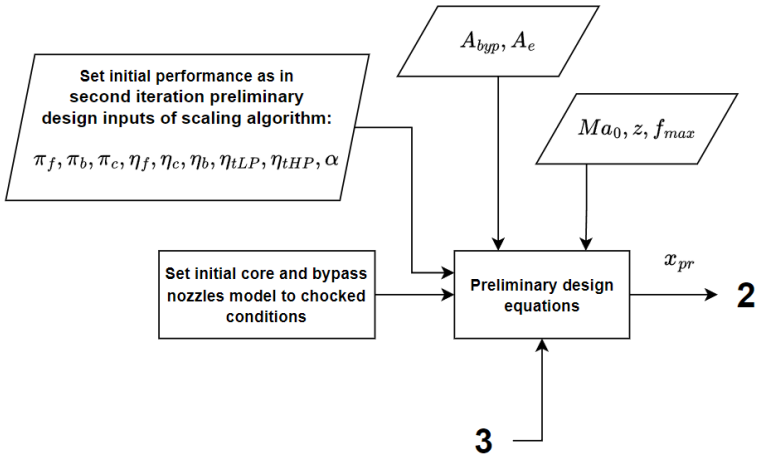

Figure 4: Preliminary design calculation in Figure 3.

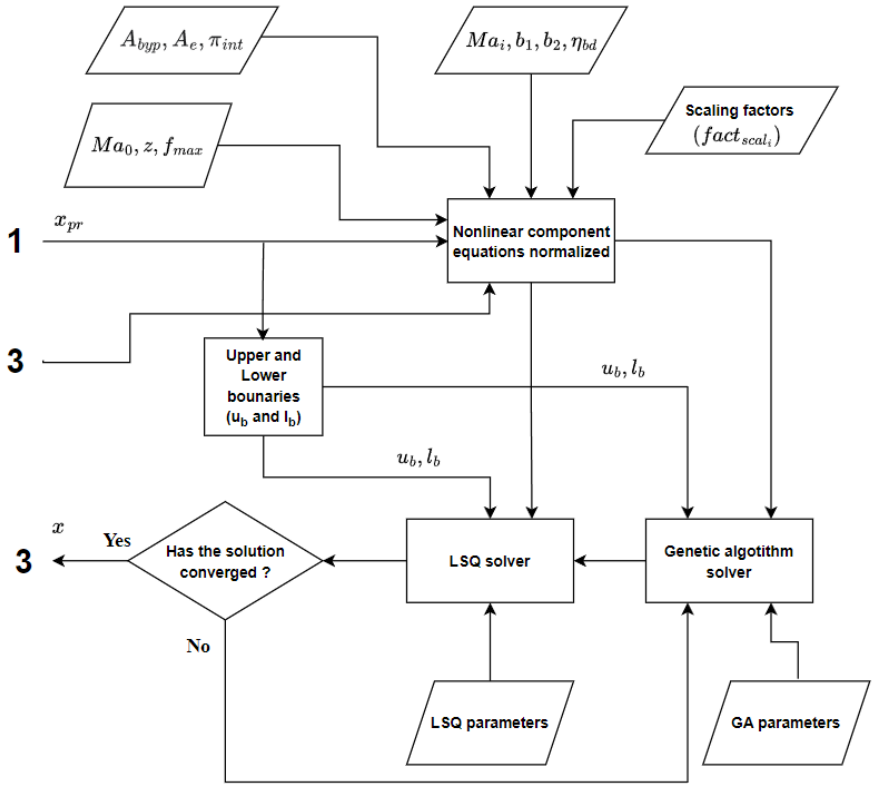

Figure 5: Nonlinear solution calculation in Figure 3.

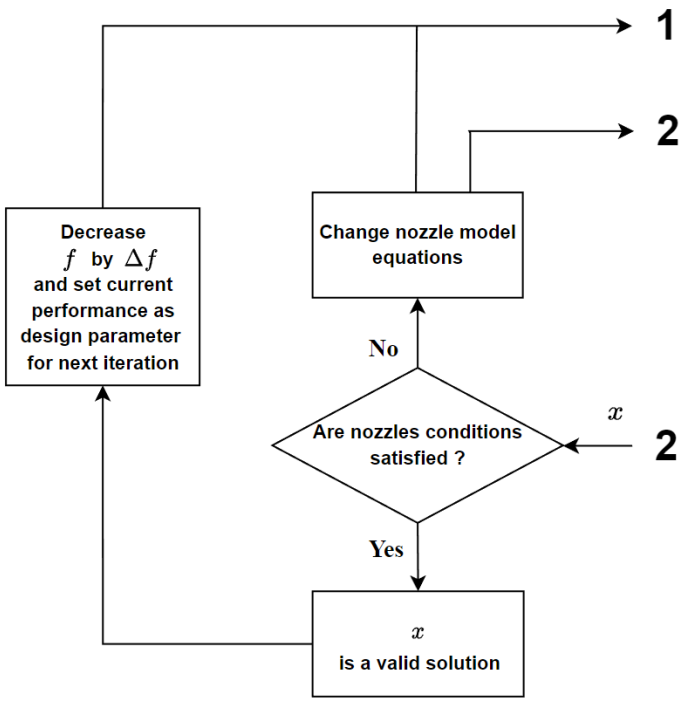

Figure 6: Nozzles condition check in Figure 3.

Preliminary design calculation was realized according to [13, 9]. Preliminary design calculation (Figure 4) begins by setting both core and bypass nozzle state to chocked on the

first iteration, then the preliminary solution is computed starting from the second iteration preliminary design inputs (π_{int} ,π_f, π_b, π_c, η_f, η_c, η_b, $\eta_{t_{LP}}$, $\eta_{t_{HP}}$, α) of scaling algorithm (see Section 3.1.8 for more details), with the desired value of Ma_0, z, and an initial value of $f = f_{max}$; other input data are A_e and A_{byp}. Specifically, the f_{max} is chosen close to the f_{cruise} but greater than it, and, defining $\varepsilon = f_{max} - f_{cruise}$, we have that ε increases as the altitude decreases (see Table 6 as an example). Preliminary design calculation output ($\vec{x}_{pr}$) is a 44-element vector which is essentially a rough estimation of vector $\vec{x}$ (turbofan performance): $\vec{x}_{pr}$ constitutes the input for the nonlinear solution calculation.

The nonlinear solution of Figure 5 starts by first calculating the lower ($\vec{l}_b$) and the upper ($\vec{u}_b$) boundary necessary to run the GA solver: this is simply conducted by setting $\vec{l}_b = 0.1 \cdot \vec{x}_{pr}$ and $\vec{u}_b = 10 \cdot \vec{x}_{pr}$. The nonlinear solution block calls the turbofan normalized equations system, described in Section 3.1.1, and requires as input, in addition to the selected flight condition (f,Ma_0 and z), $\vec{x}_{pr}$, Ma_i (Mach value of the flow for each engine section given in Table 7), A_{byp}, A_e, π_{int}, b_1, b_2, η_{bd}, and the scaling factors ($fact_{scal_i}$). In actuality, the value of Mach in the engine sections varies in off-design conditions; nevertheless, the variation is very small and has a negligible impact on performance. Scaling factors are determined using procedures explained in Section 3.1.8.

Table 6: Trent 1000 flight conditions for operating lines.

Flight Phase	z **[m]**	Ma_0	f_{max}	f_{min}	Δf
cruise	11,000	0.85	0.0263	0.0168	$1.6354 \cdot 10^{-4}$
climb 1	7000	0.6	0.0263	0.0168	$1.6354 \cdot 10^{-4}$
climb 2	5000	0.45	0.0270	0.0168	$1.7560 \cdot 10^{-4}$
take off	0	0.20	0.0312	0.0181	$2.4718 \cdot 10^{-4}$
static	0	0	0.0312	0.0181	$2.4718 \cdot 10^{-4}$

Table 7: Mach hypothesis at the component inlet section.

Fan	**Compressor**	**Burner**	**LP Turbine**	**HP Turbine**	**Byp Nozzle**	**Core Inlet**
0.40	0.40	0.40	0.30	0.40	0.40	0.40

The nonlinear equation system is solved through a combined approach that involves the use of the GA solver first and then the LSQ solver: now, if the LSQ solver fails to compute the solution ($\vec{x}$) with an error, measured by the squared norm of the residual (with i-th residual defined as $fun_i(\vec{x})$), higher than 10^{-20}, this solution is discarded and the GA solver recalculates again starting from $\vec{x}_{pr}$, generating a new population of solutions.

The nonlinear solution is then passed to the nozzle condition check block (Figure 6) in order to check whether the assumptions previously made on the nozzles were corrected. If positive (or $P_6 > P_0$ and $P_7 > P_0$), the algorithm decreases the value of f by a fixed Δf, sets the value of the design parameters (π_f, π_b, π_c, η_f, η_c, η_b, $\eta_{t_{LP}}$, $\eta_{t_{HP}}$, α) equal to their value found in the vector $\vec{x}$, and sends them to the preliminary design block. Thus, a new iteration can start from preliminary design calculation (Figure 4). If negative, the nozzle conditions are changed, imposing different core/bypass nozzle conditions (see Equation (20)), and the entire process is repeated with the same f, in particular:

- If $P_6 > P_0$ and $P_7 \leq P_0$, chocked core/unchocked bypass nozzle condition are set;
- If $P_6 \leq P_0$ and $P_7 > P_0$, unchocked core/chocked bypass nozzle condition are set;
- If $P_6 \leq P_0$ and $P_7 \leq P_0$, unchocked core/unchocked bypass nozzle condition are set.

Because of what was stated above, following each iteration from the successful outcome, the value of f is decremented by Δf. In the case where the objective is the determination of the operating line, the algorithm continues until a value of f corresponding to low engine speeds is reached ($f = f_{min}$), while in the case where performance for a specific flight condition (Ma_0, z, f) is of interest, it will be necessary to choose very small values of Δf such that, after a certain number of iterations, the desired value of f is intercepted. The procedure shown in this section is used in Section 3.2.1 to generate the operating lines on the rotating component maps as well as the performance values at certain flight conditions. Table 8 summarizes the fixed parameters and variables illustrated in the above algorithm.

Table 8: Summary of fixed and variable parameters.

Type	Parameter/Variable List
Fixed parameter	$A_{byp}, A_e, Ma_0, z, f_{max}, f_{min}, \Delta f, \pi_{int}, Ma_i, b_1, b_2, \eta_{bd}, fact_{scal_i}$
Variable	All other quantities

3.1.8 Map Scaling

The database for constructing the maps used in this thesis was exported from GSP 12 software. However, the use of these maps was subject to a scaling operation since generic maps of compressors and turbines are used in the present thesis, which must be appropriately scaled to ensure a given design operating point position on maps. Map scaling consists of determining the scaling factors ($fact_{scal}$ (see Equation (2)) for Equation (5)) to be applied to each of the 4 variables of the fan/compressor (N, W, π, and η) or turbines (N, WN, π, and η). A comprehensive description of the standard scaling procedure of rotary component maps performed by GasTurb 13 software can be found in [22]; the same modalities apply to GSP 12. The scaling operation proposed in this software consists of multiplying each map by a correction factor, calculated as the ratio between the value calculated in the preliminary design phase (var_{pr}) and that provided by a reference point on the map (var_{map}) (Equation (25) where var are map variables).

$$fact_{scal} = \frac{var_{pr}}{var_{map}} \tag{25}$$

However, a slightly different scaling method is used in this work. Such use is made necessary by the need to partially compensate for numerical inaccuracies caused by moderate conditioning of the nonlinear system. The present scaling algorithm basically consists of the algorithm proposed in Section 3.1.7 plus some modifications, which are detailed below: we will explain the scaling operation of π_f, and similar steps are performed simultaneously for all the remaining design parameters. The scaling algorithm is iterated 2 times. The first iteration ($i = 1$) begins by setting inputs as in Equation (26), where $\pi_{f\,guess}$ is first assumed as in Table 2a,b, and k_i is initially set to 1.

$$\pi_{f\,pr_{(i)}} = \frac{\pi_{f\,guess}}{k_{(i)}} \tag{26}$$

The preliminary design solution ($\pi_{f\,pr_{(i)}}$) is then computed and $fact_{scal_{(i)}}$ is derived from Equation (27) as a function of $k_{(i)}$, $\pi_{f\,pr_{(i)}}$ and the position on the original map ($\pi_{f\,map}$).

$$fact_{scal_{(i)}} = \frac{\pi_{f\,pr_{(i)}}}{\pi_{f\,map}} \cdot k_{(i)} \tag{27}$$

Using $\pi_{f\,pr_{(i)}}$ and $fact_{scal_{(i)}}$, the nonlinear solution ($\pi_{f_{(i)}}$) is then calculated, which is used to determine the parameter $k_{(i+1)}$ (Equation (28)) and a new iteration begins.

$$k_{(i+1)} = k_{(i)} \cdot \frac{\pi_{f_{(i)}}}{\frac{\pi_{f\,guess}}{k_{(i)}}} \tag{28}$$

This process ends at $i = 2$ and the same scaling procedure is performed simultaneously for all other design parameters. The scaling process is considered to be successful only if the results of the second iteration ($i = 2$) of the scaling process provide performance very close to that shown in Table 2a,b; if not, it would be necessary to slightly vary the guess design parameters ($\pi_{f\,guess}$, etc.) by increasing or decreasing that value depending on whether one obtained, in the second iteration ($i = 2$), a value smaller or larger than the value shown in Table 2a,b. This variation procedure is performed manually, but the authors reserve the possibility to create, in a future article, a routine that automates this process as well. The scaling factor obtained in the second iteration ($fact_{scal_2}$) is used as definitive value of the scaling factor, while the second preliminary design input (x_{pr_2}) is used to initialize the solution of the turbofan simulation in Section 3.1.7, as shown in the diagram in Figure 7. This scaling procedure makes it possible to compensate for most of the errors introduced in the computational phase of the solution of the nonlinear system, which arise from a moderate condition number of the Jacobian matrix associated with the system of equations.

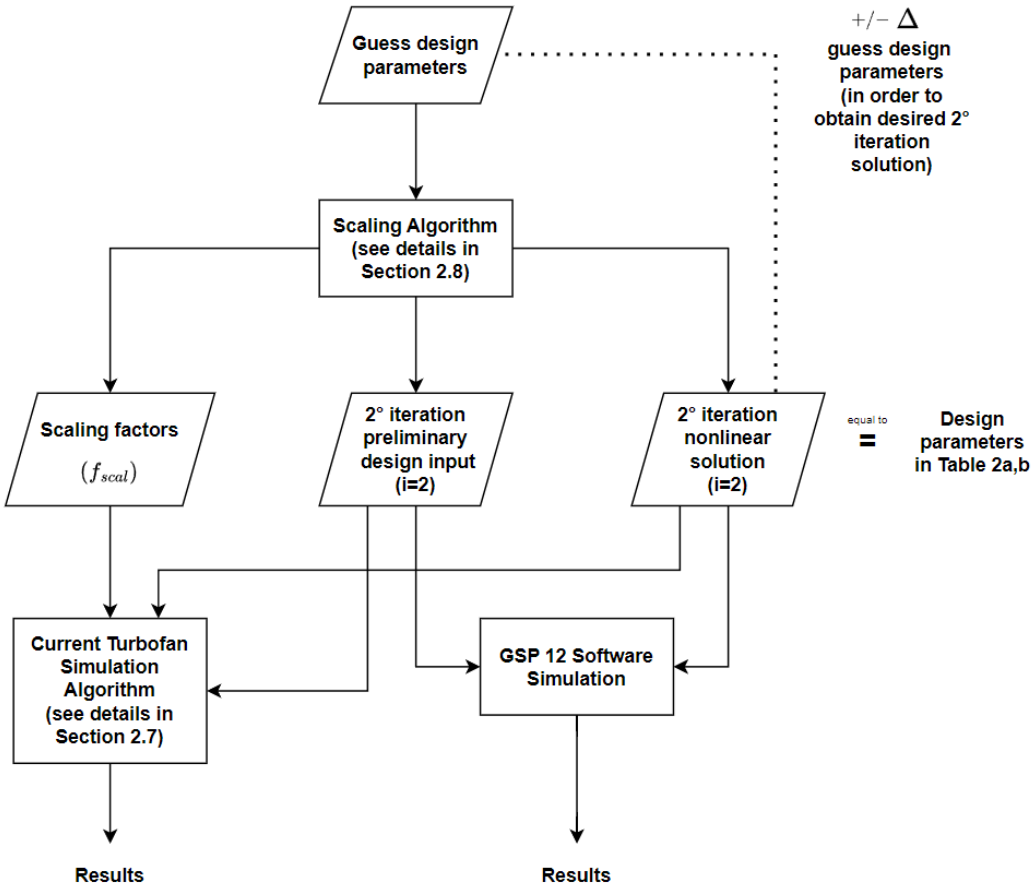

Figure 7: Overall turbofan simulation algorithm including scaling block.

3.2 Results

In this Section, results of the numerical simulations are reported in the form of operating points on the rotating component maps and overall turbofan performance (F and $\dot{m}_{fuel}$) as function of f.

3.2.1 Performance Evaluation for Relevant Flight Phases and Comparison with GSP 12

Simulations are performed for the different flight phases: they vary from cruising condition to static operation at sea level (Table 6).

These results are reported both in the form of steady-state operating points on the various maps (Figures 8–11) and in the form of graphs for the overall performance (Figures 12 and 13) as f varies. In particular, current algorithm validation is obtained through comparison with simulations carried out with GSP 12 software [4], which is provided with the same data as in Table 2a,b. Validation simulations are carried out for values of z and Ma_0 reported in Table 6 in correspondence with four distinct values of f in the interval between f_{max} and f_{min} (Table 9): the current algorithm operating points are identified in Figures 8–11 using circle markers, while GSP 12 points are identified using square markers.

Table 9: GSP points flight conditions.

Flight Phase	f_1	f_2	f_3	f_4
Cruise	0.0263	0.0232	0.0199	0.0168
Climb 1	0.0263	0.0232	0.0199	0.0168
Climb 2	0.0270	0.0237	0.0202	0.0168
Take-off	0.0312	0.0266	0.0216	0.0183
Static	0.0312	0.0266	0.0216	0.0182

More extensive simulations aimed at identifying the operating line are performed for the same conditions in Table 6 using around 48 to 54 values (depending on the flight phases) of f between f_{max} and f_{min} spaced apart from each other by Δf (Table 6). Figures 8–11 show the variation of π_f, π_c, π_{tLP}, and π_{tHP} as a function of the respective corrected mass flow rates W or WN (in the case of turbines), as f varies, starting from the right (where $f = f_{max}$) to the left ($f = f_{min}$), forming the operating line. It can be seen how the resulting operating line is in agreement, with a fair margin of error, with the trend resulting from the data provided by GSP 12.

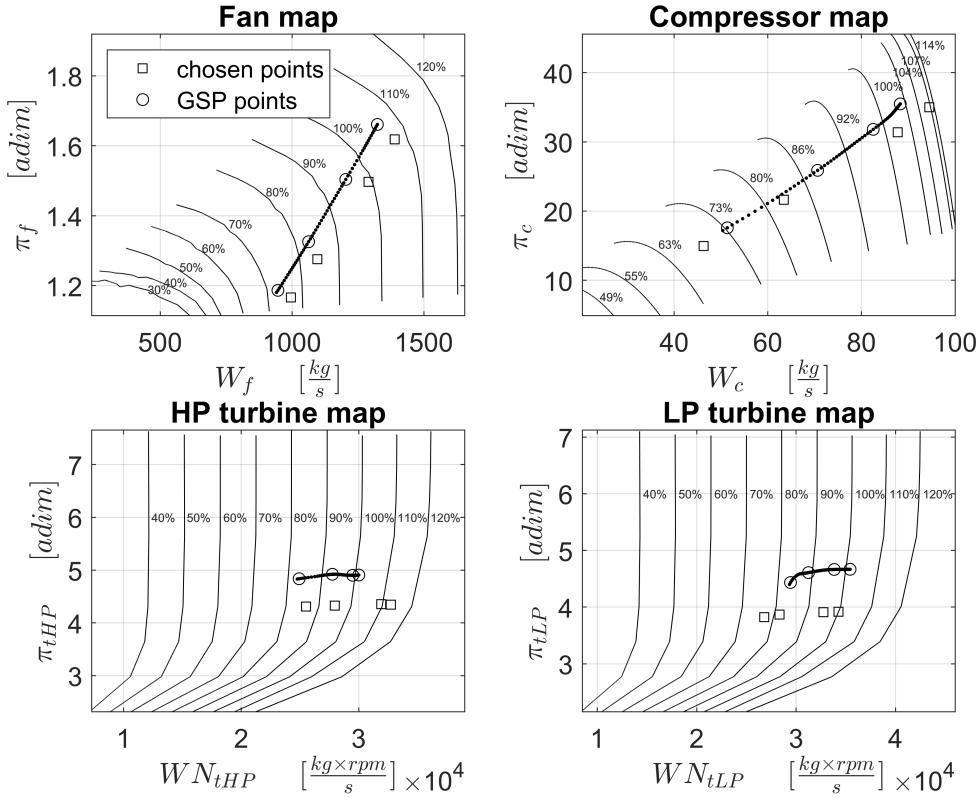

Figure 8: Operating lines on maps for $z = 11{,}000$ m and $Ma_0 = 0.85$ as f decreases from 0.0263 to 0.0168.

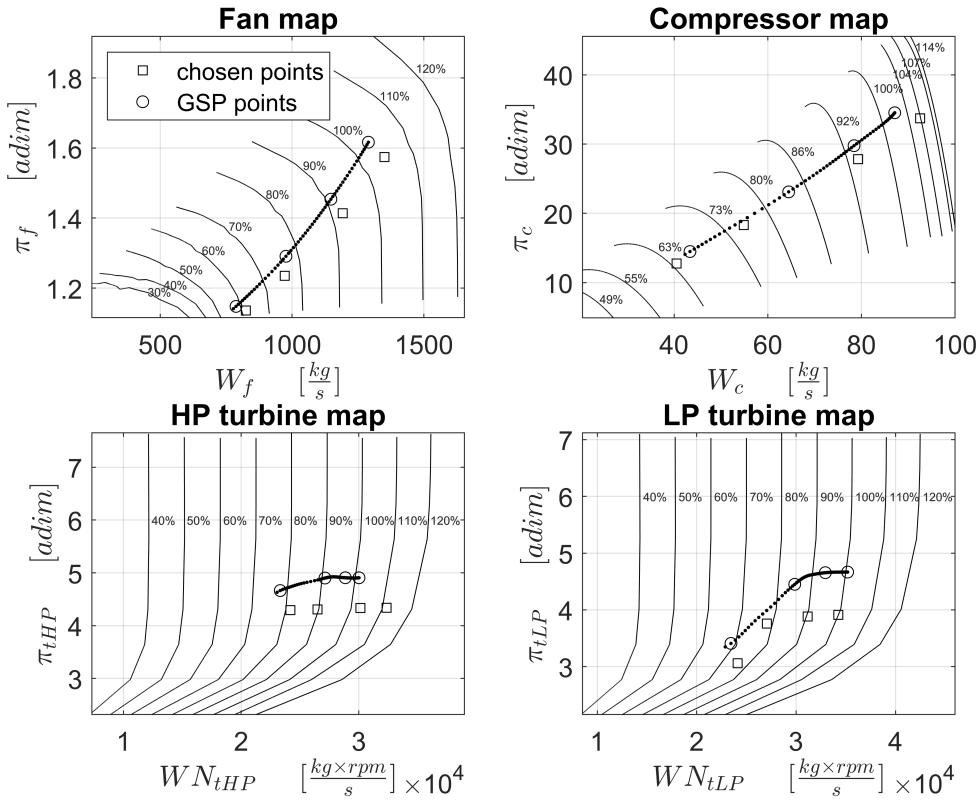

Figure 9: Operating lines on maps for $z = 5000$ m and $Ma_0 = 0.45$ as f decreases from 0.0270 to 0.0168.

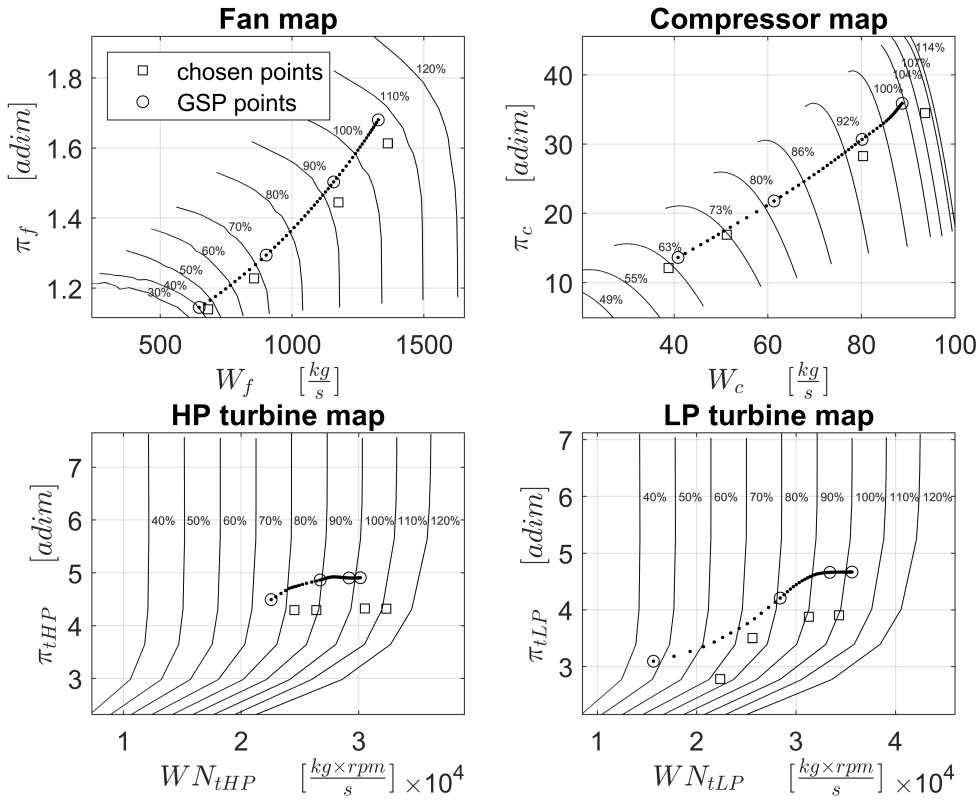

Figure 10: Operating lines on maps for $z = 0$ m and $Ma_0 = 0.20$ as f decreases from 0.0312 to 0.0183.

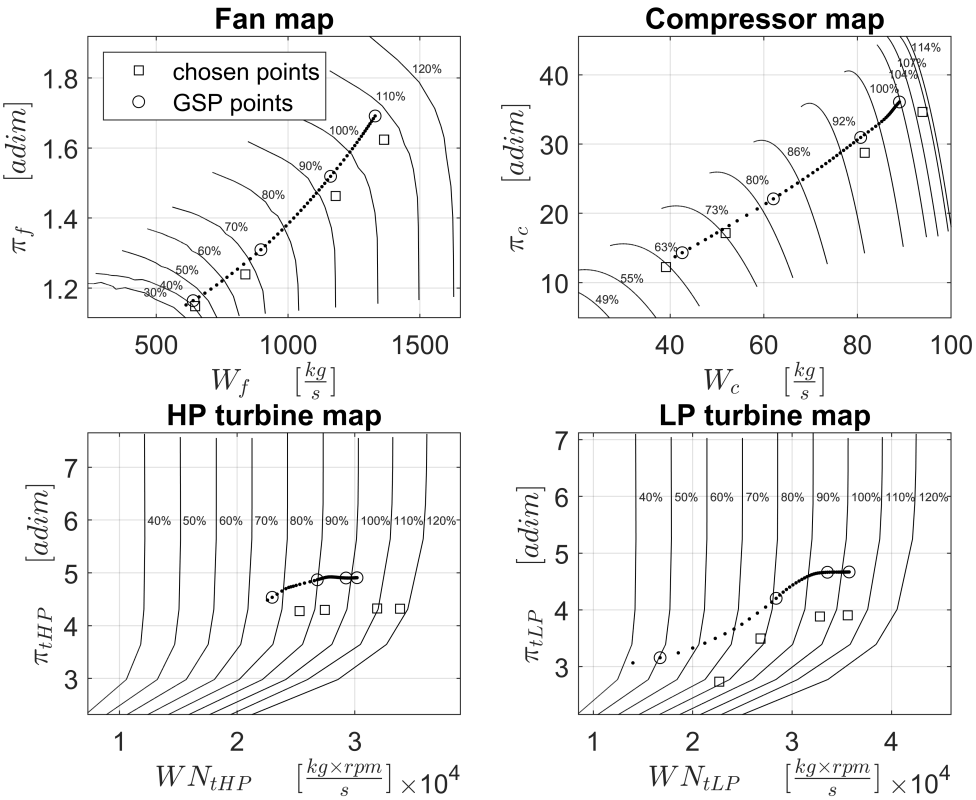

Figure 11: Operating lines on maps for $z = 0$ m and $Ma_0 = 0$ as f decreases from 0.0312 to 0.0182.

Similar considerations also apply to Figures 12 and 13 (where lines are used for simulation results while GSP 12 points are depicted by symbols), which show a nearly linear trend of $\dot{m}_{fuel}$ and F as function of f, in very good agreement with the output of GSP 12.

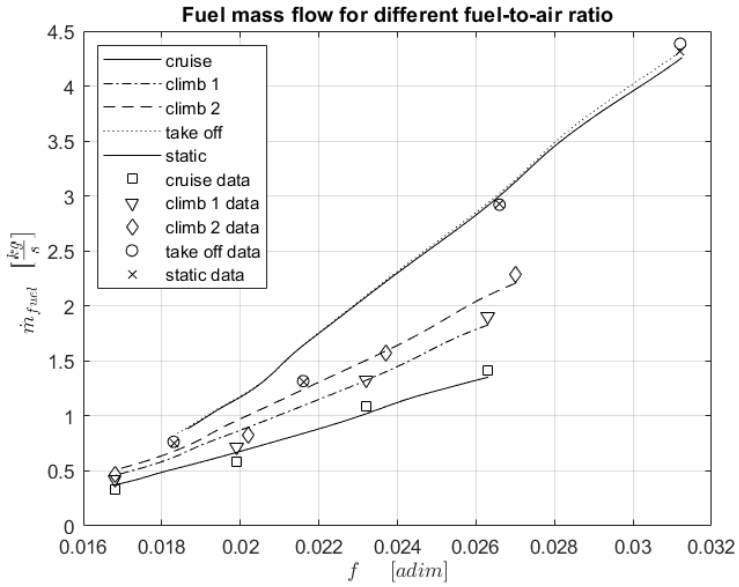

Figure 12: Trend of $\dot{m}_{fuel}$ as f decreases for flight conditions shown in Table 6.

Finally, a comparison of computational times between the present algorithm and GSP 12 was performed at three distinct flight phases and for a fixed number of points (20) between f_{max} and f_{min} (Table 10). The results show that there is limited difference in computational time; nevertheless, it is necessary to take into account that GSP 12 also computes solutions of a fair amount of intermediate points.

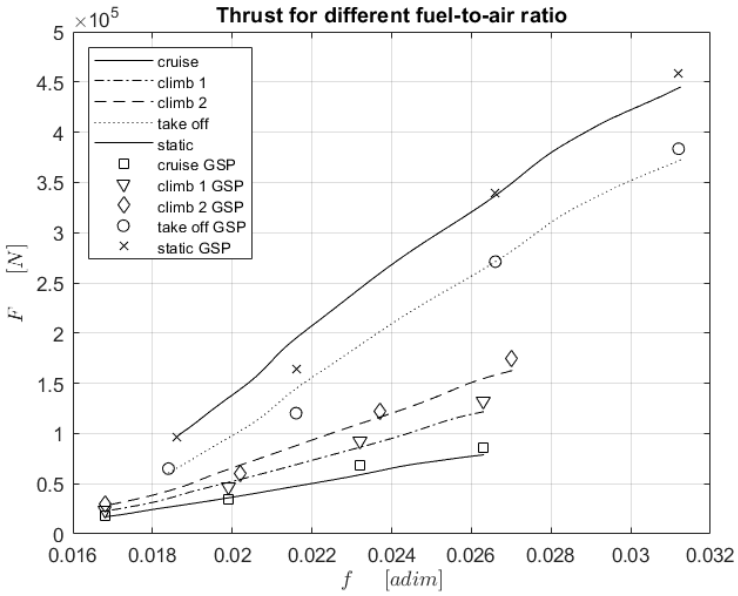

Figure 13: Trend of F as f decreases for flight conditions shown in Table 6.

Table 10: Comparison of computational time.

Flight Phase	f_{max}	f_{min}	**n°Points**	**GSP 12 Time** $[s]$	**Actual Algo Time** $[s]$
Cruise	0.0263	0.0189	20	50	56
Climb 2	0.0270	0.0189	20	56	68
Static	0.0312	0.0189	20	57	86

3.3 Conclusions

The present work demonstrates how a steady-state nonlinear turbofan model with components represented by nonlinear equations or implicit relations derived from neural network training can be effectively solved using GA and LSQ algorithms. A major advantage over current commercial codes (GSP 12, GasTurb) is the ease of implementation in Matlab and the ability to implement various components by simply modifying the system equations. This simplicity of implementation is made possible by the use of a scaling mode that can compensate for most of the errors caused by the potential ill-conditioning of a large nonlinear system. The results obtained suggest that trends in F and $\dot{m}_{fuel}$, as flight conditions change, are consistent with the outputs obtained from GSP 12 software. A small contribution to the error can also be attributed to differences, difficult to detect, in turbofan modeling between the present algorithm and that of GSP 12. The average interpolation error for all variables of the maps and their standard deviations do not exceed 1% and 1.5%, respectively. A relevant aspect of the reduction in the accuracy of the simulations could be determined by the high

local maximum percentage error, which is around 16.50% for the fan and compressor maps (but turns out to be about 1% for the turbine map); however, for the present simulations, this aspect is negligible because the operating points do not fall within these regions. More investigation into the interaction of the various errors is needed in order to solve these problems; however, it emerges unequivocally that the feasibility of such an approach is related to finding the ANN architecture and the structure of the data that minimize both the MSE and the maximum local error. This work also demonstrates the effectiveness and feasibility of using the combined GA/LSQ approach for solving nonlinear systems of even considerable dimensionality. Future studies will focus on improving the accuracy and method reliability, extending it to nonstationary off-design performance.

4 Variable pitch fans

The fan strongly influences the performance of modern turbofan engines. This is greatly amplified by the transition to higher bypass ratios (BPRs) that leads to the use of larger fans.

The increase in BPR allows the reduction of thrust specific fuel consumption (TSFC) and thus, for the same thrust generated, improves fuel economy. Given the important environmental targets set by organizations and government authorities around the world, reduction in fuel consumption is a major step towards the neutral carbon footprint target. At the same time, it represents a major opportunity for engine manufacturers (such as Rolls-Royce or General-Electric) to provide airlines with a reduction in variable costs and thus a potentially increase in profit margins. However, the increase in fan diameter would lead, for very high by-pass ratio (UHBR) solutions, to obvious issues with ground clearance and drag increase (given the large increase in frontal area). Therefore, over the past 20 years, complementary solutions that can increase turbofan performance, including Variable Pitch Fan (VPF), have been proposed by the industry and the academic community.

The VPF is an advanced aerodynamic feature that enables the adjustment of the fan blade angle (pitch) during operation. The VPF offers adaptability to varying operating conditions, providing potential benefits in efficiency, noise reduction, and versatility. The only turbofan engine model equipped with VPF to be produced was the Turbomeca Astafan series. The ability to adjust pitch allows the engine to maintain optimal performance for wide ranges of flight altitude, flight speed, and engine rpm. Therefore, the performance improvement will be more pronounced for medium- and short-duration flights, where the cruise portion becomes less dominant than other flight phases. In the take-off phase, the pitch is increased and is then gradually decreased, reaching a minimum at cruse condition. Studies have shown that, for a medium-range mission, the use of VPF can lead to the decrease of TSFC by about 8% [23] [24]. Pitch variation can also allow for faster response to engine power demand. It is also possible to use the VPF to generate negative thrusts, allowing the elimination of the two thurst reversers, thus reducing the total weight by about $1000kg$. However, the problems with VPF are several. From a manufacturing point of view, there is a significantly larger number of components than in a conventional fan. This increase in component count not only increases complexity but potentially reduces the reliability of the system. Some examples of kinematics for fan pitch variations can be found in literature [25] [26].

While from a structural point of view the main problem lies in the possibility of high concentrations of mechanical stress in some sensitive components, from an aerodynamic point of view the biggest problem is definitely tip shroud sealing. The space between tip blade and shroud decisively affects fan performance [27] [28] [29]. Specifically, fan performance degrades rapidly as tip clearance increases, which is why it is usually contained within 1% of the blade length. The presence of tip clearance allows to provide enough space for blade deformation in the radial direction caused by centrifugal forces and eventually to compensate for any small tolerance defects. The use of a VPF makes tip sealing even more complex because the variation in blade pitch around its rotation axis causes the clearance to increase or decrease unevenly (Figure 14a and Figure 14b).

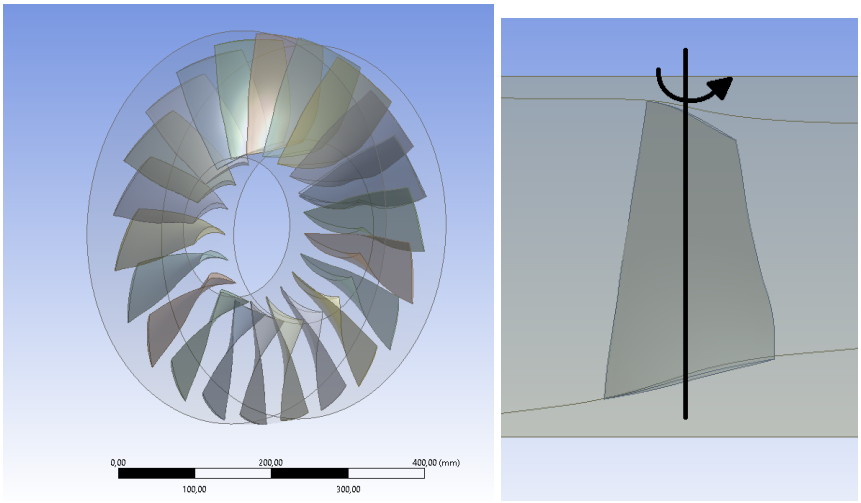

(a) (b)

Figure 14: Fan Blade row and VPF rotation axis

4.1 Simulation methods

Performance evaluation of VPF need to be performed in both design (or cruise) and off-design conditions. Since the performance study would require performing simulations for a fairly large number of flight conditions, it is therefore necessary to use a computationally sustainable approach. This condition excludes a priori the use of more accurate CFD simulation methods with Large-Eddy-Simulation (LES) or Direct-Numerical-Simulation (DNS). CFD simulation using Reynolds-Average-Navier-Stokes equations can provide fair detailed indication for the creation and testing of VPF prototypes at an acceptable computational cost. Simulation of VPFs can be accomplished using the entire fan or using a single blade passage, exploiting the geometric symmetries of the fan. The blade passage consists of a blade geometry plus the two adjacent gaps (Figure 15).

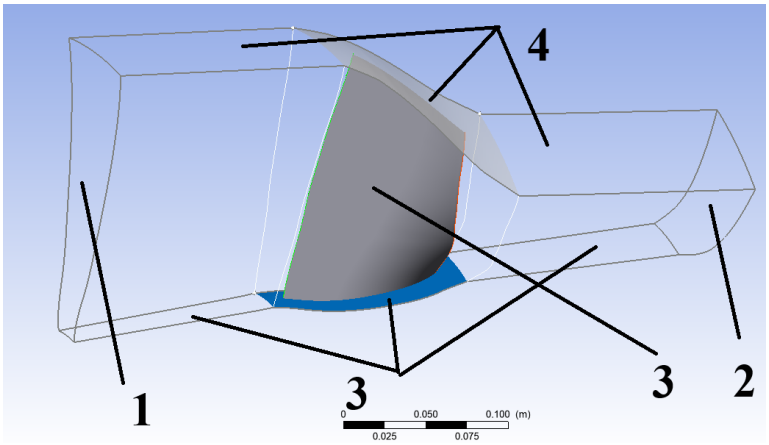

Figure 15: Blade passage with section numbered according to Table 12

The simulation performed with the blade passage allows only symmetrical flight conditions to be studied but nevertheless provides important insights for design. The main purpose

is to obtain, for a fixed fan pitch angle (θ), the component performance map, such as that shown in Figure 16.

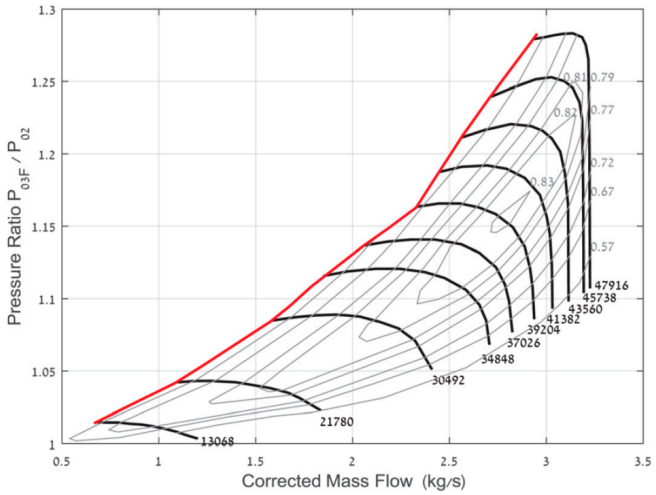

Figure 16: Fan map [30]

Such maps are the graphic representation of relations between the variables η, π, N and W. The basic idea is to obtain maps for a set of values of θ between $-5°$ and $+5°$ (for example $\alpha = [-5,-3,-1,0,+1,+3,+5]$) and then interpolate between these to obtain maps for intermediate values of θ.

To make a more careful noise estimations, however, it is necessary to consider the rotor + stator assembly since a substantial portion of the noise is caused by the interaction between the turbulent wake of the rotor and the leading edge of the stator [31].

Starting from the blade passage geometry in CAD format, the simulation can be performed using Ansys Turbogrid and Ansys CFX softwares. Turbogrid is used to generate surface and volume meshes, while in CFX the CFD settings are selected and the boundary conditions are imposed.

4.2 Rotor 67 geometry

Currently only a few open source rotor geometries are available in the scientific literature: NASA Rotor 67 and CATANA fan [32] [33]. Both geometries refer to scaled rotors with a total diameter of about $50cm$. The Rotor 67 is an old generation fan, conceived more than 35 years ago while the CATANA fan incorporates all the features of a new generation UHBP fan.

In this work we use the Rotor 67 because the CAD geometry is already available [34]. An additional motivation for choosing the NASA Rotor 67 is the availability of a discrete amount of experimental data. Xinyu Bian also performed Rotor 67 simulation using a single blade passage and showed excellent overlap of numerical results with available experimental data [35]. Also in [36] the author illustrated a new approach for simulating the rotor + stator assembly using Rotor 67 + Stator 67. The values of rotor speed (N), corrected flow rate (W_c) and π under nominal conditions are shown in Table 11 [37].

Table 11: Rotor 67 nominal condition

N $[rpm]$	W_c $[\frac{Kg}{s}]$	π $[adim]$
16042	33.25	1.63

These values were obtained for inlet pressure and inlet temperature of $1atm$ and $288K$, respectively. The blade dimensions are available in [37].

4.3 VPF geometry

In a VPF, rotation about its own axis results in a change in the tip clearance distribution from uniform, at the reference position point, to nonuniform. The reference position is conventionally assumed such that $\theta = 0°$. In order to ensure a minimum tip clearance of 1% for any pitch value, it is therefore necessary to increase the baseline clearance, that is, the clearance under zero pitch conditions, by a certain percentage. In the present work we have verified that increasing the baseline clearance from 1% to 2% is sufficient to satisfy the requirements for a pitch range of $-5°$ to $+5°$.

4.4 Mesh and Boundary conditions

The volume was divided into approximately 285309 hexagonal elements with a total of 306630 nodes. The type of boundary conditions imposed on the single blade passage are listed in Table 12 with reference to Figure 15.

Table 12: Boundary conditions specification

ID	1	2	3	4	5
Type	inlet	outlet	wall	rotating-wall	periodic boundary

In the inlet section, static temperature and total fluid pressure are imposed, while in the outlet section, static temperature and static pressure are imposed. The choice not to impose an inlet or outlet mass flow rate is due to the rise in frequent solution instabilities. The surfaces of the blade and case are defined as walls while a counter-rotating wall is chosen for the shroud (since it rotates in the opposite direction with respect to all the other rotor elements). The remaining (side) surfaces are defined as periodic boundary conditions.

4.5 Conclusions

The technique illustrated in Section 4 allows to simulate the performance of a VPF under symmetrical fly conditions. In Section 4, the discussion was limited to describing the method, and testing it in some operating points near nominal conditions (Table 11) for different pitch angles. All simulations performed in Ansys CFX were found to be convergent and required a variable number of iterations (in the order of $3000 - 4000$). However, the results were not included within the thesis, as the complete determination of the maps would have required time frames not compatible with those actually available.

5 Turbofan emission model

The aviation industry is increasingly focusing on human health and ecosystem impact. This is reinforced by the regulations of national and supra-national bodies [2], such as EASA (in the EU) and FAA (in the US), which incentivize the transition to aviation technologies with lower environmental impact. The challenge is further complicated by the stringent weight requirements of aircraft, which, unlike the automotive sector, currently do not allow for a transition to hybrid or fully electric propulsion [38]. However, a viable avenue for reducing emissions could be the use of sustainable aviation fuels (SAFs), which have lower life-cycle emissions compared to conventional jet fuels (*e.g.*, JP-8). The benefits of SAFs are also evident in emissions, with full-scale engine tests showing a reduction in soot of approximately 70% in static conditions [39] and 50% in cruise conditions [40]. Blends of SAFs with JP-8 (or JET-A) up to 50% in volume are drop-in fuels with chemical and physical properties similar to JP-8 [41], allowing them to be used without modifications to the turbofan design. SAFs are distinguished by their various feedstocks and production processes, with their standard for use in aircraft turbines set by the ASTM D7566 regulation. Currently, SAFs approved by ASTM D7566 include Fischer–Tropsch (FT) fuels produced from solid biomass using the Fischer-Tropsch process [42], alcohol-to-jet (ATJ) fuels produced via waste fermentation, and hydroprocessed esters and fatty acids (HEFA) fuels, albeit only in mixtures with petroleum jet fuel and within stringent blending limits.

HEFA fuels are produced via the hydroprocessing of oils and fats in a three-step process: deoxygenation, hydroisomerization, and hydrocracking [43]. Deoxygenation starts from triglycerides, such as those found in camelina crude oil [44]. After separation, fatty-acids are converted into a mixture of n-paraffins. Hydroisomerization and hydrocracking can occur in separate or simultaneous steps, transforming the n-paraffin mixture into an iso-paraffins mixture. During the hydrocracking step, the iso-paraffins are partially broken down into smaller alkanes. Given the low aromatic hydrocarbon content, the use of SAFs is permitted in blends with JP-8 up to 50% by volume.

In this context, it is crucial to have emission models that can describe the steady-state operation of turbines based on their operating parameters, such as altitude, flight Mach number, and throttle. In this work, we propose an emission model capable of predicting the behavior of different types of JP-8 and SAF fuels. This is achieved using the FGMech (**f**unctional **g**roup **m**echanism) approach [45] [46], which enables the generation of a compact lumped gas-phase kinetic mechanism for the oxidation of real fuels. The complete fuel combustion kinetic mechanism was obtained by combining the FGMech with a base mechanism describing the chemistry of small gas-phase species, such as AramcoMech 2.0 [47], AramcoMech 3.0 [48], and USC Mech II [49]). Nitrogen [50] and sulfur [51] chemistries were further merged into the gas-phase mechanism to predict NO_x and SO_x emissions.

Due to the large number of reactions and species involved in modeling the combustion of aviation fuels, using three-dimensional (3D) computational fluid dynamics (CFD) simulations is unfeasible. Therefore, over the years, multiple efforts have been made to propose alternative methods for simulating combustion and emissions in turbines, all of which suggest using 0D/1D reactor networks. Moniruzzaman and Yu [52] simulated the operation of a CFM56-2-C1 turbofan in idle. Their model, which consists solely of 0D gas parcels, provides accurate predictions for a considerable number of species. However, validation at only one operating point may limit its robustness. Bisson *et al.* [53] simulated the same type of turbofan, with validation performed over a wide range of throttle levels. Their model

uses a network of perfectly stirred reactors (PSR) and plug flow reactors (PFR) and provides satisfactory results for the concentrations of the main gaseous pollutant species and soot generated from JP-8. However, it is important to note that the validation was conducted only under static conditions.

In the present work, an equivalent modeling of the turbofan was proposed through a network of PSR and PFR reactors, implemented using the Chemkin API [54] [55] in a Python script. This model, unlike those in previous literature, was validated over a wider range of operating conditions, limiting discretionary tuning to only one parameter while deriving all other parameters from chemical and physical considerations. Information from single annular combustor (SAC) CFD simulations in the literature [56] was used to gain qualitative insights into the possible configuration of the reactor network. Their results, which utilized a SAC with a geometry very similar to the one under our consideration, show that the temperature is maximum in the central zone of the combustor and progressively decreases, reaching a minimum near the liners, regardless of the flight conditions and the longitudinal coordinate of the combustor. The average maximum temperature is reached over the sections near the end of primary combustion zone (PZ) [56] [57]. The fluid motion inside the combustor was simplified by assuming the flow lines exiting in the normal direction from the liners holes and directed toward the combustor outlet, following a trajectory similar to an equilateral hyperbola. PZ modeling significantly impacts the accuracy of emission models due to the high temperatures and considerable residence time of the flow. To the best of the authors' knowledge, the only PZ modeling found in the literature [52] [53] involves multiple 0D reactors, each characterized by an inlet mass flow and equivalence ratio.

One of the original contributions presented in this work is to investigate the use of a log-normal function as the equivalence ratio (ϕ) distribution for the PZ inlet, instead of the conventional Gaussian shape. The initial use of the Gaussian distribution was not based on experimental observations [58]. However, by defining its mean and variance, it can approximately model the inhomogeneities in the PZ. The log-normal distribution could indeed resemble a Gaussian shape but has the advantage of being defined only over the positive ϕ interval.

The emission model was validated using six data points from NASA's APEX [59] and ACCESS [40] full-scale engine test campaigns. These tests were conducted with a CFM56-2-C turbofan model at sea level and cruise altitude, covering various throttle (or power) levels. APEX tests used only JP-8 (with varying sulfur content), whereas ACCESS tests included both JP-8 and a blend of CAM-HEFA + JP-8. The APEX database offers a vast array of experimental data on gaseous chemical species, polycyclic aromatic hydrocarbons (PAHs), and EI_{SVF}, while the ACCESS database provides data only on carbon monoxide (CO), nitric monoxide (NO) and emission index of soot volume fraction (EI_{SVF}) for 3 different throttle levels.

This work is the first attempt to build a turbofan model potentially capable of estimating emissions from both SAF and conventional fuels under a wide range of operating conditions.

5.1 Methods

Section 5.1.1 introduces the composition of the JP-8 surrogate and the derivation process of the CAM-HEFA surrogate from laboratory test data. A brief exposition of the FGMech method is provided in Section 5.1.2, followed by an explanation of the rationale for selecting the base mechanism of small gas-phase species in Section 5.1.3. In Section 5.1.4,

the complete gas-phase kinetic mechanism is assembled, starting from FGMech and base mechanism, followed by the sub-mechanisms describing the formation of NO_x, SO_x, and PAHs. Next, the turbofan reactor network is presented in Section 5.1.5, detailing modifications from the state-of-the-art. Beginning with the design parameters, a CFM56-2-C1 performance model is built via GSP12 [60] [61], and part of the outputs are used for the formulation of model inputs (Section 5.1.6). The model parameters and inputs are then defined, and experimental data points for validation are listed (Section 5.1.7). Section 5.1.8 describes the choice and rationale of the equivalence ratio distribution inside the burner PZ.

5.1.1 Composition of JP-8 and CAM-HEFA fuels

The types of fuels studied in this work are conventional JP-8 and a blend of CAM-HEFA + JP-8 (50%:50% by volume). JP-8 represents a mixture of a broad class of hydrocarbons, including n-paraffins, iso-paraffins, cyclo-alkanes, and aromatics. It has been extensively studied, and a fair number of surrogates are available. The JP-8 surrogate selected for this study is POSF10264 [62]. For CAM-HEFA and CAM-HEFA + JP-8 blends, unlike JP-8, no widely validated surrogate models are currently available. This is due to the low level of standardization in the production processes of HEFA fuels (*e.g.*, different catalysts, temperatures, pressures, and times).

Therefore, the surrogate composition of CAM-HEFA + JP-8 blends was determined from U.S. Environmental Protection Agency (EPA) measurements, commissioned by the U.S. Air Force Research Laboratory, on samples of CAM-HEFA + JP-8 blends (50%:50% by volume) [63]. These measurements were conducted with two different EPA methods (EPA 8260-B [64] and EPA 8270-C [65]), resulting in the identification of different possible compositions. Specifically, Ref. [63] provides four sets of measurements: aromatic hydrocarbons and paraffins made by either EPA 8260-B or EPA 8270-C methods. Regarding aromatic hydrocarbon concentrations, only data from measurements using EPA 8270-C are considered. Measurements using EPA 8260-B show concentrations below the practical quantitation limit (PQL) for all detected species, which is the lowest level at which the method can confidently discern between two different values. For the aromatic hydrocarbons detected by EPA 8270-C, only those with concentrations above the PQL were considered. Paraffin concentrations, on the other hand, were obtained via EPA 8260-B because this composition provides a distillation curve in better agreement with the experimental distillation curve, as shown in Fig. 17. Because EPA methods require solvents for their implementation, the concentrations reported in [63] include both the mass of the solute (*i.e.*, fuel) and the solvent. To determine the relative composition of the species based solely on the mass of fuel, the compositions were normalized using the sum of the compositions of paraffins and aromatic hydrocarbons.

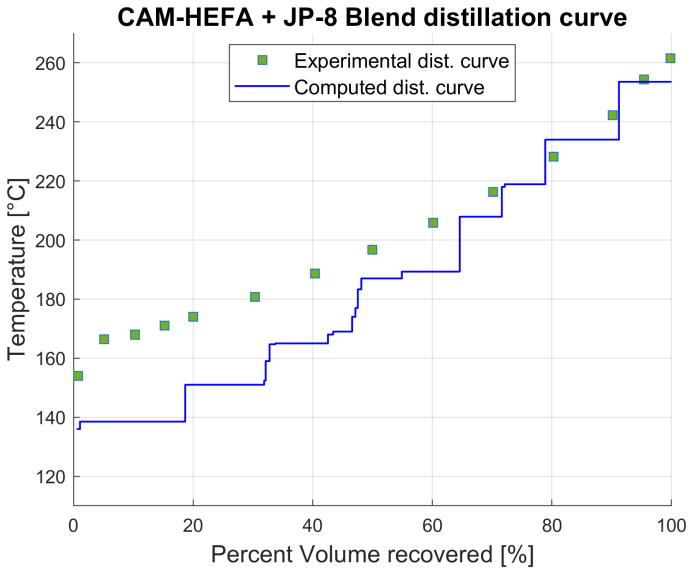

Figure 17: Comparison of experimental and computed distillation curves for CAM-HEFA + JP-8 blend.

5.1.2 FGMech combustion kinetic mechanism

The combustion chemistry of the fuels is described by combining an oxidative pyrolysis sub-mechanism for the fuel with an oxidation base mechanisms. The FGMech approach has been used to generate lumped, high-temperature, oxidative pyrolysis sub-mechanisms for each of the investigated fuels. According to this approach, the real-fuel is represented as a single surrogate species that matches the average molecular weight and atomic distribution of the blend. Subsequently, seven reactions are defined to describe the high-temperature decomposition of the surrogate species into smaller species: one reaction defines the unimolecular decomposition of the fuel; the remaining six reactions describe the pyrolysis promoted via hydrogen abstraction by six important species (*i.e.*, O_2, OH, H, HO_2, O, and CH_3). All reactions are lumped, representing all possible pathways of such reaction class. For the sake of simplicity, only the nine most relevant pyrolysis products in high-temperature combustion applications are considered, namely H radical, methyl radical, methane, ethylene, propylene, isobutylene, 1-butylene, benzene, and toluene. Products stoichiometric coefficients, reaction rates and thermodynamic and transport data are computed from the functional group distribution of the fuel as described in [45] and [46]. The fuel characterization is described in Section 5.1.1, the *BI* value, necessary for the FGMech calculation, can be found in [66]. Once the fuel oxidative pyrolysis is defined, the oxidation kinetic for the pyrolysis products is described adopting a base mechanism. The base mechanism chosen is the USC because, as shown in Section 5.1.3, it is better able to predict the experimental results of some soot precursors than AramcoMech 2.0 [47] and AramcoMech 3.0 [48].

The combustion kinetic mechanism used for all the considered fuels consists of a lumped, oxidative pyrolysis mechanism plus a base mechanism for the oxidation of smaller species and radicals. The lumped mechanism consists of 17 species and 7 reactions, and it is constructed from the composition of fuels identified in Section 5.1.1, via the FGMech approach by first calculating stoichiometric coefficients [45] and then kinetic parameters (A_{pre}, E_a, n) [46].

5.1.3 Selection of the base gas-phase mechanism

PAHs are soot precursors that play a key role in soot inception, nucleation, and growth [67]. To accurately predict these PAHs, the selection of a base gas-phase mechanism is crucial. The formation of the first aromatic ring (*i.e.*, benzene) is dominated by the self-recombination of propargyl radicals (C_3H_3) [68], and the PAH growth is mostly via hydrogen-abstraction-acetylene (C_2H_2)-addition (HACA) mechanism [69]. Therefore, the predictions of C_2H_2, allene (a-C_3H_4), and propyne (p-C_3H_4) compared to experimental measurements are important indicators for selecting the appropriate base mechanism. In this work, we chose AramcoMech 2.0 [47], AramcoMech 3.0 [48], and USC Mech II [49] as potential candidates for the base mechanism. Shock tube speciation data from JET-A oxidation [70] are used for the base mechanism validation. To the best of the authors' knowledge, no data has been reported for CAM-HEFA. Therefore, only JP-8 was considered for the analysis. Comparisons with shock tube data (Fig. 18), using a JET-A surrogate (POSF4658) at $\phi = 1.86$, $O_2 = 678ppm$ and $P = 16.3 - 23.1atm$, suggest that USC Mech II provides slightly better results and therefore was chosen as the base mechanism for our study. In these conditions, the maximum error occurs at a temperature of about $1400K$, and the error in the prediction of C_2H_2, a-C_3H_4, and p-C_3H_4, reaches a maximum factor of about 4.

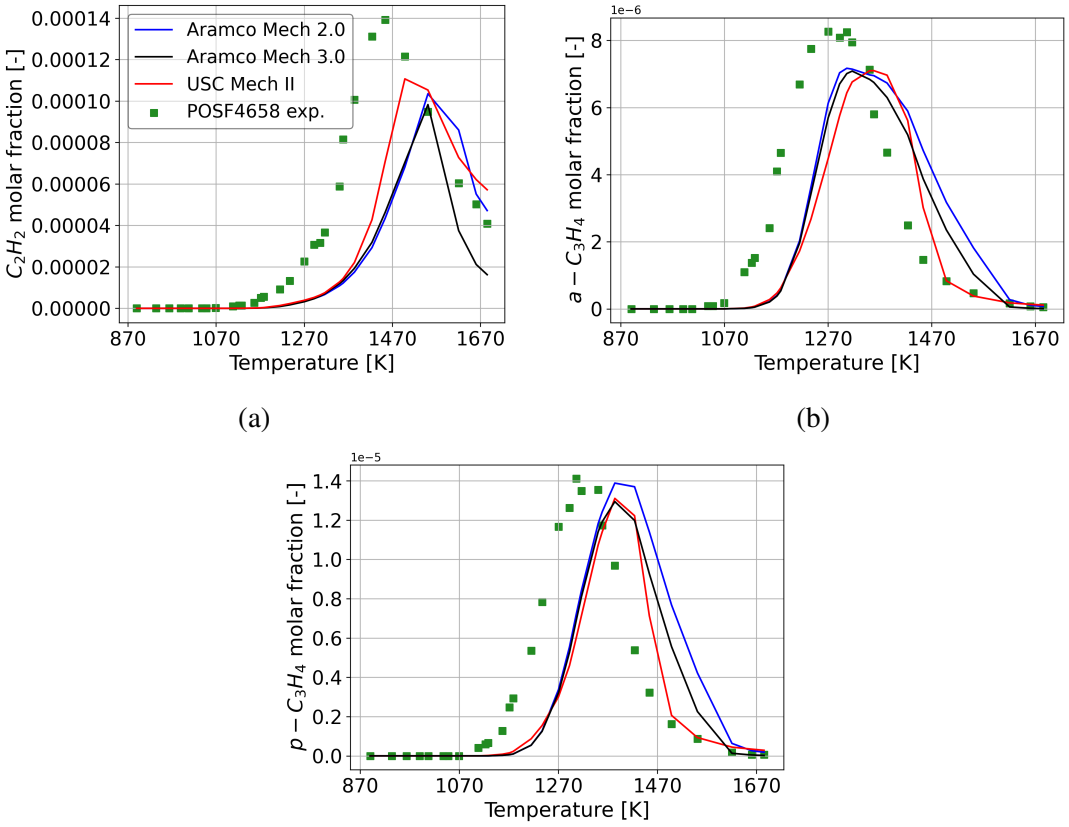

Figure 18: C_2H_2, a-C_3H_4 and p-C_3H_4 comparison with experimental data for JP-8.

5.1.4 Assembly of the overall kinetic mechanism

The gas-phase kinetic mechanism is obtained by combining the abovementioned FGMech submechanism and USC Mech II with a PAH mechanism [71] and additional chemistries for NO_x [50] and SO_x [51]. For simplicity, sulfur in the fuel is considered to be present in the form of atomic sulfur (S). The soot formation was predicted by the Particle Tracking model of Chemkin-Pro, using the ABF surface mechanism [72]. Particle dynamics is modeled by the method of moments. A free molecular coagulation regime, unit collision efficiency, and no particle aggregation were assumed. These settings were found to be of little influence in the current study since the focus is on the soot volume fraction and not on the number of particles. Soot inception, absorption, HACA growth, and oxidation were included in the surface mechanism. The overall kinetic mechanism consists of 236 gas-phase species, 1416 gas-phase reactions and 14 surface reactions.

5.1.5 Turbofan equivalent reactor network

The construction of the turbofan reactor network, as shown in Fig. 19, started from the baseline network in Ref. [53], which was subsequently modified to better model the SAC (Fig. 20).

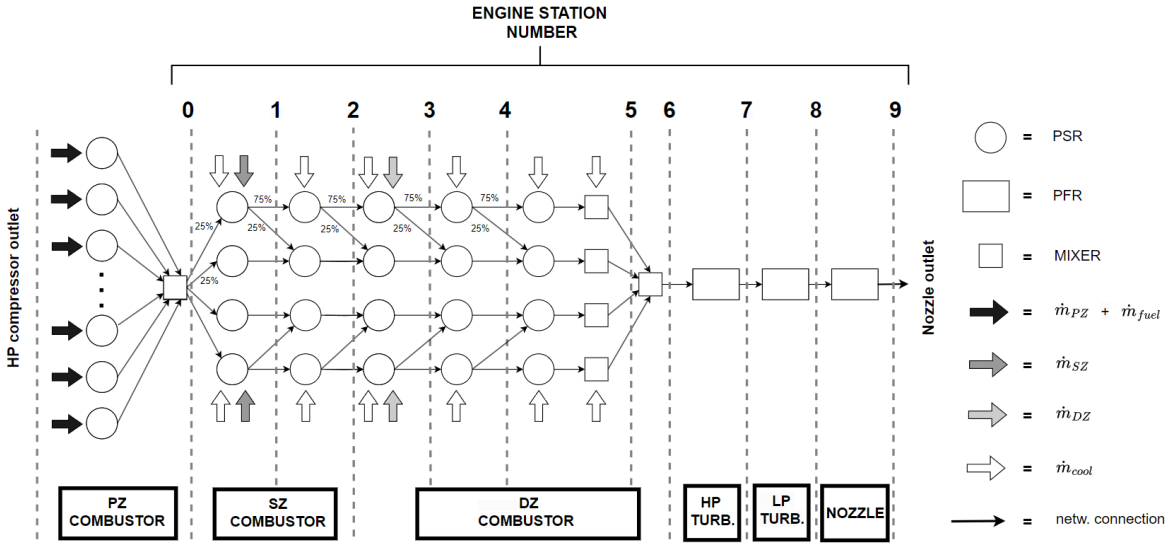

Figure 19: Turbofan reactor network representation and engine station numbering

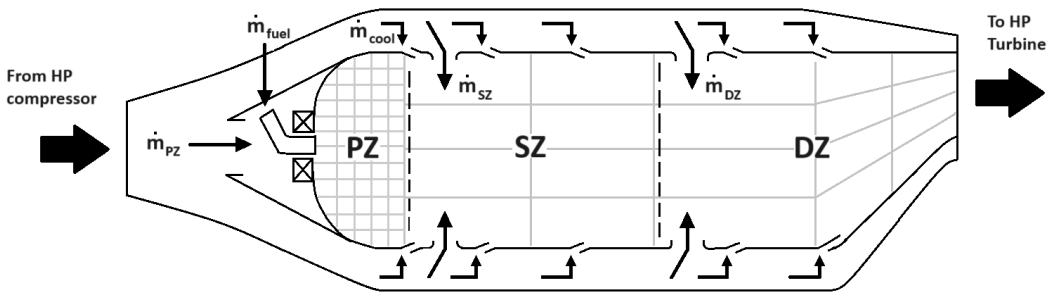

Figure 20: SAC section diagram

The PZ is represented by 60 PSRs in parallel. This number was chosen because a parametric study [53] performed in the range of 1 to 120 showed that 60 PSRs provide a good compromise between accuracy and computational cost. All the PSR reactors in the PZ supply their output flow to a mixer, which calculates their average properties and composition. The mixer then equally distributes the mass flow to each of the PSR reactors in the first part of the SZ.

The modifications mainly concern the architecture of the SZ and DZ, as well as the choice of ϕ distribution at the PZ inlet (explained in detail in Section 5.1.8). In the current configuration, the SZ and DZ are represented by four parallel rows of PSRs in series. The upper and lower outer rows each receive 50% of non-PZ mass flow rate (equal to $\dot{m}_{tot}$ - $\dot{m}_{PZ}$) coming from the last stage of the HP compressor. The 50% division is a simplification based on images of the CFM56-2-C1 combustor [57], which show that the outer liner DZ and SZ holes have approximately the same diameter as those in the inner liner. To facilitate convergence in solving the conservation equations of species, energy, and mass for the SZ and DZ PSRs, the mass flow distribution between the outer and inner liners was varied by a maximum of about 5% under some operating conditions. It was also verified that this procedure only introduces small variances in the species concentration and temperature profiles at the outlet nozzle (see Fig. 73 in the Appendix).

The non-PZ mass flow rate is divided (Fig. 20) into secondary combustion ($\dot{m}_{SZ}$ in Fig. 20), dilution ($\dot{m}_{DZ}$ in Fig. 20) and cooling mass flow rate ($\dot{m}_{cool}$ in Fig. 20). While the $\dot{m}_{SZ}$ participate in the combustion process, the $\dot{m}_{DZ}$ and the $\dot{m}_{cool}$ are meant to cool down the core flow and the burner liner, respectively. Note that while $\dot{m}_{cool}$ is equally distributed along all outer PSRs, the mass flow rates $\dot{m}_{SZ}$ and $\dot{m}_{DZ}$ are provided as input only to the 1° and 3° PSRs columns, respectively. In this reactor network architecture, the two outer rows of PSRs supply partially combusted air to the two inner rows, as shown in Fig. 19. Each PSR in the outer row divides the flow into two parts: 75% of the mass flow rate is supplied to the next PSR in the same row, while the remaining 25% is supplied as input to the nearest PSR present in the adjacent inner row. This flux distribution (75%-25%) was chosen to achieve a radial temperature profile (with reference axis passing through the atomizer centerline) comparable to that observed in CFD simulation of a similar SAC under near-cruise conditions [56].

Lastly, the afterburner zones (HP turbine, LP turbine and nozzle) are modeled with a series of PFRs.

5.1.6 CFM56-2-C1 offdesign performace

To generate some of the reactor network inputs and parameters, it is necessary to obtain the off-design performance of the CFM56-2-C1 turbofan using GSP12 software. GSP12 is a software used for simulating stationary and transient performance of a wide variety of gas turbine configurations, with components represented by nonlinear equations or maps (especially for rotary components). The results provided by GSP12 are close to those provided by other commercial software such as GasTurb [22] or Matlab implementable algorithms [73]. To obtain the off-design-performance, a dual-spool turbofan model was initially created in GSP12, and then supplied with the CFM56-2-C1 design parameters found in [59] (summarized in Table 13) and the Mach numbers of the flow at each engine station (Table 14).

Table 13: CFM56-2-C1 design parameters

F $[KN]$	OPR $[adim]$	π_f $[adim]$	$\pi_{LPcompr}$ $[adim]$	$\pi_{HPcompr}$ $[adim]$	α $[adim]$
98.0	23.5	1.61	2.84	11.43	6.0

Table 14: Mach at the component inlet and isoentropic efficiencies (on design condition)

Type	Fan	Compressor	Burner	HP turbine	LP turbine	Byp./core nozzle
Ma	0.40	0.40	0.40	0.40	0.30	0.40
η	0.85	0.85	-	0.90	0.90	-

The GSP turbofan model requires defining the isoentropic efficiencies of the fan, LP compressor, HP compressor, HP turbine, and LP turbine. These values were derived from the typical values of older turbofan generations [74] and are reported in Table 14. The design condition coincides with the static operating conditions of $Ma_0 = 0$, $z = 0m$, and $f = 0.0188$. The value of f was calculated to obtain the amount of F in Table 13. One relevant output provided by the design phase is the inlet/outlet area of turbofan components, as shown in Table 15.

Table 15: Turbofan model sections area

A_{tHP} inlet $[cm^2]$	A_{tLP} inlet $[cm^2]$	A_e inlet $[cm^2]$	A_e outlet $[cm^2]$
574	1236	3516	3490

5.1.7 Reactor network parameters and inputs

The operating conditions used to validate the model are shown in Table 16. Table 16 also provides the nomenclature of the different APEX and ACCESS data points with details on the flight speed, altitude and power level. The flight conditions were chosen to cover as much as possible the range of operating conditions typically experienced by a turbofan. The JP-8 fuel used in the chosen APEX data points has a sulfur content of 1595 ppm.

Table 16: Nomenclature for APEX and ACCESS test conditions

Flight condition	Ma_0 $[adim]$	z $[m]$	Power [%]	ID	Fuel type
7% APEX	0	0	7%	807**	JP-8
30% APEX	0	0	30%	813**	JP-8
100% APEX	0	0	100%	816**	JP-8
Low power ACCESS	0.6	10600	Low*	-	JP-8 + CAM-HEFA
Medium power ACCESS	0.6	10600	Medium*	-	JP-8 + CAM-HEFA
High power ACCESS	0.6	10600	High*	-	JP-8 + CAM-HEFA

*Note: for ACCESS experiments the power level is not precisely quantified
**Note: number identifying the dataset point in [59]

The reactor network is defined from a significant amount of data, which are divided into network parameters (Table 17 and Table 18) and network inputs (Table 19 and Table 20).

Table 17: Reactor network parameters for different thrust setting in APEX conditions

Input type	7% APEX	30% APEX	100% APEX
P_{comb} $[Pa]$	$2.96 \cdot 10^5$	$7.28 \cdot 10^5$	$1.647 \cdot 10^6$
T_{comb} $[K]$	485.9	616.6	775
f $[adim]$	0.0120	0.0122	0.0192
$\dot{m}_{fuel}$ $[\frac{Kg}{s}]$	0.112	0.277	0.835

Table 18: Reactor network parameters for different thrust setting in ACCESS conditions

Input type	Low power ACCESS	Medium power ACCESS	High power ACCESS
P_{comb} $[Pa]$	$4.65 \cdot 10^5$	$5.09 \cdot 10^5$	$6.06 \cdot 10^5$
T_{comb} $[K]$	565	588	645
f $[adim]$	0.0148	0.0165	0.0205
$\dot{m}_{fuel}$ $[\frac{Kg}{s}]$	0.231	0.280	0.373

Table 19: Reactor network inputs for different thrust setting in APEX conditions

Input type	7% APEX	30% APEX	100% APEX
$\dot{m}_{PZ}$ $[\%]$	24.40	24.40	24.40
t_{PZ} $[msec]$	1.5	2.3	2.5
$\dot{m}_{SZ}$ $[\%]$	25.76	25.76	25.76
t_{SZ} $[msec]$	0.8*	0.8*	0.8*
$\dot{m}_{DZ}$ $[\%]$	21.82	21.82	21.82
t_{DZ} $[msec]$	0.8*	0.8*	0.8*
$\dot{m}_{cool}$ $[\%]$	28.01	28.01	28.01

*Note: 0.3 for PSR near SZ holes

Table 20: Reactor network inputs for different thrust setting in ACCESS conditions

Input type	Low power ACCESS	Medium power ACCESS	High power ACCESS
$\dot{m}_{PZ}$ $[\%]$	24.40	24.40	24.40
t_{PZ} $[msec]$	2.3	2.1	2.2
$\dot{m}_{SZ}$ $[\%]$	25.76	25.76	25.76
t_{SZ} $[msec]$	0.8*	0.8*	0.8*
$\dot{m}_{DZ}$ $[\%]$	21.82	21.82	21.82
t_{DZ} $[msec]$	0.8*	0.8*	0.8*
$\dot{m}_{cool}$ $[\%]$	28.01	28.01	28.01

*Note: 0.3 for PSR near SZ holes

The difference between the two types of data lies in the fact that parameters are known with a low margin of uncertainty, whereas inputs have substantially higher error ranges. Unlike the directly provided APEX parameters [59], the ACCESS parameters, except for $\dot{m}_{fuel}$, were obtained using the model detailed in Ref. 5.1.6, by calculating the off-design performance at the ACCESS flight conditions (expressed in Table 38). The GSP12 turbofan model also provides the pressure ratios of turbines and nozzles (π_{tHP}, π_{tLP}, π_e) for both APEX (Table 21) and ACCESS (Table 22), which are necessary to determine the pressure profile (assumed to be linear) of the PFRs in the reactor network (see Fig. 19).

Table 21: Pressure ratios provided by GSP12 off-design performance for APEX

Input type	7% APEX	30% APEX	100% APEX
π_{tHP} $[adim]$	2.86	2.89	3.13
π_{tLP} $[adim]$	2.27	2.33	4.01
π_e $[adim]$	1.05	1.05	1.21

Table 22: Pressure ratios provided by GSP12 off-design performance for ACCESS

Input type	Low power ACCESS	Medium power ACCESS	High power ACCESS
π_{tHP} $[adim]$	3.16	3.15	3.13
π_{tLP} $[adim]$	4.67	4.93	5.18
π_e $[adim]$	1.34	1.44	1.61

The network inputs consist of data related to the residence times in the PZ, SZ, and DZ (t_{PZ}, t_{SZ} and t_{DZ}), as well as how the mass flow is distributed across the combustion chamber. The t_{PZ} was calculated for each operating point (Table 16) using Eq. (29) (see Eq. (43) and Eq. (44) in the Appendix for more details on the derivation), $V_{PZ} = 8300cm^3$ [53], and assuming an average temperature within the PZ (see Table 23 and Table 24). The values of T_{PZ} for the APEX data points were obtained from the modeling results in Ref. [53] and were assumed to be the same for ACCESS conditions, as T_{PZ} depends more on engine speed than on z and Ma_0. The results show that the maximum estimation error of T_{PZ} for the data in Table 23 is approximately 25% (see Section 5.2.2). Consequently, this results in a maximum estimation error of about t_{PZ} of 25%, which is deemed acceptable for the present work.

Table 23: PZ mean temperature in APEX for t_{PZ} calculation

Input	7% APEX	30% APEX	100% APEX
T_{PZ} $[K]$	1500	1700	2000

Table 24: PZ mean temperature in ACCESS for t_{PZ} calculation

Input	Low power ACCESS	Medium power ACCESS	High power ACCESS
T_{PZ} $[K]$	1500	1700	2000

$$t_{PZ} = \frac{P_{PZ} \cdot V_{PZ}}{\bar{R} \cdot T_{PZ} \cdot \dot{m}_{PZ}} \tag{29}$$

The calculations using Eq. (29) yield values of t_{PZ} as shown in Table 19 and Table 20, which remain nearly constant with the throttle, except in APEX at idle. Note that although the calculated value of t_{PZ} at idle is $1.1msec$, considerations for convergence led to the choice of a slightly higher value of $1.5msec$. The values of t_{SZ} and t_{DZ} were chosen to obtain t_{tot} in the combustion chamber equal to around $6msec$, close to the values used in [53] and [52], and in line with the data for similar combustors [75]. The estimation of mass flow distribution in the combustion chamber was formulated based on data from the F101 PV combustor [75], which were subsequently adjusted to incorporate additional information on the CFM56-2-C1 burner geometry [57]. In fact, Ref. [75] analyzes several variation of the

F101 PV combustor, among which one (denominated SA-01) closely resembles the CFM56-2-C1 combustor. Through an experimental setup, the authors derived the mass flow rates shown in Table 25.

Table 25: Mass flows estimation from [75]

Mass flow type	Value
$\dot{m}_{PZ}$ [%]	24.40
$\dot{m}_{SZ} + \dot{m}_{DZ}$ [%]	47.58
$\dot{m}_{cool}$ [%]	28.01

Although Ref. [57] does not provide the exact sizes of SZ and DZ holes, it is possible to estimate from images that the diameter of the SZ holes is about $\frac{1}{3}$ larger than that of the DZ holes, and the DZ holes are about 50% more numerous than the SZ holes. Using this data, it is therefore possible to estimate that the total area ratio of SZ to DZ holes for the entire combustor is approximately 1.18. This ratio allows us to proportionally distribute the flow $\dot{m}_{SZ}+\dot{m}_{DZ}$ (see Table 25), resulting in the values shown in Table 19 and Table 20. The values of the mass flow rates are consistent with those found in Ref. [76] for CFM56 combustor, where $\dot{m}_{PZ}$, $\dot{m}_{SZ} + \dot{m}_{DZ}$ and $\dot{m}_{cool}$ are 25%, 45% and 30% respectively. Similar values were also reported for other types of SAC combustor [77]. Finally, to complete the definition of the network parameters, it is necessary to make an assumption about the lengths of the PFRs. The lengths, shown in Table 26, are the same as in Ref. [53]. These values can be justified based on the total length of the turbofan [78], considering the relative size of each component as observed from available images of the CFM56-2-C1 engine.

Table 26: Turbofan model components length

L_{tHP} [cm]	L_{tLP} [cm]	L_e [cm]
12	30	69

5.1.8 Criteria for selection of equivalence ratio distribution function

Unlike the previous literature, which extensively employs a Gaussian ϕ_{PZ} distribution [53] [52], this model opts for a log-normal distribution. This choice offers a similar shape but with the significant advantage of being defined over the domain of ϕ_{PZ} between 0 and $+\infty$, excluding all negative values. In practice, to minimize the area under the Gaussian function for $\phi_{PZ} < 0$, moderate values of $\bar{\phi}_{PZ}$ and standard deviation are required. However, these constraints could potentially limit the modeling of certain ϕ_{PZ} distributions. Another justification for using the log-normal distribution is its similarity in shape to the Gaussian distribution. This ensures that for the same $\bar{\phi}_{PZ}$ and variance, the model outputs remain comparable. The log-normal function (Eq. (30)) is established through the parameter μ (function of σ), chosen as in Eq. (31), where $\bar{\phi}_{PZ} = \frac{f}{f_{stoich}}$.

$$\phi(x) = \frac{1}{x\sigma\sqrt{2\pi}} \exp\left[-\frac{(\ln(x)-\mu)^2}{2\sigma^2}\right] \tag{30}$$

$$\mu = \log\left(\bar{\phi}_{PZ}\right) - \frac{\sigma^2}{2} \tag{31}$$

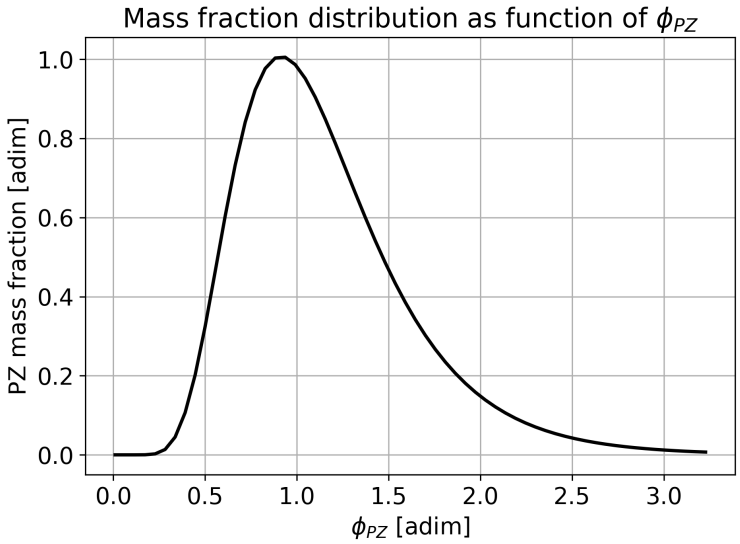

Figure 21: Log-normal mass fraction distribution as function of local ϕ_{PZ}

The σ parameter served as the sole tuning parameter for the emission model, with its values detailed in Table 27 and Table 28. These values indicate that at high engine speeds in APEX conditions, the variance of σ is noticeably increased, resulting in regions within the PZ where combustion occurs at substantial higher values of ϕ.

Table 27: σ values under APEX operating conditions

Input	7% APEX	30% APEX	100% APEX
σ	0.40	0.40	0.85

Table 28: σ values under ACCESS operating conditions

Input	Low power ACCESS	Medium power ACCESS	High power ACCESS
σ	0.40	0.40	0.40

5.2 Results

In Section 5.2.1, the emission model is validated against local burner temperature profiles obtained using CFD simulations. In Sections 5.2.2 and 5.2.3, the model is validated using six data points from APEX and ACCESS NASA database. These data points represent a wide range of engine RPMs at sea-level and cruise altitude, and include a variety of pollutant species as well as nozzle exhaust temperature. In the figures presented in Sections 5.2.2 and 5.2.3, only the end state (output conditions) of the gases for each reactor (PSR or PFR) within the network is shown. The spatial coordinate refers to the engine station nomenclature depicted in Fig. 19.

5.2.1 Model validation against CFD data

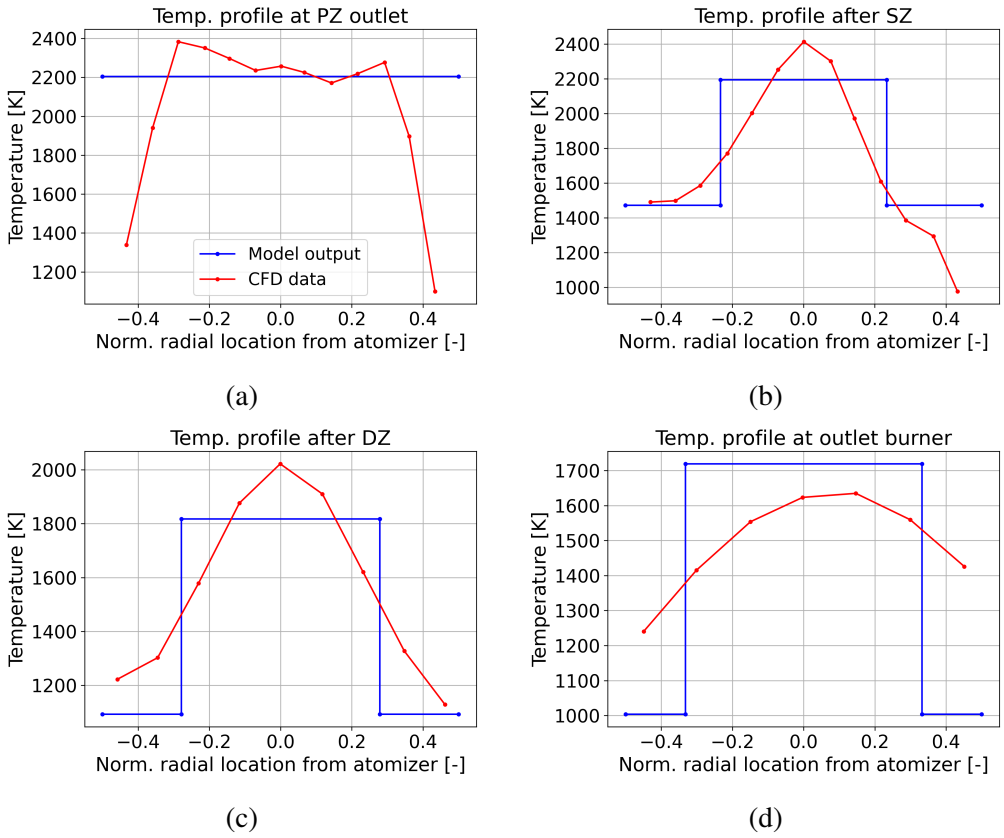

Figure 22: Validation plot on CFD simulations at $z = 12Km$, $Ma_0 = 0.6$ and $f = 0.025$ (Case 1)

Comparison between model output and CFD data for Case 1 and Case 2 condition (Table 55) are given in Fig. 22 and in Appendix (Fig. 80) respectively. CFD data for Case 1 and Case 2 are obtained from normalized temperature profiles found in Ref. [56]: from these the actual temperature profiles were derived assuming an average combustor inlet and outlet temperature of $660K$ and $1550K$ respectively, consistent with high operating regimes for the CFM-56-2C. To plot the temperature profile of the present model as a function of the radial coordinate (i.e. the distance from the atomizer centerline), the assumption of mass flow uniformity was made for the combustor sections in Fig. 22. The analysis of Fig. 22a reveals that the temperature at the PZ outlet section is almost constant at an average value of about $2200K$, except for the regions very close to the inner and outer liners. This is accurately represented in the model with a single flow at $2200K$.

For the SZ outlet section (Fig. 22b), the model provides flows with temperatures of approximately $2200K$ and $1480K$, with a mass flow split of 46.61% and 53.39%, respectively. The modeling of the SZ outlet flow is therefore in agreement with data from CFD although the intermediate temperatures between the peak and minimum temperatures are not represented in the model.

Similar considerations also apply to the DZ outlet temperature profile shown in Fig. 22c. The temperature profile leaving the combustor shows less homogeneity compared to the CFD data, with higher estimation errors particularly near the liners (Fig. 22d). However,

this substantial error is partially mitigated by the fact that the low-temperature airflow at the burner outlet constitutes only about 33.56% of the total air flow rate. From Fig. 22, a potential improvement to the model could involve increasing the number of PSR rows (in the SZ and DZ) to better align with the detailed temperature profiles obtained from CFD simulations. Validation of the temperature profiles conducted on Case 2 dataset (see Appendix for more datails) led to results and considerations similar to those of Case 1.

5.2.2 Model validation on APEX dataset

In this Section, only select species are presented, while others are detailed in the Appendix to streamline the manuscript.

The species listed in the Appendix are ethylene (C_2H_4), butadiene (C_4H_6), ethane (C_2H_6), propane (C_3H_8), methanol (CH_3OH), and oxygen (O_2). For these species, the concentration at the outlet is predicted with a margin of error of less than two orders of magnitude except for C_3H_8 for high and medium engine speeds (100% APEX) where the error is about 2.5 orders of magnitude. The trends of C_2H_4, C_4H_6, and CH_3OH for medium and low throttle values are found to be in agreement with experimental trends. For C_2H_4 there is a general tendency to overestimate the output concentration while the opposite occurs for C_3H_8.

The model correctly reproduces the temperature trend (Fig. 23) observed in turbofan, with an almost monotonically decreasing temperature until the nozzle outlet and a maximum peak near the PZ outlet. The high and low temperature zones within the combustor, identified by the PSR reactors inner and outer row (Fig. 19) in SZ and DZ zones, are qualitatively represented and have a difference of about $500K$ to $600K$ regardless of the flight condition. The efflux temperature turns out to be approximately $200K$ to $300K$ lower than the experimental data, and this can be attributed in part to the use of higher-than-actual π values for turbines and nozzle: these numerical lower-than-expected values are found to be in line with the data predicted by the model in [53], which gives efflux temperatures in the range of about $750K$ to $600K$. However, several tests, performed with the present model, have shown that the use of moderately lower π values provides similar results in terms of gas species and soot production. The decrease in π would in fact lead to a decrease in the temperature ratio of the component and thus to an increase in temperatures: nevertheless, these temperatures would be at most equal to $1000K$ with very limited effect on the formation of the various pollutants.

Performance in predicting carbon-based species, specifically carbon dioxide (CO_2), methane (CH_4), and CO, is satisfactory (Fig. 24 to Fig. 26) with an estimation error substantially exceeding one order of magnitude only in the case of 7% APEX for CH_4 and 100% APEX for CO. The CH_4 outlet concentrations are predicted with one order of magnitude error and their trend is in very good agreement with experimental values (increasing concentration with decreasing throttle). The outlet concentration of CO remains almost constant as the throttle decreases in opposition to an increasing experimental trend. The error on CO ranges from a minimum of 0.5 (7% APEX) to 1.5 (100% APEX) order of magnitude. The concentration of CO_2 at the nozzle outlet is constant as the throttle changes, and this is in agreement with the experimental data (Fig. 25), with differences on the order of a few 10^{-2}. For soot precursors (C_2H_2) the maximum error results in about one order of magnitude and the model predicts a slight increase in concentration at the outlet as power decreases versus an almost constant experimental trend (Fig. 31).

The model turns out to correctly predict the outlet concentration values of most relevant nitrogen oxides, namely NO, nitric dioxide (NO_2) and nitrous oxide (N_2O), for all data-

points tested with an error of less than an order of magnitude and a higher accuracy for NO and NO_2 compared to N_2O (Fig. 27 to Fig. 29). Experimental value of NO at outlet increase appreciably with temperature (and thus with throttle) while NO_2 and N_2O concentrations remain almost constant. The computed NO and NO_2 trend accurately follows the experimental trend while the computed N_2O trend shows a slight decrease as throttle decreases against an almost constant experimental trend.

The concentration of sulfur dioxide (SO_2) on the efflux section turns out to be almost constant as the engine power varies, in line with the experimental trend (Fig. 30): the error is well below an order of magnitude. A correct prediction of SO_2 and other sulfur-based molecules appears to be relevant in understanding the mechanisms of nucleation and growth of ice crystals forming contrails. Some findings suggest that an increase in sulfur content causes more but smaller ice particles [79]: the increase in number density of a high sulfur fuel can reach a factor of 2 compared to a low sulfur fuel. The value of EI_{SVF} at the outlet decreases with decreasing power, except for very low throttle level where is constant. The EI_{SVF} prediction error ranges from about 1.5 (7% APEX) to 2.5 (100% APEX) orders of magnitude.

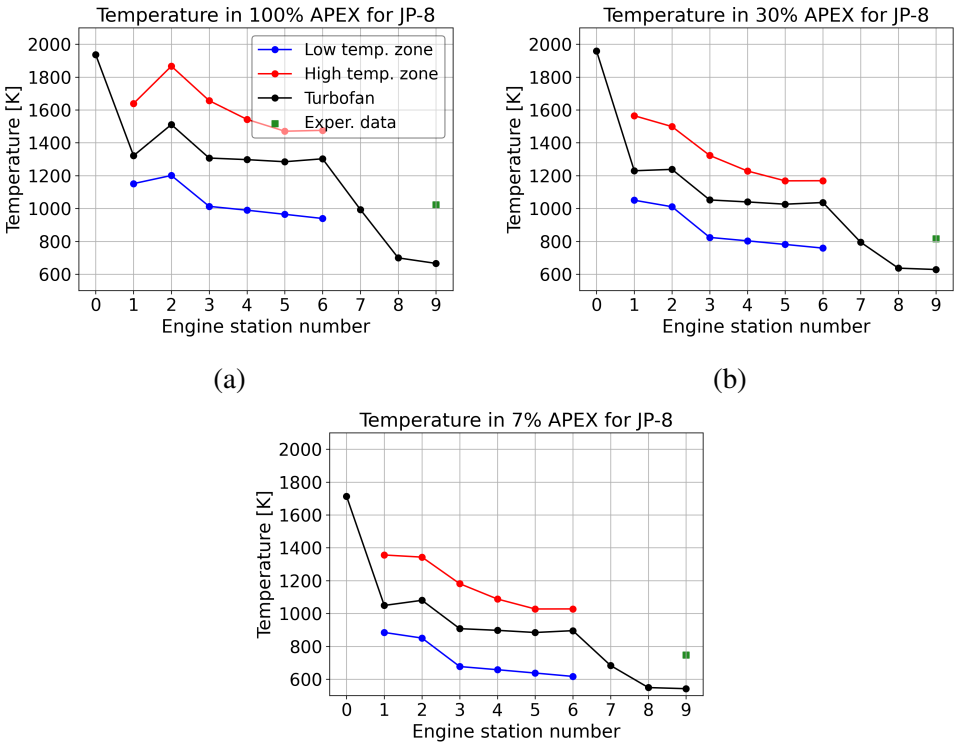

Figure 23: Temperature profile in APEX conditions for decreasing throttle

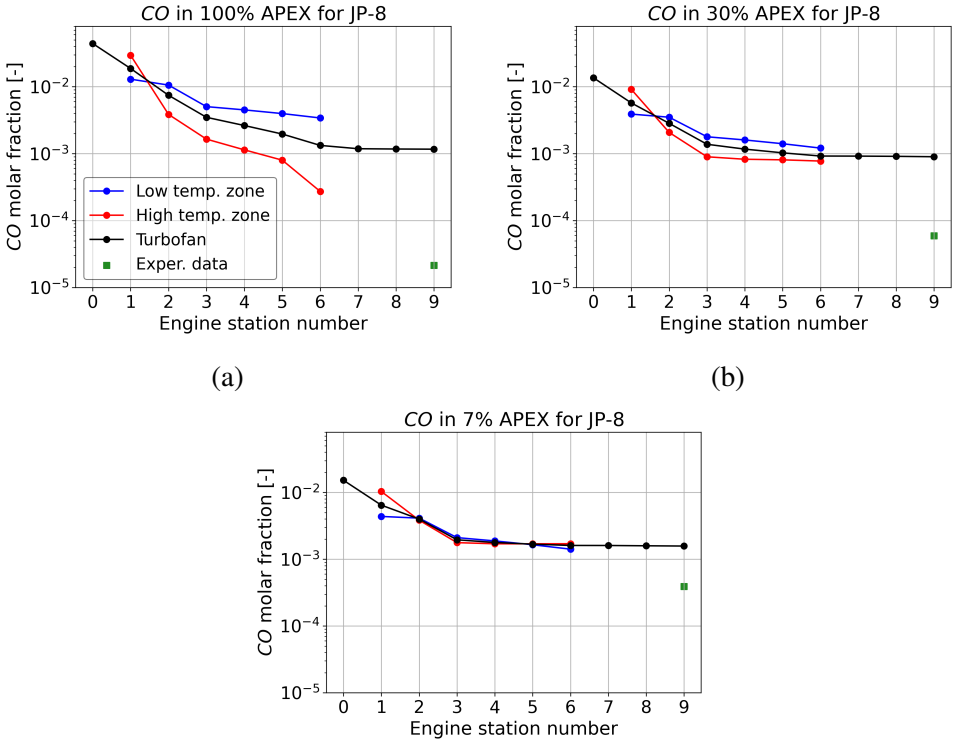

Figure 24: CO concentration profile in APEX conditions for decreasing throttle

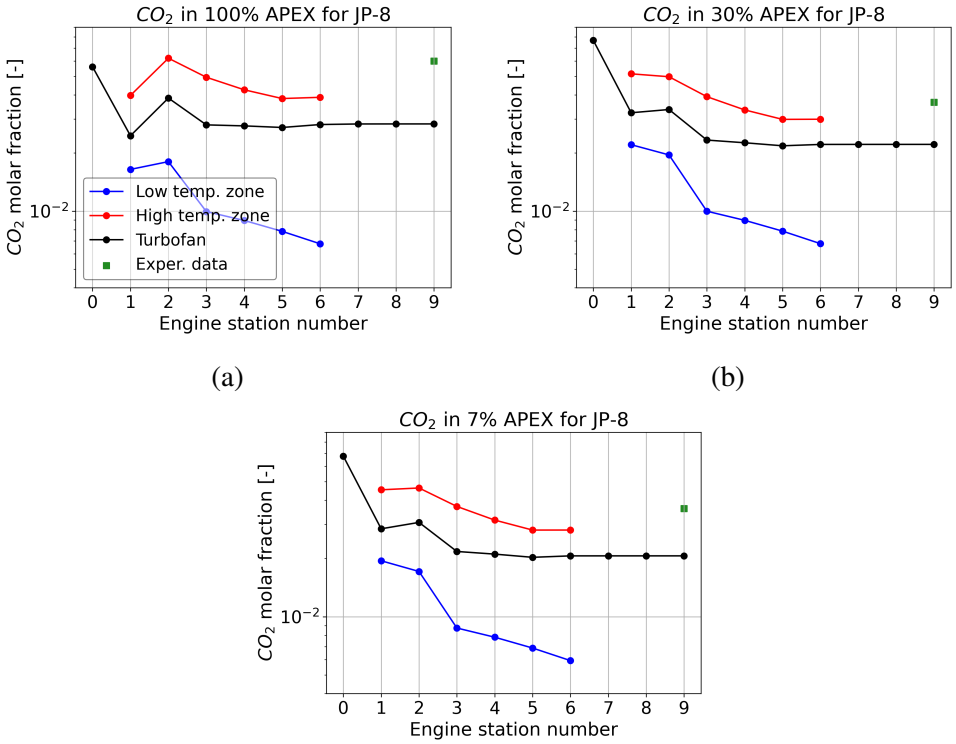

Figure 25: CO_2 concentration profile in APEX conditions for decreasing throttle

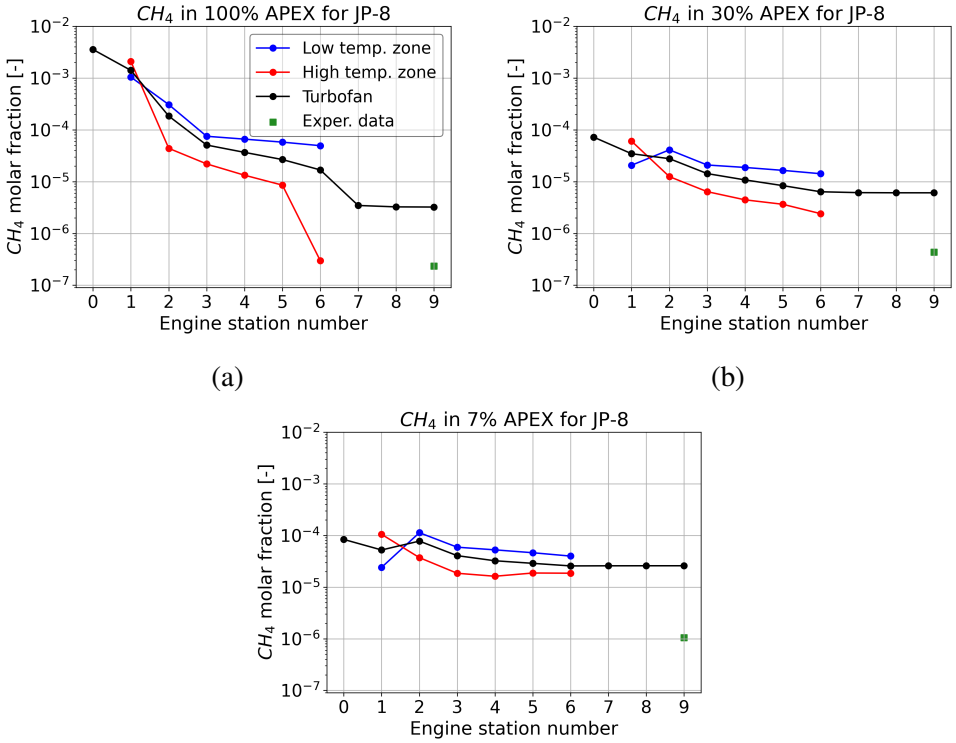

Figure 26: CH_4 concentration profile in APEX conditions for decreasing throttle

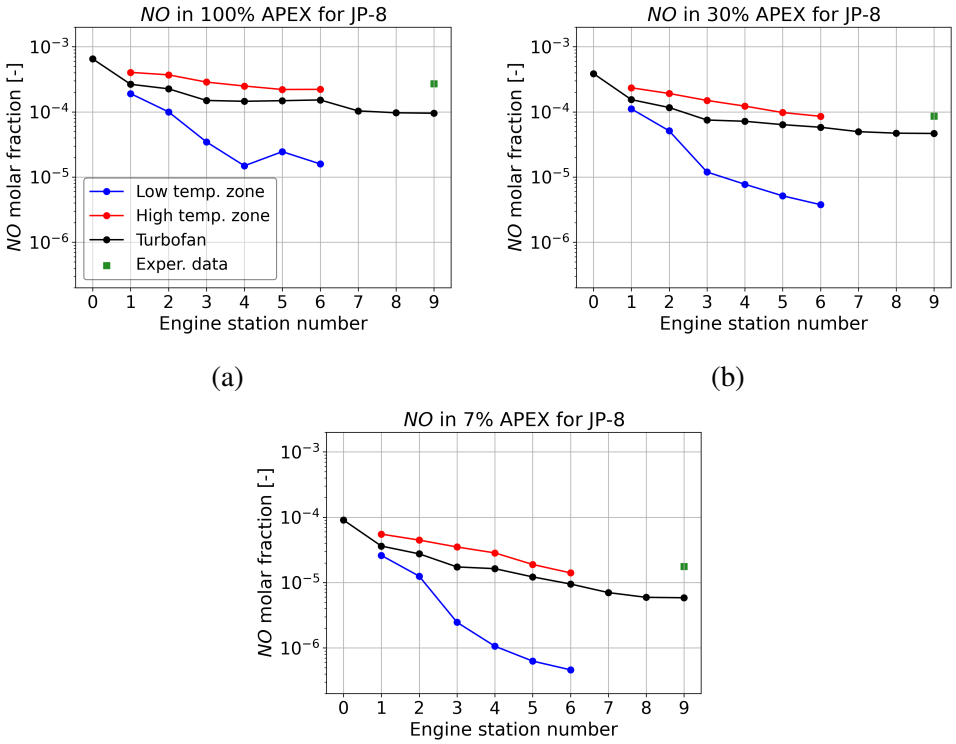

Figure 27: NO concentration profile in APEX conditions for decreasing throttle

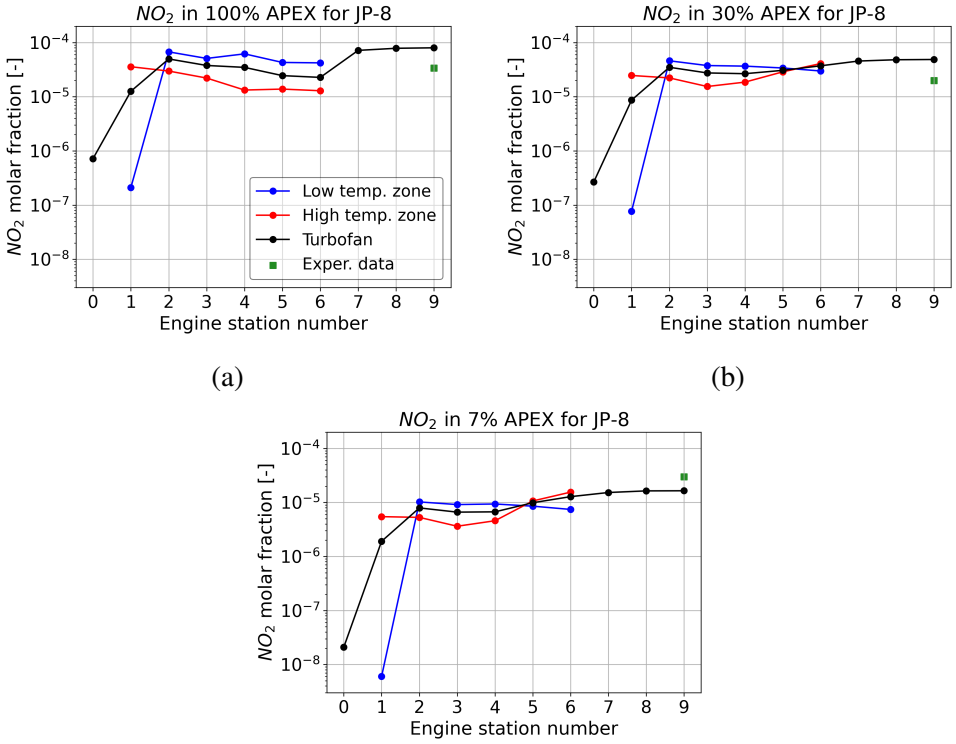

Figure 28: NO_2 concentration profile in APEX conditions for decreasing throttle (to the right)

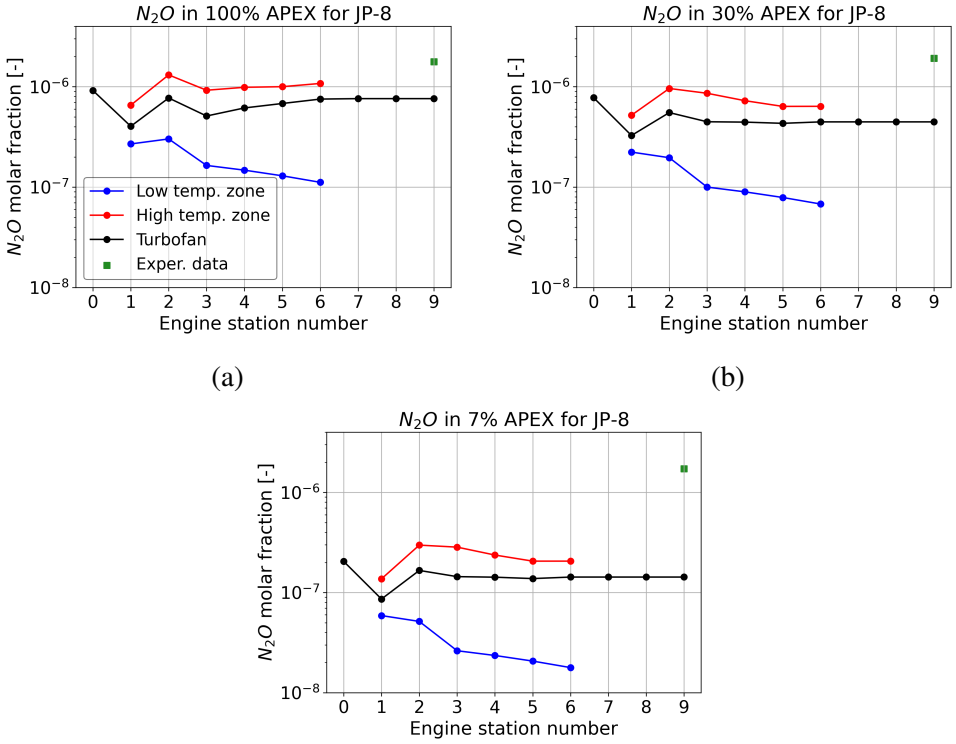

Figure 29: N_2O concentration profile in APEX conditions for decreasing throttle

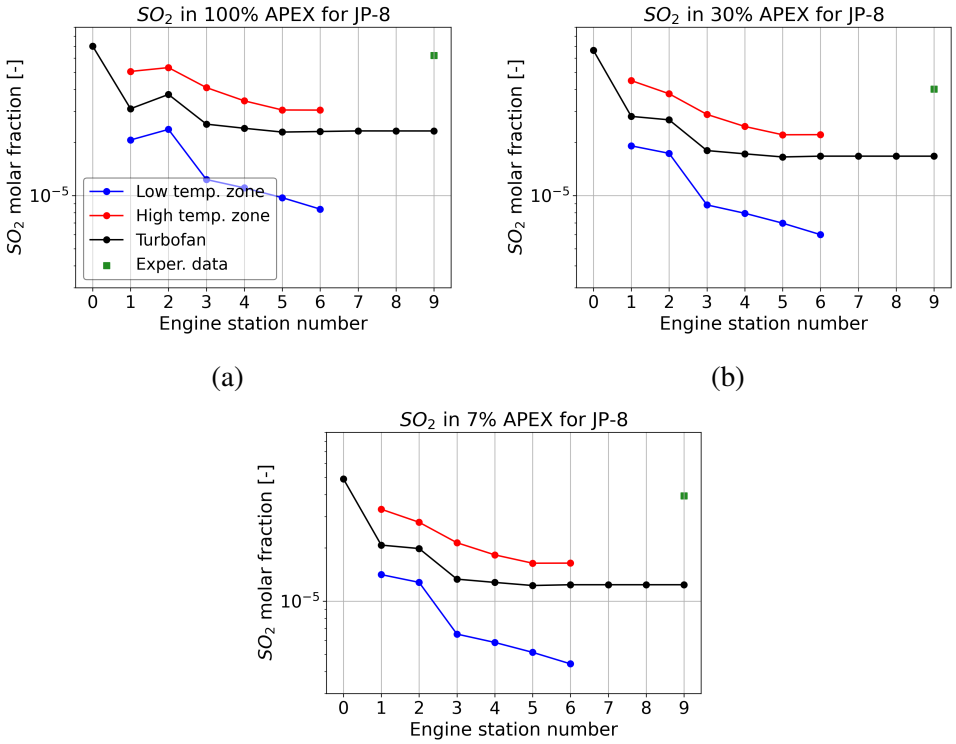

Figure 30: SO_2 concentration profile in APEX conditions for decreasing throttle

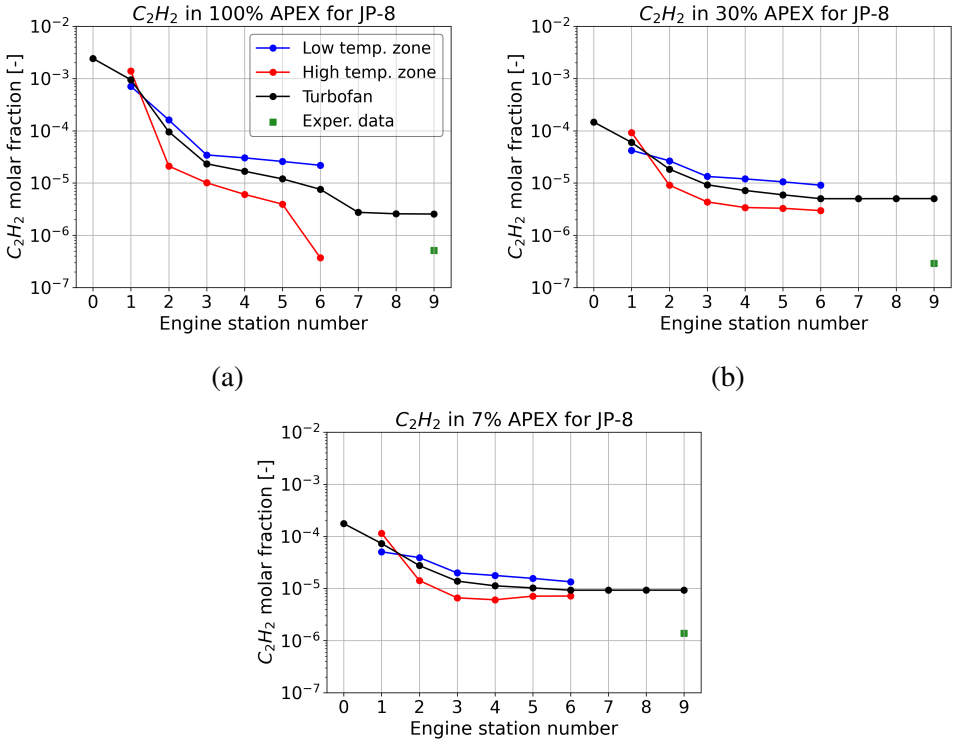

(a) (b)

(c)

Figure 31: C_2H_2 concentration profile in APEX conditions for decreasing throttle

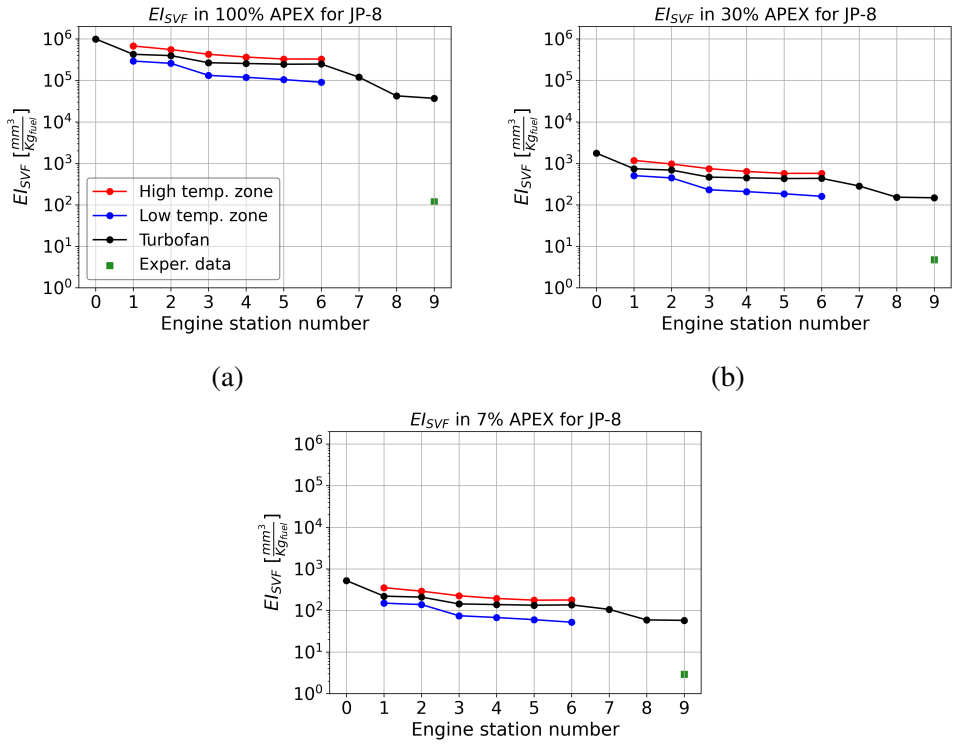

(a) (b)

(c)

Figure 32: EI_{SVF} profile in APEX conditions for decreasing throttle

Overall, the model has comparable performance with the reference model built in [53]. The accuracy in predicting the concentrations of CO_2, NO, and SO_2 is very close to the reference model; the model also succeeds slightly better in predicting the concentrations of NO_2 and has significantly better performance in estimating C_2H_2. Errors in the estimation of CO, N_2O and EI_{SVF} are higher than the reference model. However because the reference model was not tested for the species in the Appendix it was not possible to make a full comparison of performance. Some tests conducted on current model showed greater sensitivity from the PZ parameters (t_{PZ}, $\dot{m}_{PZ}$) than those of SZ and DZ. Model sensitivity from turbine and nozzle parameters (π) was found to be marginal due to relatively low temperatures.

5.2.3 Model validation on ACCESS dataset

Testing the model on the operating conditions of the ACCESS dataset shows overall a slight increase in CO (Fig. 33) and decrease in NO (Fig. 34) concentrations at the outlet with increasing throttle against a roughly constant experimental trend. As is well known, decreasing the throttle of a turbofan leads to an increase in CO concentrations and a decrease in NO [74], and this is also confirmed by the results obtained in Section 5.2.2: this deviation in experimental data can be in part explained by the high uncertainty in estimation of concentration [40], due to the fact that sampling of turbofan exhaust occurs several tens of meters away, with possible dilution of the wake. The use of JP-8 instead of CAM-HEFA + JP-8 in ACCESS conditions has been tested and found not to appreciably influence NO and CO outlet concentration values: these considerations are in line with experimental results. Therefore, in the following only CAM-HEFA blend results are provided.

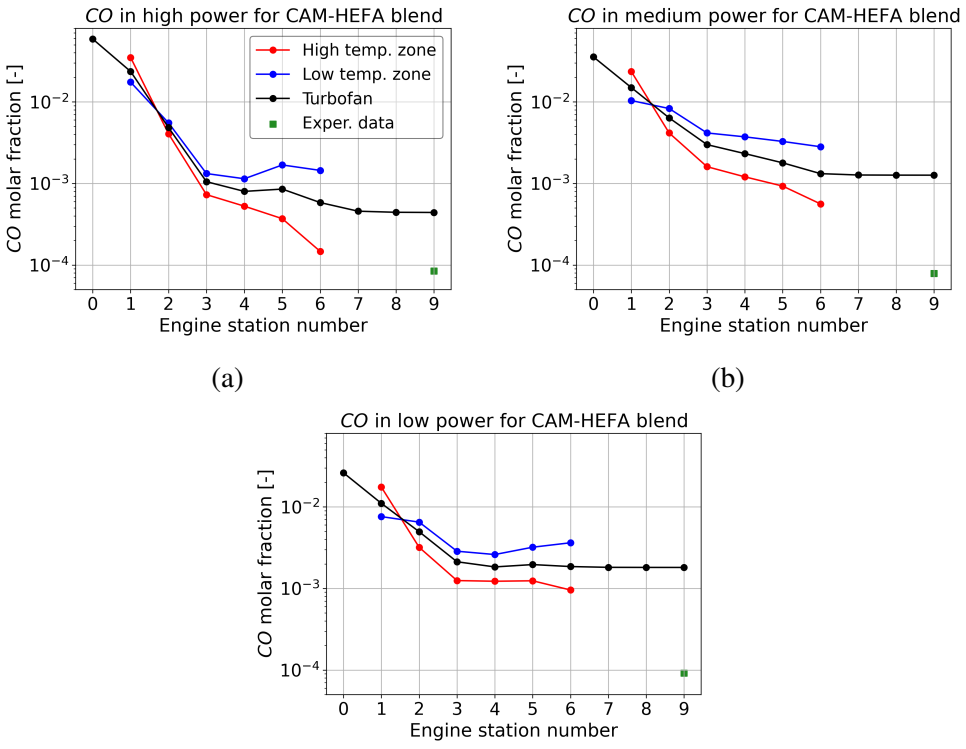

Figure 33: CO concentration profile in ACCESS conditions for decreasing throttle

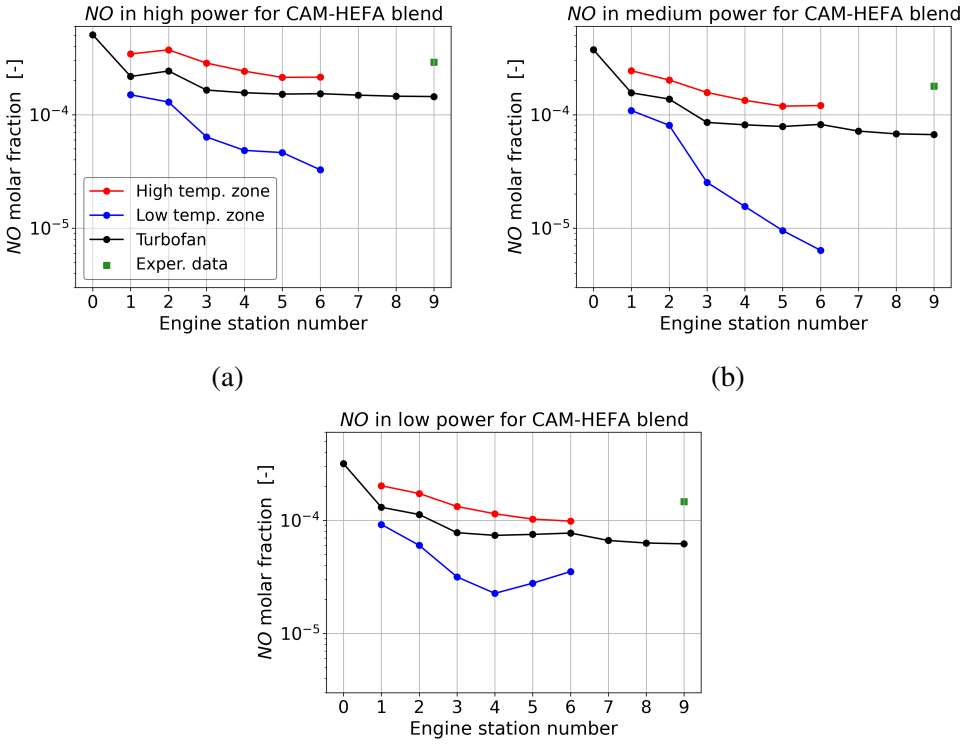

Figure 34: NO concentration profile in ACCESS conditions for decreasing throttle

As in APEX operating conditions, the value of EI_{SVF} is found to be overestimated by about 2 orders of magnitude regardless of the power level (Fig. 35). However, the trend of EI_{SVF} scaled to the EI_{SVF} value at maximum throttle (Fig. 36a and Fig. 36b), appears to be in line with the experimental data which show, regardless of fuel type, a value of about 40% and 35% for medium and low throttle versus the model's values of 30% and 20%. The EI_{SVF} percentage reduction using CAM-HEFA + JP-8, compared to using JP-8 alone, is reasonably predicted by the model with values almost constant around 30% versus experimental data in the range from 52% to 44% (Fig. 36c).

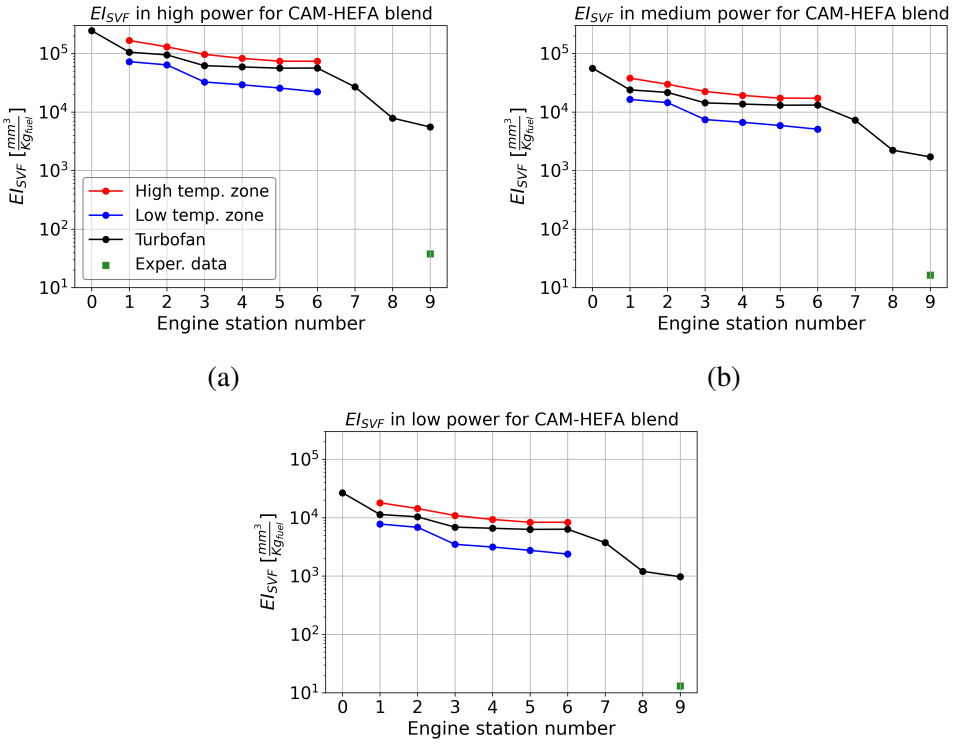

(a) (b)

(c)

Figure 35: EI_{SVF} profile in ACCESS conditions for decreasing throttle

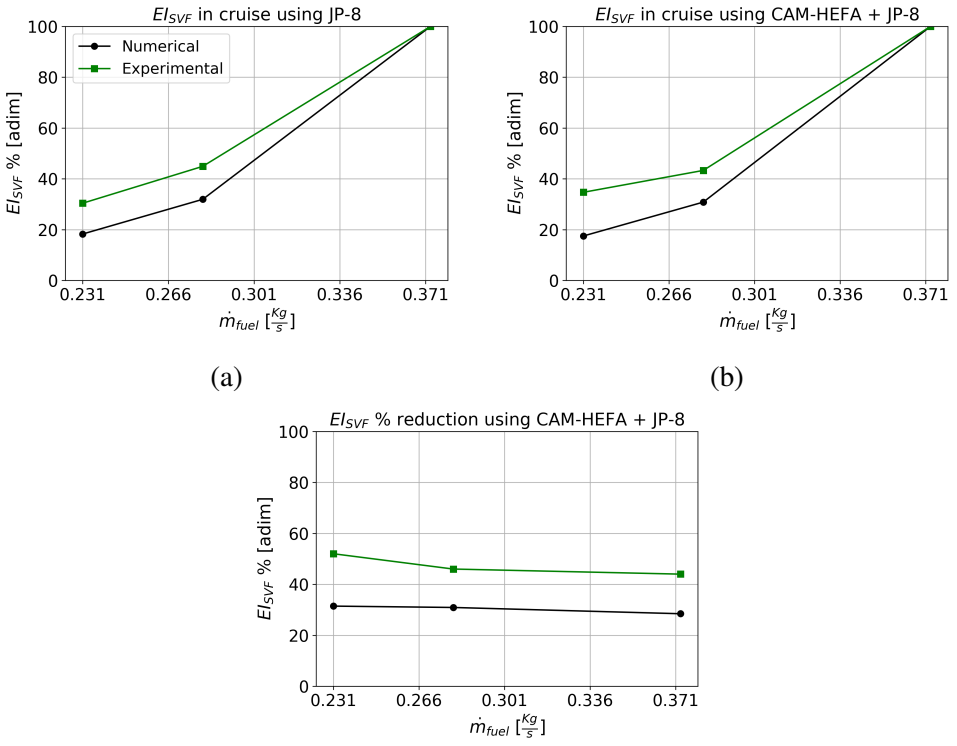

(a) (b)

(c)

Figure 36: EI_{SVF} reduction using CAM-HEFA + JP-8 and EI_{SVF} trends as throttle decreases

5.3 Conclusions

The present emission model provides good performance over a wide range of turbofan operating conditions for both conventional and CAM-HEFA fuel and is able to predict with fair accuracy the exhaust concentrations of 14 pollutant species among which CO, CO_2, NO, NO_2, N_2O and SO_2 represent those of greatest interest. The numerical results are overall close to experimental results for most flight conditions, with errors below two orders of magnitude for most relevant polluting gaseous species and soot volume emission index. The FGmech approach correctly models the kinetics of both JP-8 and CAM-HEFA + JP-8 blend providing a percent reduction value of EI_{SVF} reasonably close to the results obtained in full scale engine tests. The trend of EI_{SVF} at varying throttle has a good overlap with the experimental findings but absolute values are about 2 orders of magnitude larger. Overall, the model has comparable performance with the latest literature models but is validated over wider operating ranges and provides the ability to test even unconventional fuel compositions. Future improvements in the model may come from even more accurate modeling of the combustor PZ. This could be achieved through the use of CFD equipped with a simple combustion kinetics model that can faithfully replicate temperature, pressure and velocity field of the combustor, providing quantitative indications for network optimization. Given the growing interest in SAF and alternative fuels, FGMech application to model turbofan operations opens up the possibility of conducting, through numerical studies, more research on the influence of fuel composition on emissions generation.

6 CFD turbofan emission model

A better understanding of combustion processes in gas turbines is of primary importance for the reduction of pollutants and the engine energy efficiency.

Turbofan engines nowadays represent almost the totality of engines used in civil and military aviation industry. Historical data on passenger and air cargo traffic show that, with the exception of the COVID period 2020-2022, for the period between 2010 and 2019 the annual increase in the passenger per km and the freight-tonne per km have been about 6.6% and 3.8% respectively [80]. According to recent data [81], total air traffic passengers could grow in the next few years by an average $+7.3\%$ annually, with growth holding steady for the next 20 years. Under these premises, aviation-generated emissions, which currently make up 3% of the total anthropogenic emissions [82], could in the future constitute a substantial part of them. This possibility has led to the issuance of new targets and regulations by major supranational flight agencies, such as EASA and FAA, and by nation-states which have and continue to incentivize the transition to technologies with a lower environmental impact. Reducing the environmental impact of aviation can be accomplished primarily through the use of lighter materials (such as composite materials), increased aerodynamic efficiency (by acting on the shape of wings and fuselage), and the use of more efficient engines. While the first two have traditionally been the most widely used, engine efficiency, despite the progress that has been made, is probably the area in which there is most room for improvement because of the considerable complexity of the interplay between fluid-dynamic phenomena and chemical kinetics, which have so far hindered its full development.

Reducing the environmental impact of turbofans involves building models, which make it possible to assess the impact of component geometry, operating conditions, and fuel composition on the production of gaseous pollutants and soot. Nowadays, the construction of such models is more achievable due to the presence of high computational capabilities, the development of small combustion kinetic mechanisms, and an established literature on turbulence and turbulence-chemistry interaction models. Several attempts have been made in recent years to model the emissions generated from stationary and aircraft gas turbines. Most of these involve the use of computational fluid dynamics (CFD) techniques which can guide the construction of an equivalent network of 0D or 1D reactors. In fact, the use of complex detailed kinetic mechanisms, composed by at least hundreds of chemical species and thousands of reactions, applied directly to CFD is not computationally feasible, due to the very large number of equations for individual species which would have to be resolved in space (i.e., at each node of the mesh) and, in the case of transient simulations, for each time instant.

Over the past 20 years multiple models have been proposed and most of them have been designed for NO and CO estimation in can or annular combustors. In such models, the equivalent RN can consists of a variable number of reactors from a dozen up to more than a thousand. In some of these works, the RN is constructed algorithmically from the data obtained from CFDs [83] [84], while in others the CFD data is used as a guide to divide arbitrarily the domain into a number of different functionally zones, such as the flame front, dome and central recirculation zone [85]. In almost all cases, the volume is divided into homogeneous temperature and mixture fraction zones. Significantly interesing is the work of Akerblom and Fureby [86] where a CFD simulation, performed using Large Eddy Simulation (LES) method, is used to construct an equivalent RN of an aeronautical can combustor: this technique although much more computational expensive than RANS predicts accurately the concentrations of CO and NO, and the Sauter mean diameter of the fuel droplets.

In this thesis we present a model for estimating emissions of a wide range of gaseous pollutants for a CFM56-2 turbofan engine. This model consists of a reactor network composed of perfectly stirred (PSR) and plug flow (PFR) reactors. The reactor network is constructed from the temperature and velocity fields obtained through CFD Reynolds-averaged Navier–Stokes (RANS) simulations of the real components. Specifically, the CAD geometry of the CFM56-2 combustor was re-constructed from data in the work of Oliveira [57] while the turbines and nozzles, modeled as simple convergents or divergents, are represented in the reactor network by PFRs. In the absence of detailed information on CFM56-2 swirler geometry, the fuel entering the combustor is modeled with a set of droplets having diameters distributed according to a gaussian curve. The overall model was validated over a wide range of throttle levels in static operating condition, and on two types of fuels. The type of fuel used is JP-8, a conventional military aviation kerosene blend. The datapoints used to validate the model are contained in NASA's APEX reports [59]. The construction of the mechanism is done through the FGMech approach [45] [46]. The FGMech approach is used to generate lumped, high-temperature, oxidative pyrolysis sub-mechanisms for each of the investigated fuels. According to this approach, the real-fuel is represented as a single surrogate species that matches the average molecular weight and atomic distribution of the blend. Subsequently, seven reactions are defined to describe the high temperature decomposition of the surrogate species into smaller species. This methodology makes it possible to assess how the composition of the fuel blend affects the emissions and performance of the engine in different flight phases. Another major advantage of FGMech is that, unlike detailed mechanisms such as [87], the resulting overall combustion mechanism is still enough small in size (236 species and 1430 reactions in total, when USC-II is used as base mechanism) to allow simulations to be performed even with reduced computational capabilities.

6.1 Methods

Section 6.1.1 first illustrates the methodogy and operations used to reconstruct the CAD geometry of the CFM56-2 combustor. Section 6.1.2 presents the setup and type of boundary conditions to perform the CFD combustor simulation. Section 6.1.3 illustrates a brief literature study of the swirler and collects all available information to provide an estimate of the average droplet diameter and velocity field near the swirler. Sections 6.1.4 presents the surrogated fuel blend compositions used while Section 6.1.5 briefly describes the construction of the combustion kinetic mechanisms. Section 6.1.6 presents the criteria to generate the equivalent reactor network from CFD simulation data. Finally, Section 6.1.7 describes how to construct a CFM56-2 performance model using the GSP12 software while Section 6.1.8 shows the datapoints of the APEX dataset used for model validation.

6.1.1 CFM56-2 combustor geometry

Proper fluid-dynamic modeling of the combustor is of paramount importance for emission estimation due to the high temperatures that characterize this component.

The temperature inside the combustor can reach more than $2500K$ at the PZ and decrease to about $1300K$ at the outlet section. Differently, modeling of components such as the HP-LP turbines and nozzle, can, in principle, be done less detailed because of the relative low temperatures and neglegible presence of unburned fuel. This work uses a detailed CFM56-3 combustor CAD geometry: this was assumed to be a good approximation of CFM56-2

burner. The geometry was derived starting from images of the combustor section found in Oliveira's work [57]. This combustor section was imported as a .png image within Ansys SpaceClaim [88] and the outer perimeter was subsequently approximated through the use of multiple splines. The section was scaled by a factor to ensure a total combustor length of about $19cm$ [53]. The resulting section was then subjected to a circular extrusion of $0.237m$ radius (defined from the centerline of the swirler) and 360 degrees angle. Additional details at the outer and inner liners such as SZ, DZ and cooling holes were added to the resulting CAD model. Specifically, the diameters (Table 29) and relative positions (Figure 37) of the above-mentioned holes were deduced from the relative images of the CFM56-2 combustor found in [57].

Table 29: Swirler outlet geometry and SZ/DZ/cooling holes diameter

Diameter $[mm]$	PZ_1	PZ_2	PZ_3	SZ	DZ	$Cool.$
dome	11.0	11.92	18.73	-	-	-
outer liner	-	-	-	10.00	7.05	1.60-2.00
inner liner	-	-	-	10.24	7.00	1.40-1.60

The fuel injector and swirler are not directly modeled but rather the outflow conditions are selected based on considerations over very similar swirler (as described in Section 6.1.3).

The combustor domain was divided into 4 volumes (Figure 37) to have more flexibility in realizing the mesh. A finer mesh was chosen in the PZ near swirler outlet (Volume 1 in Figure 37) in to achieve greater accuracy of the solutions. The remaining volumes were meshed more coarsely with elements about twice the dimension of the PZ elements. All the meshes were conformal. The total number of elements obtained is 3604180 with a maximum element skewness of 0.86858.

6.1.2 CFD boundary condition and setup

The boundary conditions chosen for the CFD simulation are listed shown in Figure 37 and listed in Table 30.

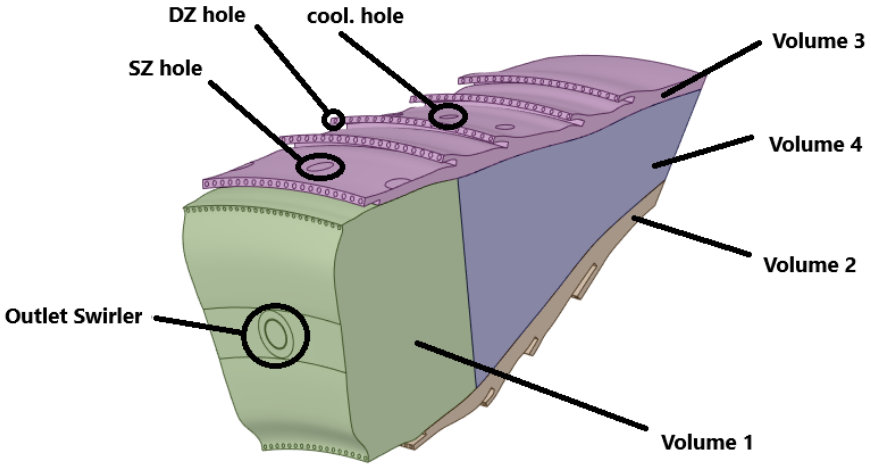

Figure 37: CFM56-2 combustor representative section and its main features

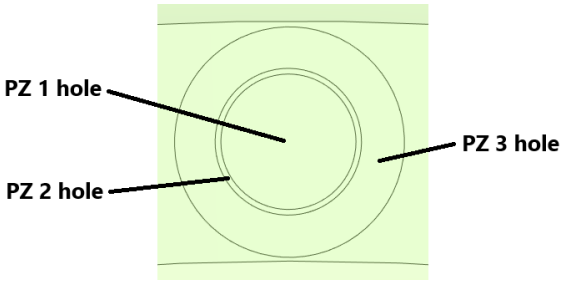

Figure 38: Details of the swirler outlet

Table 30: Burner boundary conditions

ID zone	Zone name	Boundary type	$\dot{m}$ % (of total mass) [adim]
1	PZ 1 hole	mass flow inlet	13%
2	PZ 2 hole	mass flow inlet	1%
3	PZ 3 hole	mass flow inlet	13%
4	SZ holes	mass flow inlet	20%
5	DZ holes	mass flow inlet	17%
6	cooling holes	mass flow inlet	36%
7	exhaust section	pressure outlet	-
8	sector sides	symmetry	-

The RANS CFD simulation is performed using Ansys Fluent software. The sections corresponding to the PZ, SZ, DZ and cooling holes were defined as mass flow inlets. The mass flow rates at the inlets were defined by considering that 26% of the flow rate from the HP compressor outlet passes through the swirler while the remaining part is distributed in proportion to the area of the SZ, DZ and cooling holes as done for the previously constructed emission model (Table 30). Tests performed by slightly changing the distribution of non-PZ flow rates showed such variation does not appreciably affect the results of gas species concentrations at the combustor outlet.

For all inlets except PZ and cooling inlets, it was chosen to tilt the inlet flow by an angle of 60 degrees with respect to the centerline of the swirler (Figure 39): this allows us to qualitatively simulate the effect of the momentum that the flow has along the axial direction of the engine just before entering the combustion chamber.

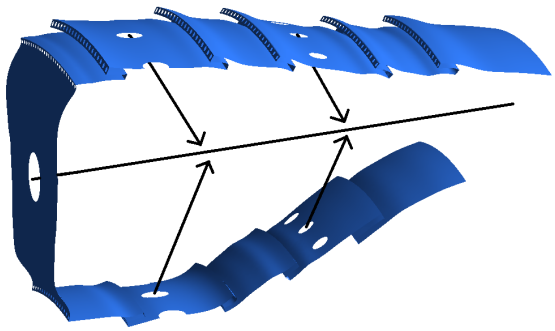

Figure 39: Inflow slope of SZ and DZ inflows

All flows entering the combustor were assigned temperature and pressure values as indicated in Section 6.1.8, according to experimental data. In the present CFD simulation,

the energy balance is included and the Realizable k-ε is used as the viscous model. The Realizable k-ε model was chosen because in experimental studies of non-premixed combustion it exhibited superior performance compared with the other turbulence models [89]. The chemistry model considered is the Species Transport while the Discrete Ordinates is selected as the radiation model. Droplet dynamics is modeled through the Discrete Phase Model (DPM); more details on the distribution and properties of droplets are provided in Section 6.1.3. The pressure-velocity coupling scheme considered is Coupled and for all variables (velocity, density, energy, species, etc.) the spatial discretization approximation is performed using Third-order MUSC: this choice allows for greater accuracy in estimating the solution in spite of greater computational effort and possible instabilities in the solution (the latter not occurring in the simulations conducted) [90]. Tests have shown that the use of a First-order discretization provides an appreciably different solution from that provided by Second-order or Third-order: differently the latter two provide very similar values for the pressure, temperature, velocity and equivalence ratio fields. The CFD model convergence criteria are listed in Table 31.

Table 31: CFD convergence criteria

Criteria numb.	Variable	Domain	Condition
1	equations residuals	volume	$<< 10^{-3}$
2	mass flow imbalance	inlet/outlet	$<< \dot{m}_{tot}$
3	mass weighted-average T	volume	stability
4	mass weighted-average ϕ	volume	stability
5	mass weighted-average T	outlet	stability
6	mass weighted-average P	outlet	stability
7	maximum ϕ	volume	stability
8	maximum T	volume	stability

6.1.3 Swirler modeling

In the absence of detailed knowledge of the CFM56-2 swirler geometry, the swirler was modeled in the CFD simulation by imposing the outflow conditions.

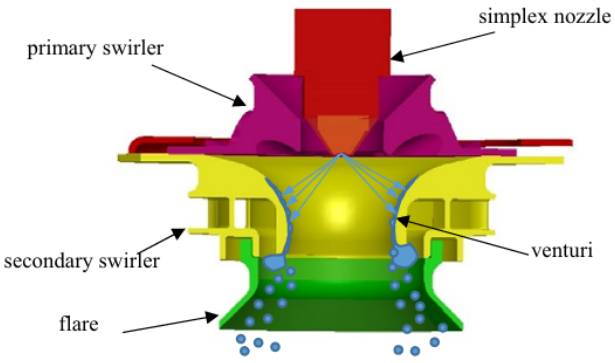

Figure 40: Schematic representation of a swirler section [91]

Figure 40 shows the main components of a swirler, also known as prefilming airblast atomizer.

The liquid fuel is injected through an simplex or duplex atomizer generally using a conical pattern: the fuel then impinges on the walls of the primary ventury, forming a thin film on

the order of $50-200\mu m$ thick at the end of ventury throat [91]. The formation of a thin film is also promoted by the swirling airflow from the primary swirler inlets, which also forces the motion of the film toward the primary ventury tip. At the primary venturi tip the film is broken into droplets of different diameters due to the action at the tangential stress generated by the presence of an additional swirling airflow passing through the secondary swirler and counter-rotating (in most cases) with respect to the primary swirler airflow. The generated droplets pass through the flare and reach the combustor PZ where due to a higher than boiling room temperature they will progressively evaporate releasing gaseous fuel into the environment [92]. Flare geometry can appreciably influences swirler operation and particularly axial, radial, and tangential velocity profiles, and droplet distribution in the immediate proximity of the flare outflow section [93].

In the scientific literature, there are currently several empirical and semi-empirical formulas for estimating the Sauter mean diameter (SMD) of a spray generated by prefilming airblast atomizers such as Rizkalla-Lefebvre [94], Gepperth [95], Hsiang-Faeth [96]. However, most of these models are validated in a fairly narrow range of conditions and are generally calibrated over relatively low ranges of mass flow rate, temperature, and pressure (i.e., no more than $500K$ and $8atm$) compared to the conditions of the present work.

The atomization process of an airblast swirler is almost independent on ambient pressure and benefits very little from AFR values above 5.0 [97]. Studies conducted on prefilm swirlers have shown that the SMD undergoes a strong reduction for AFR values between 1 and 3 [98]. For values above 3 the swirler size tends to stabilize at fixed SMD values: this tendency is most pronounced at high airflow swirler velocities, with SMD values that can reach $20\mu m$. From the above we can infer that when operating at high AFRs (above 10) the most relevant factor affecting atomization process is the airflow velocity.

Experimental data on CFM56-2 swirler currently in the literature are very limited. The few available data on the CFM56 swirler refer to experimental campaigns conducted on X3-scale models under non-reactive conditions [93]. Such test shows clearly that the influence of the spray angle on the continous phase flow field is neglegible [99]. Further tests conducted for low air flow rates also showed that the average droplet diameter is around $35\mu m$ with values decreasing towards the swirler centerline [100]. The droplet rate profiles also show peaks approximately around the fuel film breakup locations [100] with much lower values in the central part of the swirler. Fixed point measurements near the swirler have also shown that the droplet diameter exhibits much less variability over time than continuous phase characteristics such as axial velocity [101].

Since accurate information on the geometry of the CFM56-2 swirler is not available, it was decided, based on qualitative considerations described above, to model the swirler outflow by imposing boundary conditions on the velocity vector direction and the droplet distribution. The outflow direction is indicated in Table 32 in cylindrical coordinates.

Table 32: Flow direction imposed at the swirler outlet

Inlet ID	Radial component	Tangential component	Axial component
PZ 1	8	6	10
PZ 2	8	-6	10
PZ 3	8	-6	10

The cylindrical reference system is chosen such that the axial axis is normal to the swirler outlet (and directed toward the internal combustor volume) with the remaining two axes lying

in the outlet plane. As in the CFM56 [93], the PZ-1 and the PZ-2/PZ-3 flows were imposed as counter-swilring. Droplets generated by the swirler are assumed to have symmetric diameter distribution around an average value of $35\mu m$ (Table 33); droplets are generated only at the PZ-3 surface, which emulates the presence of an annular section source adjacent to the primary venturi leap where the breakup of the fuel liquid film occurs. The presence of primary droplets generated directly from the injectors, which are mostly present more in the central part of the venturi, is neglected here as they are of secondary importance.

Table 33: Droplet diameters distibution

Parcel number	1	2	3	4	5	6	7
Diameter [μm]	5	15	25	35	45	55	65
Fraction number [%]	7	11	15	34	15	11	7

The choice of the average diameter and shape of the PZ-3 section was suggested by [100], in which a scaled CFM56 swirler is tested at low power (non-reactive) conditions: the obtained experimental data shows an average diameter of about $35\mu m$ and droplet accumulation along the shearing layer between the primary and secondary streams.

6.1.4 JP-8 surrogate model

The kinetic mechanism for combustion is constructed through the use of the FGmech approach [45] [46]. This methodology requires the knowledge of the fuel composition to determine the stoichiometric coefficients and kinetic parameters of the lumped mechanism for the fuel oxidation.

In the present work, POSF10264 [62] is used as a JP-8 surrogate.

6.1.5 Overall kinetic mechanism

The gas-phase kinetic mechanism is obtained by combining the FGMech and a base mechanism with a PAH mechanism [71] and additional chemistries for NO_x [50] and SO_x [51]. The USC-II [102] is used as base combustion mechanism.

6.1.6 Reactor Network generation criteria

The CFD solution is used as a guide to divide the fluid dynamic domain into zones characterized by homogeneous flow properties. The division of the domain is performed using filtering variables through a set of iso-surface values. The filtering variables could be, in principle, any physical quantity provided by the CFD.

The filtering variables used in the present model are temperature (T) and velocity magnitude (v). Temperature was selected because it is a crucial factor in determining the reaction rates (according to the Arrethius law) and thus the final concentration. The velocity significantly influences the residence time which in turn affects not only the temperature at the end of combustion but also the percentage of polluting agent (such CO_x and NO_x). The filtering variables are applied sequentially, i.e., first the T filter and then the v filter (Figure 41): thus, the first step is to obtain a fluid dynamic domain divided into subdomains by temperature ranges (Table 34). Both T and v ranges in Table 34 are given as percentage relative to their minimum and maximum values in the combustor.

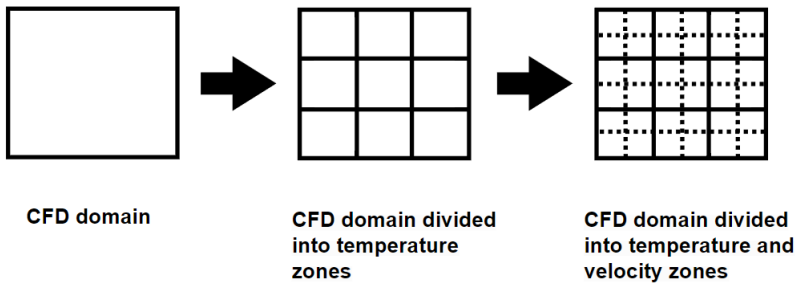

Figure 41: Filtering operations are applied sequentially on the entire domain

Table 34: Temperature and velocity intervals used for filtering operations, given as percentage relative to their minimum and maximum values in the combustor

Variable	
$T\ [K]$	0%, 5%, 10%, ... , 90%, 95%, 100%
$v\ [\frac{m}{s}]$	0%, 10%, 20%, ... , 80%, 90%, 100%

Each of these subdomains is assigned a single value of T obtained by mass-weigth averages of the individual cells (of the CFD) composing it. These subdomains are in turn subdivided into subdomains using v ranges (Table 34), and each subdomain is assigned a single v value obtained by mass-weigth averages of the individual cells (of the CFD) that comprise it. In principle, the higher the number of T and v intervals the better the reactor network will approximate the operation of the CFD model but at the expense of increased computational resources (especially in terms of RAM and CPU time). The individual subdomains thus obtained are represented by means of perfectly stirred reactors (PSRs) that are assigned volume values equal to the sum of the volume of their constituent cells and values. The connectivity of the network is reconstructed from the mass flows between the cells adjacent to the boundaries bordering the sub-subdomains themselves. The formulation of the PSR reactors includes the energy balance equation and the individual PSR volume cannot be less than 0.04% of the total volume: this criterion is chosen to avoid obtaining too complex RN which contains zones that, due to their small volume, have little influence on the overall combustion dynamics. A inlet fuel flow is also defined for each PSR and the mass flow rate is equals the sum of the flow rate given by the evaporation of the individual droplets contained in the volume. Flows near the combustor outlet are routed to a mixed located at the outlet: thus the equivalent RN presents a single flow as output. The burner outflow is provided as input to a block of 3 PSRs arranged in series, which represent the HP turbine, LP turbine, and nozzle (Figure 42).

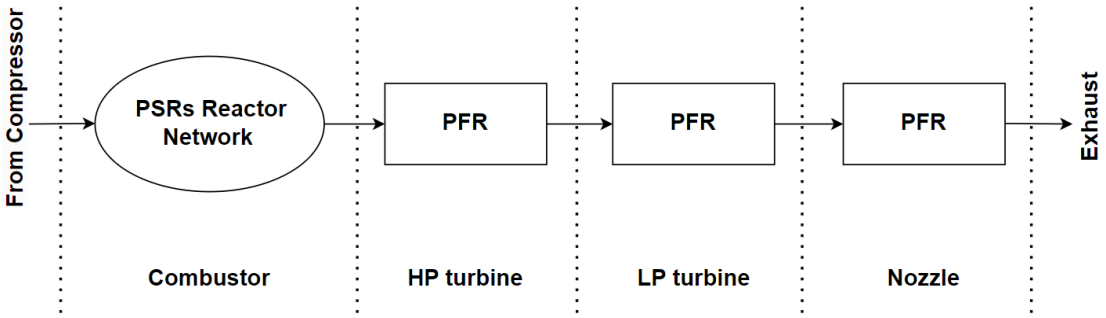

Figure 42: Turbofan scheme

The pressure values and dimensions of the PSRs are given in Section 6.1.7 and Section 6.1.8. Domain partitioning, filter application and creation of the equivalent reactor network is performed through Ansys Energico software.

In order to achieve stable and convergent solutions for the RN, it was necessary to use Relaxation as the Tear Acceleration Algorithm and to increase the absolute and relative tear tolerances by 3 orders of magnitude (compared to the default values). The complete settings for Tear Stream Control are given in Appendix (Table 59).

6.1.7 CFM56-2 engine performance model

To generate some of the reactor network inputs, it is necessary to obtain the off-design performance of the CFM56-2 turbofan using GSP12 software. GSP12 is a software used for simulating stationary and transient performance of a wide variety of gas turbine configurations, with components represented by nonlinear equations or maps. The results provided by GSP12 are close to those provided by other commercial software such as GasTurb [22] or Matlab implementable algorithms [73].

To obtain the off-design-performance, a dual-spool turbofan model was initially created in GSP12, and then supplied with the CFM56-2 design parameters found in [59] (summarized in Table 35) and the Mach numbers of the flow at each engine station (Table 36).

Table 35: CFM56-2 design parameters

$F\ [KN]$	$OPR\ [adim]$	$\pi_f\ [adim]$	$\pi_{LPcompr}\ [adim]$	$\pi_{HPcompr}\ [adim]$	$\alpha\ [adim]$
98.0	23.5	1.61	2.84	11.43	6.0

Table 36: Mach at the component inlet and isoentropic efficiencies (on design condition)

Type	Fan	Compressor	Burner	HP turbine	LP turbine	Byp./core nozzle
Ma	0.40	0.40	0.40	0.35	0.35	0.40
η	0.85	0.85	-	0.90	0.90	-

The GSP turbofan model requires defining the isoentropic efficiencies of the fan, LP compressor, HP compressor, HP turbine, and LP turbine. These values were derived from the typical values of older turbofan generations and are reported in Table 36. The design condition coincides with the static operating conditions of $Ma_0 = 0$, $z = 0m$, and $f = 0.0188$. The value of f was calculated to obtain the amount of F in Table 35. GSP12 also provide

as output the inlet/outlet area of turbofan components: these values (see Table 57 in the Appendix) were used as initial guess and then slightly modified so that the present model would give approximately the Mach values on the input and output sections of the components shown in Table 36. The values of the sections used are shown in Table 37.

Table 37: Turbofan model sections area

A_{tHP} inlet $[cm^2]$	A_{tLP} inlet $[cm^2]$	A_e inlet $[cm^2]$	A_e outlet $[cm^2]$
400	900	2300	1400

6.1.8 APEX and ACCESS datapoints

The accuracy of this emission model was evaluated by comparing the results obtained with experimental measurements derived from the NASA APEX [59] database.

APEX database contains, for each engine operating point, the concentrations more than 20 pollutant species at the outlet nozzle. The measurements were carried out on different diametrical points: these values show a substantial homeogeneity of species concentration over the whole outlet section and therefore for simplicity in the present work we will refer only to the concentration at the nozzle axis. Table 38 shows the datapoints used to validate the model along with the respective engine operating conditions.

Table 38: Nomenclature for APEX test conditions

Flight condition	Ma_0 $[adim]$	z $[m]$	Power [%]	Dataset ID	Fuel type
7% APEX	0	0	7%	807*	JP-8
30% APEX	0	0	30%	813*	JP-8
100% APEX	0	0	100%	816*	JP-8

*Note: number identifying the dataset point in [59]

Pressure values imposed at the inlet and outlet section of the HP turbine, LP turbine, and nozzle are calculated using average mach values shown in Table 36 and pressure ratios in Table 58 (derived starting from the CFM56-2 performance model). Pressure ratio values are slightly modified in order to ensure adapted core nozzle conditions. Changes in pressure ratios, however, has no appreciable influence on species concentrations at the engine outlet.

6.2 Results

In Section 6.2.1, the independence study of CFD results from mesh size is performed. Section 6.2.2 illustrates the temperature and velocity CFD fields while Section 6.2.3 briefly lists the RN dimensions obtained for each APEX datapoint tested. Section 6.2.4 reports the concentration profiles of different gas species as function of fuel mass flow rates for the conditions given in Table 38.

6.2.1 Mesh independency study

The accuracy of a CFD model in modeling a real component depends on a number of factors. These factors can be distinguished into: the convergence of the solution, independence of the results from the mesh size, and the simulation setup.

Solution convergence depends largely on the size and type of mesh used, and the numerical method employed. Convergence is considered achieved when the conditions described in Table 31 are all simultaneously satisfied. Verification of the independence of the results from the mesh size is achieved by running CFD simulations in 100% APEX condition with increasingly finer meshes (Table 39) and verifying that as the mesh size decreases, the quantities of interest tend to a stable value. The monitored quantities are listed in Table 40. The simulation setup is more concerned with the models used to describe the physics of the problem and the imposed boundary conditions. The correctness of the setup cannot be deduced from considerations on the stability of the obtained solution but can be ensured by choosing the best type of boundary condition on the basis of experimental measurements made on the physical component or from any literature available. Results obtained show the convergence of the solution (Table 40) and its independence of mesh size (Table 39).

Table 39: Size and quality of the tested meshes in APEX 100%

Mesh ID	Number nodes	Number cells	Max skewness
Mesh 1	252895	945221	0.94021
Mesh 2	389739	1480501	0.93943
Mesh 3	807333	3604180	0.86858

Table 40: Target quantities for different mesh size

Variable	Domain	Mesh 1	Mesh 2	Mesh 3
mass weighted-average fuel fract. $[-]$	outlet	$10.25 \cdot 10^{-8}$	$9.25 \cdot 10^{-8}$	$6.74 \cdot 10^{-8}$
mass weighted-average T $[K]$	outlet	1442.0	1441.5	1440.5
maximum T $[K]$	volume	2820.1	2822.8	2839.3

6.2.2 CFD results

The temperature field for the APEX 100% condition (Figure 43) shows high values in the PZ (i.e., in the immediate vicinity of the swirler) with peaks around 2800K, then decreasing and assuming a more homogeneous distribution proceeding toward the outlet, due to the presence of the dilution holes. The presence of the cooling holes makes it possible to maintain the outer and inner liners temperature in the 900K-1200K range, compatible with the mechanical properties of the materials used.

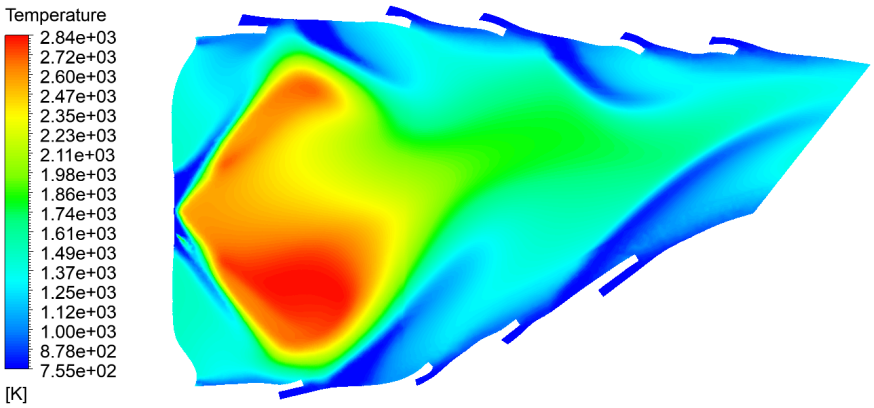

Figure 43: Temperature field in 100% APEX condition

The velocity field (Figure 44) is highly inhomogeneous, with the highest velocities occurring in the areas adjacent to the swirler outlet and SZ/DZ holes. In contrast, the central part of the PZ exhibits moderate velocities thus ensuring flame and combustion stability.

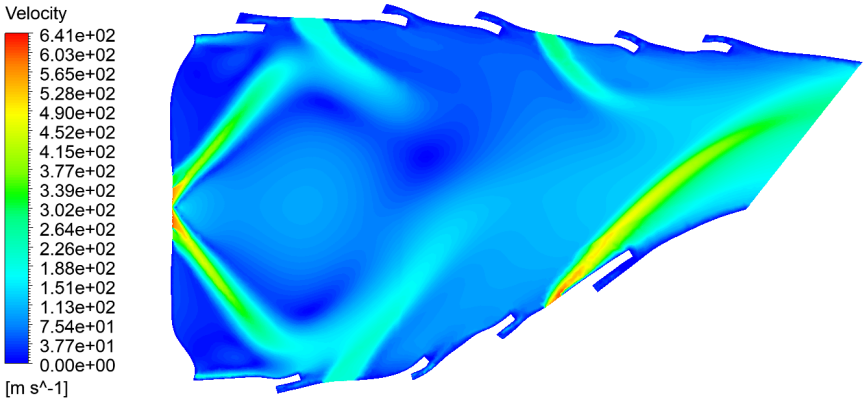

Figure 44: Velocity field in 100% APEX condition

Figure 45 show the fuel mass flow provided by the evaporation of droplets. The evaporation of the droplets is very pronounced a few mm away from the swirler outlet and from there it tends to decrease to reach almost zero values at a distance of about $3cm$. A detail that, because of the scale, cannot be noticed in Figure 45 is that some droplets reach the vicinity of the outlet burner leading to an albeit very reduced release of gaseous fuel in the secondary combustion and dilution zones.

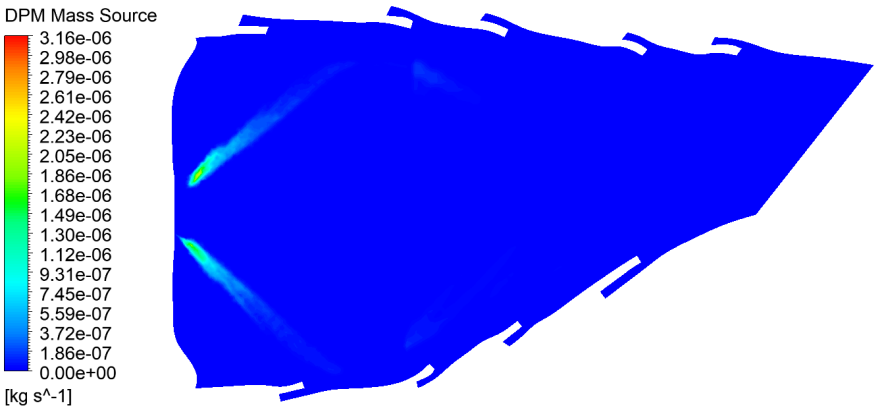

Figure 45: DPM field in 100% APEX condition

6.2.3 Reactor Network layout

The reactor network obtained by application of filter variables depends on the operating condition simulated: although the applied filters are the same (Table 34), the presence of different fields for all the variables leads to a different volume partitioning and thus a different RN architecture. For each condition tested the total number of reactors is shown in Table 41.

Table 41: Number of reactors

7% APEX	30% APEX	100% APEX
233	209	211

6.2.4 APEX results

In this Section, the engine outlet concentration values of a wide multitude of gas species are compared with experimental data from APEX datapoints (Table 38).

The carbon monoxide (CO) concentration is found to be overestimated by 0.5 to 1.5 orders of magnitude, depending on engine operating conditions, with the simulated trend, as a function the fuel mass flow rate, showing a good matching with the experimental one (Figure 46). The concentrations of carbon dioxide (CO_2) and oxygen (O_2) are accurately predicted by the model (Figure 47 and 79). The concentrations of methane (CH_4) and acetylene (C_2H_2) are almost consistently overestimated by 1 and 2 orders of magnitude, respectively, and their simulated and experimental trends are in perfect agreement (Figure 48 and 52). The concentrations of nitric oxide (NO) and nitric dioxide (NO_2) are predicted with a margin of error of 0.5 orders of magnitude (Figure 49 and 50): the experimental and numerical trends are overlapping, except for NO_2 at low fuel flow conditions. The concentration of nitrous oxide (N_2O) is consistently underestimated by about 1 to less than 0.5 orders of magnitude (Figure 51): the experimental trend is flatter than the simulated one, with the latter increasing by about 1 order of magnitude from low to high power conditions. The concentration of butadiene (C_4H_6) is predicted with a margin of error of maximum 0.5 magnitude orders (Figure 75); similarly, the concentration of methanol (CH_3OH) is overestimated by less than 1 order of magnitude with more accurate model performance for high fuel mass flow rates (Figure 78). The ethylene (C_2H_4) concentrations is overestimated by about 1 to 1.5 orders of magnitude but the simulated trend closely reproduces the experimental trend (Figure 74). The model gives significantly underestimated concentrations for propane (C_3H_8) compared with all the other species tested (Figure 77): values differ by about 1.5 to 3.5 orders of magnitude but the experimental and simulated trends are similar, except for low powers. The model gives for ethane (C_2H_6) a decreasing trend as fuel mass flow increases versus a slightly increasing experimental trend, and the estimation error is within 1 order of magnitude (Figure 76)

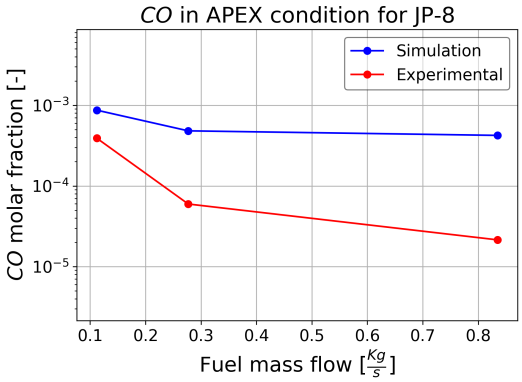

Figure 46: CO concentration in APEX

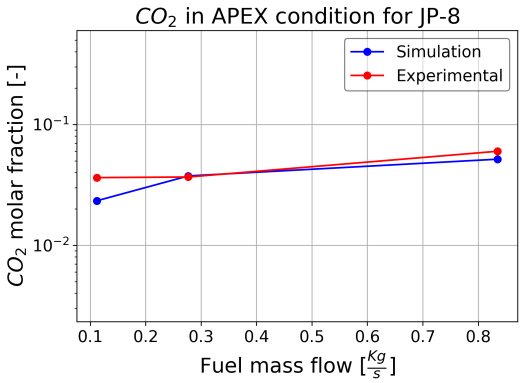

Figure 47: CO_2 concentration in APEX conditions

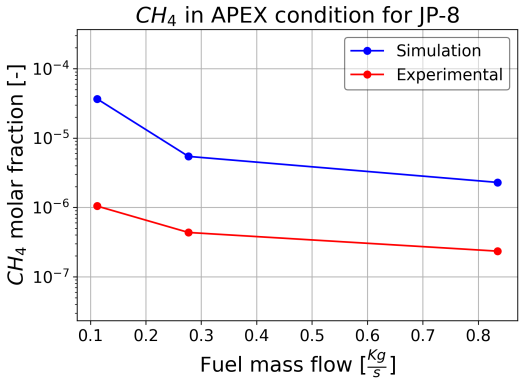

Figure 48: CH_4 concentration in APEX conditions

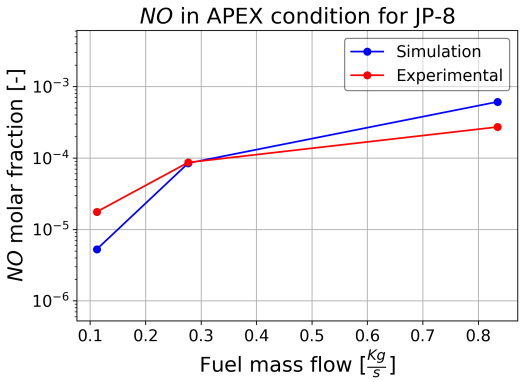

Figure 49: NO concentration in APEX conditions

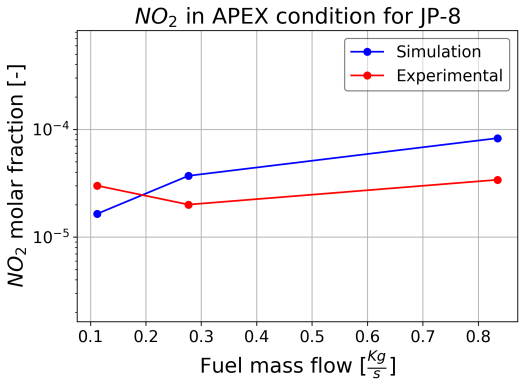

Figure 50: NO_2 concentration in APEX conditions

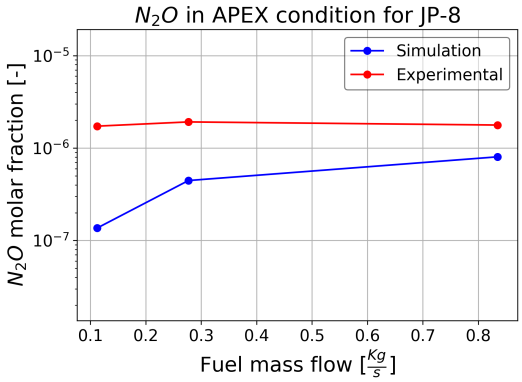

Figure 51: N_2O concentration in APEX conditions

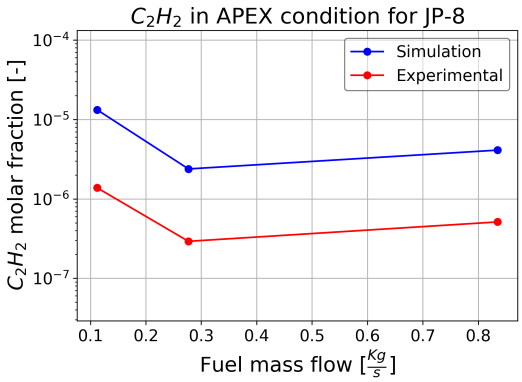

Figure 52: C_2H_2 concentration in APEX conditions

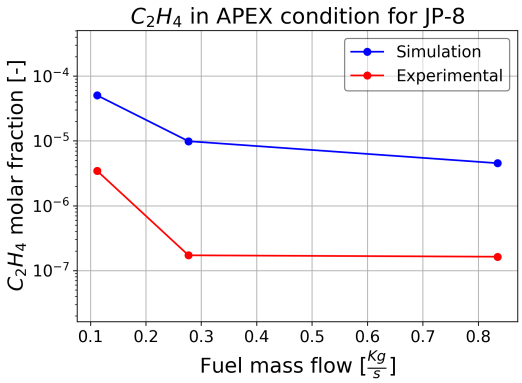

Figure 53: C_2H_4 concentration in APEX conditions

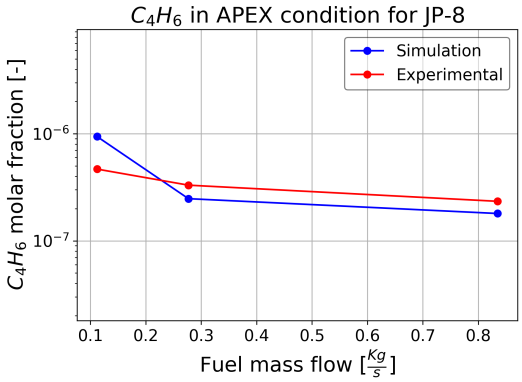

Figure 54: C_4H_6 concentration in APEX conditions

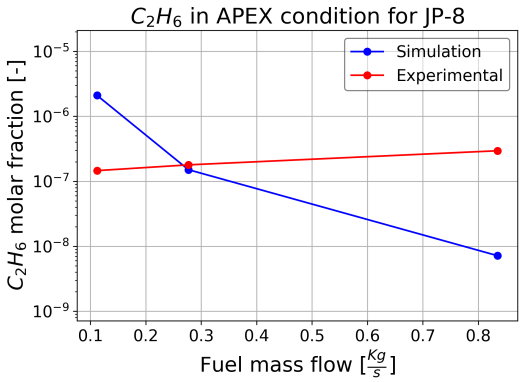

Figure 55: C_2H_6 concentration in APEX conditions

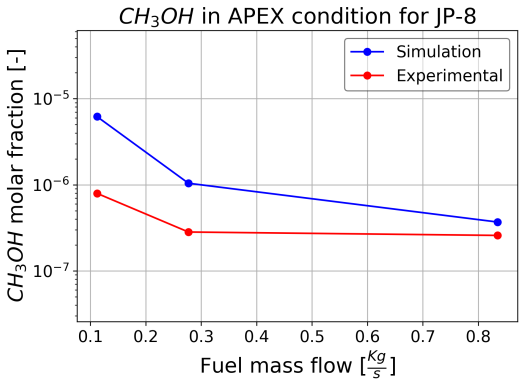

Figure 56: CH_3OH concentration in APEX conditions

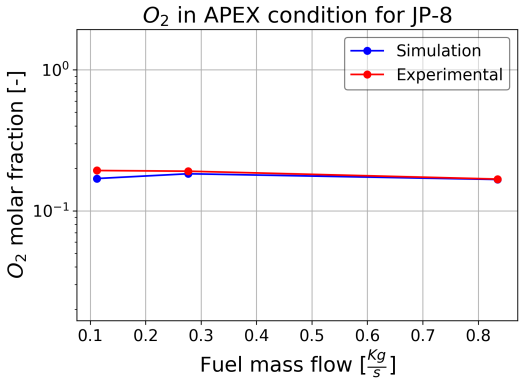

Figure 57: O_2 concentration in APEX conditions

6.3 Conclusions

In this thesis, a method for constructing an turbofan emission model from CFD data is proposed. The combustor volume is partitioned according to temperature and velocity homogeneity criteria thus allowing to obtain an equivalent network of PSR reactors. This network is connected in series to 3 PFR reactors representing the HP turbine, LP turbine, and nozzle. The model was validated on JP8 fuel blend using experimental data obtained from ground tests at different power levels (APEX database). Overall, the model predictive performance are satisfactory, with errors in estimating concentrations of most pollutant species not exceeding 2 orders of magnitude. These differences in concentrations with experimental data can be caused, at least in part, by an intrinsic difficulty in experimental measurements, due to the low concentrations of the pollutant species in the exhaust gasses.

7 $DeNO_x$ design for turbofan

NO_x are pollutants produced by combustion which play a relevant role in enhancing the greenhouse effect [103], worsening health conditions of humans and ecosystems. The scope of this thesis is to investigate the use of catalysts for the NO_x abatement of LP turbine outflow gasses in separated flow turbofan engines. This technology is nowadays massively used in automotive and stationary applications with excellent results in terms of NO_x conversion efficiency ($DeNO_x$): its use in aeronautical applications, however, has not been pursued until now due to various factors including high mass flow rates and LP turbine exit gas temperatures characterizing the turbofan core as well as the excessive weight and bulk that this technology would entail, in a sector where weight is a critical factor in performance. A further but no less important problem arises from the fouling catalyst phenomenon [104], consisting in the partial obstruction of the holes, which would inevitably affect the reliability and performance of the overall engine. At present, one of the methods to limit NO_x emissions is to optimize the combustor design in order to reduce the formation of excessively hot gas pockets and ensure a more uniform temperature distribution. These measures, however, lead to an increase in the production of CO_2/CO and unburned hydrocarbons so it is necessary to find a trade off between NO_x and CO_2/CO production [105]. A preliminary study for the use of catalysts in turbofans was carried out in [106], in which the authors through the use of semi-empirical formulas come to the conclusion that an adequate ammonia-based flue gas treatment system must use a monolithic catalyst with a cross-sectional area of around $19m^2$ and a thickness of a few mm: for this reason they highlight the need for an innovative catalyst design with a more compact shape. In the literature there are several articles on CFD numerical simulation of a diesel engine SCR catalyst under non-uniform flow conditions [107], which in some cases also propose an SCR system setup including sensors, storage system and urea flow regulation [108]: these works, carried out for marine and automotive applications, show low GHSV and excellent $DeNOx$ efficiency ($\approx 80-90\%$) for design working condition. The present thesis proposes a new catalyst design, which is developed and simulated in Ansys Fluent and interact with a 0D nonlinear turbofan model in order to estimate turbofan overall performance such as F and $\dot{m}_{fuel}$. The obtained performance are compared with that of a conventional turbofan, with the same design parameters, in order to quantify the impact of this technology. Catalyst geometry is modeled in Ansys DesignModeler, meshed and subsequently integrated with a NO_x-NH_3 chemical kinetics model, representative of the most important chemical processes that take place. The role of the catalyst is to implement a chemical process known as selective catalytic reduction (SCR), with the aim to drastically reduce (up to $90\%-95\%$) the presence of NO_x, mainly NO and NO_2, in combustion gasses through the use of reducing reagents such as ammonia (NH_3) and urea. The reducing agent considered in the thesis is NH_3, which is assumed to be injected after the last stages of LP turbine. The high degree of turbulence in the turbine outflow allows NH_3 to be effectively mixed with the burnt gases, allowing a fairly homogeneous mixture to be obtained. All the injection and mixing dynamics mentioned above are not dealt with in this thesis, which limits itself to considering a perfectly homogeneous mixture of flue gas and NH_3 at catalyst inlet. The catalyst consists of Cu-ZSM5, which is a high-performance material, in terms of $DeNO_x$ and $NH_{3_{slip}}$, at high temperatures.

7.1 Methods

This Section first presents the kinetic mechanism adopted for SCR, the calculation of surface reaction per unit of catalyst volume, the catalyst surface site density estimate and the validation of the kinetic model in Ansys Fluent. Next, a new catalyst design with the potential to meet the high mass flow and velocity requirements that characterize the turbofan core flow is presented together with the related Ansys Fluent setup. The presence of the catalyst between the LP turbine and the core nozzle makes it necessary to build an ad hoc nozzle, with a different shape from the conical one. A model of a 0D turbofan equipped with a catalyst is introduced next and assumptions are made about the flow properties inside the catalyst. These assumptions allow the catalyst to be modeled as an adiabatic 0D component (duct) characterized by a variable pressure ratio value (π_{cat}). Lastly, in Section 7.1.9, the recurrent algorithm for turbofan performance and DeNOx estimation is illustrated. Such an algorithm needs as input the flight conditions (z, Ma_0, f) and design parameters and involves, starting from a guess value of π_{cat}, the simulation of the turbofan in GSP 12: the output values (P, T, and v at the various sections of the engine) will then be used to define the boundary conditions for the CFD simulation of the catalyst, which in turn will compute a value of π_{cat} that will again be provided as input to GSP 12. This loop stops once the value of π_{cat} has reached convergence (which happens acceptably in a few iterations) and the output data from GSP 12 will be used to provide boundary conditions for the nozzle simulation.

7.1.1 SCR reaction mechanism

The kinetic model for $DeNO_x$ on Cu-ZSM5 used in this work is derived from [109], which is very close to the one proposed in [110]. The kinetic model, consisting in 7 non-reversible reactions (1 in gas phase and 6 surface reactions) and 1 reversible reaction, is proposed in Tab. 42 together with their rate expressions. The rate expression takes the form of Arrhenius law, which is suitably modified in order to introduce the typical dependence of surface reactions on θ_{NH_3} in addition to C_i (molar concentration of species i).

Table 42: Cu-Zeolite kinetic model

Symbol	Name	Reaction	Rate expression
r_1	NH_3 adsorption	$NH_3{+}\sigma \rightarrow NH_3{-}\sigma$	$AC_{NH3}(1-\theta_{NH3})$
r_2	NH_3 desorption	$NH_3{-}\sigma \rightarrow NH_3{+}\sigma$	$Ae^{\frac{-E(1-\varepsilon\theta_{NH3})}{RT}}\theta_{NH3}$
r_3	NH_3 oxidation	$2NH_3{+}2.5O_2 \rightarrow 2NO{+}3H_2O$	$Ae^{\frac{-E}{RT}}C_{O2}(C_{NH3})^2$
r_4	NO oxidation	$NO{+}0.5O_2 \rightarrow NO_2$	$Ae^{\frac{-E}{RT}}[(C_{O2})^{0.5}C_{NO}-\frac{C_{NO2}}{K_{eq}}]$
r_5	standard SCR	$4NH_3{-}\sigma{+}4NO{+}O_2 \rightarrow 4N_2{+}6H_2O{+}4\sigma$	$Ae^{\frac{-E}{RT}}C_{NO}(\theta_{NH3})^2$
r_6	fast SCR	$2NH_3{-}\sigma{+}NO{+}NO_2 \rightarrow 2N_2{+}3H_2O{+}2\sigma$	$Ae^{\frac{-E}{RT}}C_{NO}C_{NO2}\theta_{NH3}$
r_7	slow SCR	$4NH_3{-}\sigma{+}3NO_2 \rightarrow 3.5N_2{+}6H_2O{+}4\sigma$	$Ae^{\frac{-E}{RT}}C_{NO2}\theta_{NH3}$
r_8	N_2O formation	$2NH_3{-}\sigma{+}2NO_2 \rightarrow 2N_2{+}6N_2O{+}3H_2O{+}2\sigma$	$Ae^{\frac{-E}{RT}}C_{NO2}\theta_{NH3}$

All the above reactions are also provided with a pre-exponential factor (A_{pre}) and an activation energy (E_a) required to evaluate the reaction rate (Tab. 43).

Table 43: Model parameters

Name	A_{pre}	$E_a[J/(kmolK)]$
NH_3 adsorption	4.5	0
NH_3 desortption	$2.49 \cdot 10^5$	$9.75 \cdot 10^7$
NH_3 oxidation	$1.39 \cdot 10^6$	$6.38 \cdot 10^7$
NO oxidation	3.63	$3.21 \cdot 10^7$
standard SCR	$3.18 \cdot 10^8$	$8.80 \cdot 10^7$
fast SCR	$2.33 \cdot 10^7$	$3.21 \cdot 10^7$
slow SCR	$4.24 \cdot 10^5$	$5.83 \cdot 10^7$
N_2O formation	230	$2.45 \cdot 10^7$

In Tab. 42, σ represents the vacant sites available for these processes (it is assumed that the Cu-ZSM5 sites are all the same). The estimation of the local mass fraction (Y_i) was performed in Ansys through a convection-diffusion equation for each of the i-th species (Eq. (32)-Eq. (33)), where R_i is the sum of the production rates of the i-th species provided by the 8 mentioned reactions while S_i and J_i represent other source and the diffusion flux of the i-th species respectively [111].

$$(\rho Y_i)t + \nabla \cdot (\rho \vec{v} Y_i) = -\nabla \cdot \vec{J_i} + R_i + S_i \tag{32}$$

$$\vec{J_i} = -\rho D_{i,m} \nabla Y_i - D_{T,i} \nabla TT \tag{33}$$

7.1.2 Kinetic model validation in Ansys Fluent

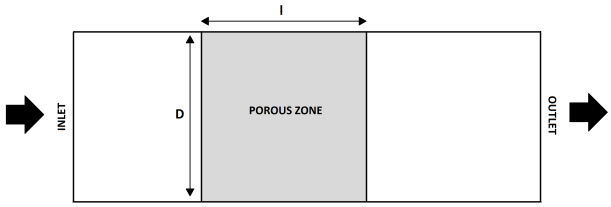

Figure 58: Test catalyst domain

The kinetic model in Section 7.1.1 was validated and tuned through a 2D CFD simulation in Ansys Fluent with the goal of reproducing as closely as possible the experimental results and the response of the kinetic model obtained in [109]. Specifically, a 2D catalyst model (Fig. 58) of diameter (D) and length (l) 0.75 inch and 0.83 inch respectively was constructed in Ansys DesignModeler and subsequently meshed using linear elements: other tests were conducted for different mesh size, which gave similar results, a circumstance that demonstrates the independence of the results from mesh size and thus their correctness. We next proceeded to the setup operation of the fluid dynamic problem by defining the inlet and outlet sections as mass flow inlet and pressure outlet respectively, while the remaining parts of the boundary were defined as walls: the contact condition between the porous zone, which represents the catalyst, and the free volume was then realized using interface boundary condition, which essentially are matching surfaces with different mesh topology. In order to be able to relate the initial 3D problem back to a 2D one, an equivalent mass flow rate ($\dot{m}_{eq}$)

was calculated in Eq. (34) (where A is the inlet area in 3D case), such as to ensure an equal average velocity at the inlet for the two cases.

$$\dot{m}_{eq} = \dot{m} \cdot \frac{D}{A} \tag{34}$$

The gas mixture was modeled as ideal gas and the turbulence model chosen was the standard $k-\varepsilon$. In addition, the type of chemistry solver used was Stiff Chemistry Solver while the interaction between turbulence and chemistry was modeled through Eddy-Dissipation Concept. Gas species composition at the catalyst inlet was set to $8\%\,H_2O$ and $5\%\,O_2$ with variable proportions of NH_3, NO_2 and NO while the remaining part was N_2. For the purpose of a complete characterization of the porous zone a geometric surface to volume ratio ($\frac{S}{V}$) of $4000\frac{1}{m}$ and a material porosity (or OFA) of 0.8 [112] were assumed while Eq. (37) was used to calculate the pressure gradient: the values of $\frac{S}{V}$ and OFA turn out to be close to those used in [113]. Surface to volume ratio was calculated assuming the use of a 400 cpi (cell per square inch) catalyst, which together with the OFA (open frontal area) value, provided an estimate of around 1 mm for the side of the catalyst square channel and thus a $\frac{S}{V}$ value of 4000. An additional input for Ansys was the surface site density (ρ_{den}), which was calculated through Eq. (35), considering an ammonia storage capacity (ρ_{stor}) of $90\frac{mol}{m^3}$ and a θ_{NH_3} equal to 0.01.

$$\rho_{den} = \frac{\rho_{stor}}{\theta_{NH_3}\frac{S}{V}} \tag{35}$$

The steady state solution was calculated using a pressure-based solver and a pseudo-transient mode. Simulations performed by gradually varying the temperature (Fig. 59) and GHSV (Fig. 60) conditions at the inlet show that the results obtained are in good agreement with data obtained in [109].

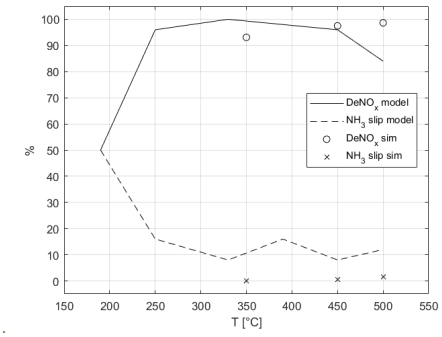

Figure 59: Validation plot for $GHSV = 36khr^{-1}$, $NO_x = 145ppm$, $\frac{NO_2}{NO_x} = 0.2$

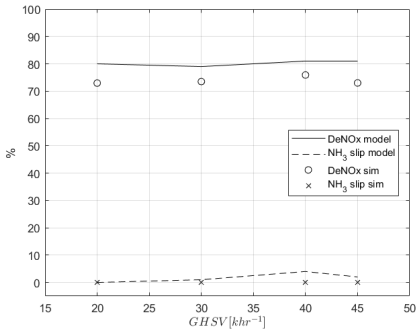

Figure 60: Validation plot for $T = 450C$, $NO_x = 450ppm$, $\frac{NO_2}{NO_x} = 0.2$

The convergence of the CFD model was evaluated using residuals of the various quantities of interest such as velocity, mass flow rate, energy and species: it was noticed that Y_i were more difficult to converge than the other quantities. Specifically, it has been established as convergence criterion that the value of residuals be at least 3 orders of magnitude lower than their peak value [114] and that, simultaneously, the weighted-area average concentration species at the outlet catalyst section converge toward a fairly stable value.

7.1.3 Innovative catalyst design

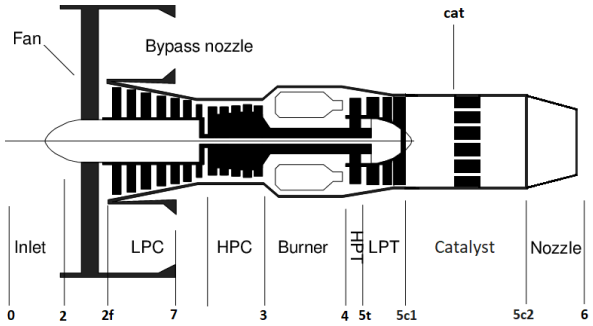

Figure 61: Turbofan model and section nomenclature

The catalyst design commonly adopted in mobile applications is the monolith type which consists in a cylindrical compact design with a series of square holes (typically 1 to 3mm side) homogeneously distributed along the entire cross section and an OFA of about $0.6-0.8$. This design is aimed at minimize the ratio between the volume of the catalyst and its exchange surface area, which is the seat of the catalytic processes, in particular at the sites contained within Cu-ZSM-5 which are accessible through surface porosity of different sizes. The monolith form is limited to low speed flows, partly because of the considerable generated pressure loss and partly because of the relatively high residence times necessary for an effective SCR. The pressure loss associated with a monolithic catalyst can be estimated with reasonable accuracy using Eq. (36) described in [115]: this relationship gives the pressure gradient drop ($\frac{\Delta P}{\Delta x}$) as a quadratic function of the upstream velocity (v_{cat}), where d_h is the hydraulic diameter of the catalyst channel and L is the thickness.

$$\frac{\Delta P}{\Delta x} = -\left[\left(\frac{32\mu}{d_h^2}\right) v_{cat} + \left(\frac{0.5}{2}\frac{\rho}{L}\right) v_{cat}^2\right] \tag{36}$$

Such a pressure gradient is implemented in the Ansys Fluent porous zone model by Eq. (37) [112] in which the values of α (material permeability) and C_2 (inertial resistance factor) are determined by equalizing Eq. (36) and Eq. (37).

$$\frac{\Delta P}{\Delta x} = -\left[\left(\frac{\mu}{\alpha}\right) v_{cat}^2 + \left(\frac{1}{2}C_2\rho\right) v_{cat}^2\right] \tag{37}$$

The value of ρ in Eq. (37) was determined, through simulation of a conventional turbofan in GSP 12, as the average value of the maximum ($1.0132\frac{Kg}{m^3}$) and minimum ($0.1772\frac{Kg}{m^3}$) values, identified by the conditions of static operation at maximum speed and cruise at low speed, respectively. This operation allows, assuming an average density value (ρ) equal to $0.5952\frac{Kg}{m^3}$ and μ as in Tab. 45b, to obtain for α and C_2 the values of $2.60010^{-8}m^2$ and $20.414\frac{1}{m}$ respectively ([113]). Generally in a HBPR turbofan, the core mass flow rate ($\dot{m}_c$) at full throttle can range between 50 to 100 $\frac{Kg}{s}$, depending on flight conditions, with a mean velocity downstream of LP turbine ($v_{5_{c1}}$ in Fig. 61) fairly stable around $200\frac{m}{s}$. According to Eq. (36), the direct use of a monolithic catalyst would cause a high pressure drop and would not guarantee a sufficiently high flow residence time within the catalyst to ensure good DeNOx efficiency: these considerations highlight the need for a catalyst with unconventional shape in order to ensure the lowest possible flow velocity at the entry of the catalyst holes

(v_{cat}) with reasonably low pressure drop. In this regard, the distinction between v_{cat} and $v_{5_{c1}}$ needs to be highlighted more clearly: in fact, although in the case of monolithic catalysts these two velocities nearly coincide ($v_{cat} \approx v_{5_{c1}}$) because the inlet section coincides with the inlet section of catalyst holes, in the present case, due to the unconventional shape, these velocities can be very different from each other (specifically $v_{cat} << v_{5_{c1}}$). The newly conceived catalyst (Fig. 64) consists in 8 elementary units (Fig. 63) connected by appropriate fittings (Fig. 62) to the annular outflow section of the LP turbine. Such a connection allows a smooth transition, in each of the units, from an annular (denoted by number 1 in Fig. 62) to a circular sector section (denoted by number 2 in Fig. 62), which has the advantage of having a higher ratio of outflow area to volume, an aspect of primary importance in this application. Specifically, it is the extrusion of this circular sector that forms the heart of the single catalyst unit: this shape is surrounded along its two lateral flat surfaces by a catalyst of constant thickness (s) equal to $0.10m$, which has square channels of size $1mm$ directed orthogonally to the outlet to which they refer (vectors $\vec{k}'$ and $\vec{k}''$ in Fig. 63). For this proposed type of catalyst geometry no references have been found in the literature for the estimate of the ΔP and, for this reason, its calculation was carried out using Fluent. The proposed catalyst, however, may have the disadvantage of reducing the net thrust (F) of the turbofan core and thus a reduction in performance compared to conventional turbofan: this performance decay arises partly because of the resistance introduced by turning the flow consequent to the settlement of catalyst walls arranged orthogonaly to the motor axis and partly because of the passage throught the catalyst holes. This increase in drag force was implemented in the turbofan model through a decrease in total pressure (Section 7.1.7).

7.1.4 Catalyst CFD simulation Setup

For the purpose of easier handling and less computational effort, only a representative portion of the flow of the entire catalyst, consisting essentially in a single catalyst unit, was simulated (Fig. 63): in fact, because of flow symmetry, the 8 portions of the fluid domain have the same solutions in terms of velocity, pressure, temperature and gas composition, so only one of them will be the subject of the 3D CFD simulation. The types of inlet and outlet boundary conditions chosen for the CFD simulation of the catalyst are velocity inlet and pressure outlet, respectively.

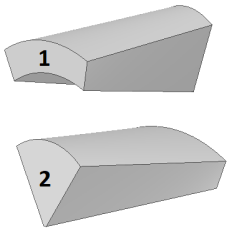

Figure 62: Catalyst fittings allows section transition

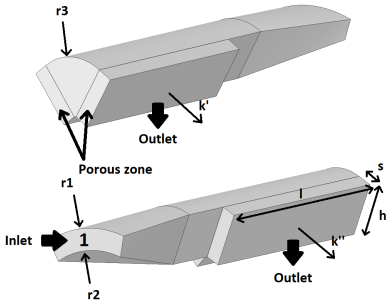

Figure 63: Boundary conditions for single catalyst unit (other surfaces are walls)

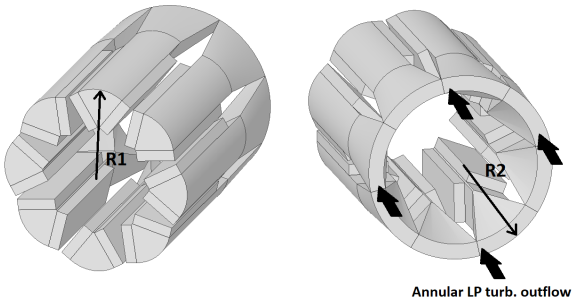

Figure 64: Catalyst 3D design and section

The catalyst dimensions, shown in Tab. 44, were obtained through the process described in Section 7.1.8, starting from assumptions about the design performance (Section 7.1.6), the component outlet mach (Tab. 47) and the constraint on $v_{5_{c2}}$ (Eq. (40)): this process allowed the determination of the catalyst total inlet and outlet areas ($A_{5_{c1}}$ and $A_{5_{c2}}$), which allowed, having fixed the shape of the catalyst, to calculate its relative dimensions.

Table 44: Geometric parameters

Parameter	**Value** [mm]
r_1	850
r_2	732
r_3	378
h	378
s	100
l	530

Fig. 63 comprehensively describes the geometry of the individual catalyst unit and highlights important aspects for CFD simulation as inlet and outlet sections and the division into the two regions of porous zone (representative of the catalyst) and free volume. In order not to increase the engine frontal area, R_1 was chosen to be nearly coincident with the outer radius of the LP turbine outflow section of a Rolls-Royce Trent 1000 turbofan: the inner radius of the LP turbine outflow section (r_2) was derived through preliminary design analysis from the design parameters contained in Tab. 46a- 46b and the assumption on $F_{cruise} = 68.268kN$ and $\dot{m}_{cruise} = 455\frac{Kg}{s}$. The CFD setup was carried out similarly to what done for the validation of the kinetic model except for the gas compositions (Tab. 45a), assumed similar to turbojet exhaust [116], and mixture properties [117] (Tab. 45b).

Table 45

(a) Exhaust gasses composition

Species	**Mass fraction [adim]**
H_2O	0.0193
O_2	0.2002
N_2	0.78015
NH_3	$1.3 \cdot 10^{-4}$
NO	$1.8 \cdot 10^{-4}$
NO_2	$1.8 \cdot 10^{-5}$
N_2O	$2 \cdot 10^{-5}$

(b) Mixture propriety

Symbol	**Characteristic**	**Value**
λ	thermal conductivity	$0.0454\frac{W}{m \cdot K}$
μ	dynamic viscosity	$3 \cdot 10^{-5}\frac{Kg}{m \cdot s}$

For the catalyst CFD analysis, the same convergence criterion of Section 7.1.2 was used.

7.1.5 Nozzle CFD simulation Setup

Fig. 65 shows the selected nozzle shape and highlights the presence of 4 symmetry planes that allow the identification of a portion of the fluid domain representative of the entire nozzle volume: this portion has been isolated in Fig. 66, where the boundary conditions required for CFD analysis are briefly described. Specifically the nozzle receives a low velocity flow directed according to the local vector $\vec{y}$ (but in the opposite direction), which is orthogonal to the direction of the engine axis ($\vec{x}$), and due to its geometry allows the flow to rotate 90° in order to align with $\vec{x}$. The flow is then accelerated in the converging part of the nozzle until exhaust section (A_e). The types of inlet and outlet boundary conditions chosen for CFD simulation of the nozzle are pressure inlet and pressure outlet, respectively. Such a nozzle simulation requires a good overlap of the performance determined by the 0D turbofan model, made in GSP 12, with the data provided by the CFD model. Generally, in fact, the performance of these models will not coincide because in the GSP turbofan model the nozzle is necessarily convergent while in the CFD model the geometry is more complex. In order to ensure tuning of the two models, it was therefore thought to incorporate this shape difference in a speed correction coefficient on the nozzle outflow section (C_v), which is supposed to be constant in all flight conditions. As explained in GSP 12 user manual, C_v is a measure of the efficiency losses of the expansion process in the nozzle and specifically represents the difference between the ideal (v_e) and actual efflux velocity. The effect of C_v on F, as implemented in the GSP 12 software, can be briefly described for a turbojet in Eq. (38).

$$F = \dot{m}_e \left(C_v \cdot v_e - v_0\right) + A_e \left(P_e - P_{atm}\right) \tag{38}$$

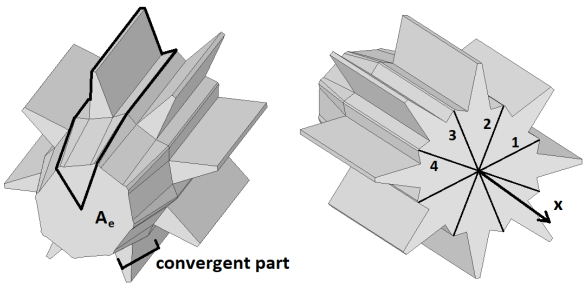

Figure 65: 3D nozzle representation

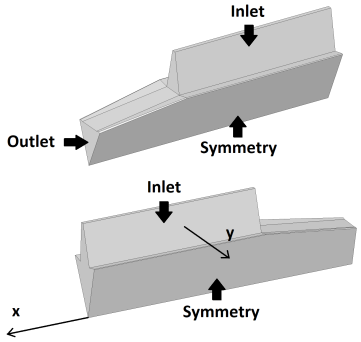

Figure 66: Nozzle boundary conditions (remaining surfaces are walls)

Finally, the assembly of the catalyst (Fig. 64) and nozzle (Fig. 65) is presented in Fig. 67.

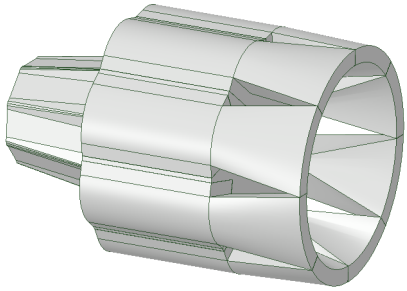

Figure 67: Catalyst and nozzle assembly

7.1.6 Turbofan reference model

The engine model used as reference is the Rolls-Royce Trent 1000 and its design performance parameters, derived from the type certificate [11] and ICAO databank [12], serve as the basis for the chosen cruising quantities in Tab. 46a.

Table 46

(a) Trent 1000 cruise data

Characteristic	Value
π_d	0.98
π_f	1.54
π_c	32.4675
π_b	1
N_{LP}	2683 rpm
N_{IP}	11164 rpm
N_{HP}	11164 rpm
α	9.12

(b) Component efficiencies in cruise

η	Value
η_f	0.90
η_c	0.90
η_{tHP}	0.93
η_{tLP}	0.93
η_b	0.9612

Core (A_e) and bypass (A_{byp}) nozzle area are $0.41m^2$ and $3.20m^2$ respectively. For cruising conditions, in the absence of data provided by the manufacturer, component efficiencies in Tab. 46b and $f = \frac{1}{42}$ have been assumed. In the current turbofan model the gas is considered ideal and H_i was chosen equal to 43.26 $\frac{KJ}{Kg}$.

7.1.7 Catalyst modelling in GSP 12

In order to characterize the catalyst operations the parameter π_{cat}, defined in Eq. (39), is used.

$$\pi_{cat} = \frac{P_{t_{5c2}}}{P_{t_{5c1}}} = \frac{P_{5_{c2}}\left[1+\frac{\gamma'-1}{2}Ma_{5_{c2}}^2\right]^{\frac{\gamma'}{\gamma'-1}}}{P_{5_{c1}}\left[1+\frac{\gamma'-1}{2}Ma_{5_{c1}}^2\right]^{\frac{\gamma'}{\gamma'-1}}} \tag{39}$$

Considering the flow through the catalyst as adiabatic ($T_{t5_{c2}} = T_{t5_{c1}}$), we have that the coefficient π_{cat} completely defines the thermodynamic state (P, T, ρ) of the outlet gas: π_{cat} will be first initiated as 0.86 and calculated for every flight condition using recursive algorithm shown in Section 7.1.9. The turbofan model assembled in GSP 12 is shown in Fig. 61. Since

there are no components in the GSP 12 libraries that can specifically emulate the operation of a catalyst, it was chosen to simulate such operation through the "Duct" component. This component idealizes the operation of a duct, the inefficiencies of which are realized by total pressure ratio (π_{duct}) between inlet and outlet section and heat losses (Q) through its walls. In GSP 12 this component needs as input the value of cross-sectional area of the inlet ($A_{5_{c1}}$) and outlet ($A_{5_{c2}}$) sections, or equivalently the corresponding values of the flow Machs under design conditions ($Ma_{5_{c1}}$ and $Ma_{5_{c2}}$ respectively). For all the component outlets an realistic assumption about the mach flow in design condition has been made (Tab. 47) and provided to GSP 12.

Table 47: Outlet efflux mach for different components

Inlet (Ma_2)	**Fan** (Ma_{2f})	**Compr.** (Ma_3)	**Burner** (Ma_4)	**HP turb.** (Ma_{5t})	**LP turb.** ($Ma_{5_{c1}}$)
0.4	0.4	0.4	0.3	0.4	0.35

7.1.8 Turbofan rotating maps scaling and catalyst sizing

Algorithm shown in Fig. 68 essentially performs the scaling of the turbofan rotary component maps and calculates the value of total inlet ($A_{5_{c1}}$) and outlet ($A_{5_{c2}}$) area of the catalyst. In Fig. 68, the turbofan map scaling is essentially accomplished by building in GSP 12 the turbofan model with catalyst (as shown in Section 7.1.7) and performing a simulation under design conditions: this simulation will also perform map scaling. GSP turbofan model (Fig. 68) takes as input $(Ma_0, z, f)_{cruise}$, design parameters (Tab. 46a - 46b) and the efflux mach from catalyst ($Ma_{5_{c2}}$): $Ma_{5_{c2}}$ value initially represents simple guess value, which is confirmed only if the calculated turbofan performance are such that Eq. (40) is satisfied.

$$v_{5_{c2}} \approx 40\frac{m}{s} \tag{40}$$

Choosing $Ma_{5_{c2}} = 0.0694$, we get, for the design condition and parameters expressed in Section 7.1.6, $v_{5_{c2}} = 39.5\frac{m}{s}$, which is enough close to the condition given in Eq. (40). The outputs of the algorithm in Fig. 68 are the rotating components maps, $A_{5_{c2}}$ and $A_{5_{c1}}$. The values of $A_{5_{c2}}$ and $A_{5_{c1}}$ are found to be $3.15m^2$ and $0.585m^2$ respectively.

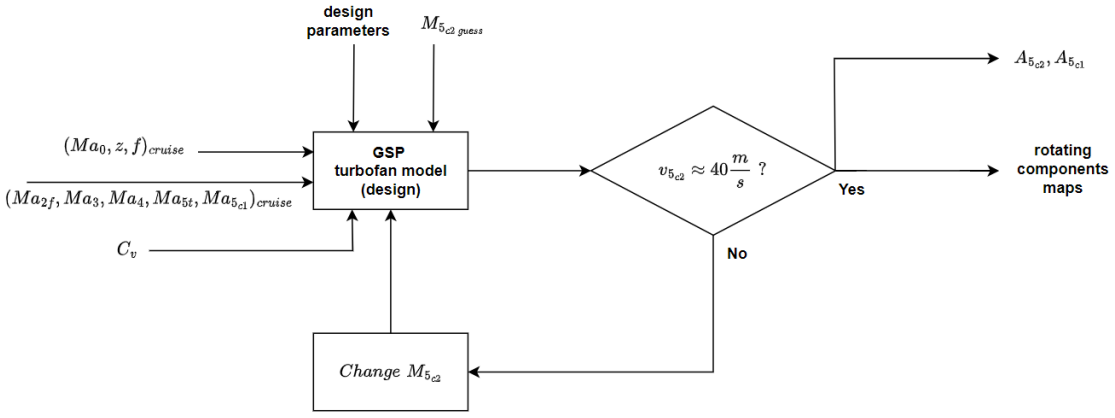

Figure 68: Turbofan map scaling

7.1.9 Interaction algorithm between CFD models and GSP 12 turbofan model

GPS turbofan model in Fig. 69 is an off-design performance model built in GSP 12 and has the objective of generating turbofan off design performance and in particular values of the variables $P_{5_{c1}}$,$T_{5_{c1}}$,$v_{5_{c1}}$ and $P_{5_{c2}}$,$T_{5_{c2}}$, P_6, which are required to realize the CFD catalyst and nozzle simulation. GSP turbofan model requires as input the flight condition (Ma_0, z and f), C_v, $\pi_{cat_{guess}}$ and the rotating components maps (derived at Section 7.1.8). Specifically C_v is choosen equal to 0.88 to best match GSP turbofan data with CFD nozzle output.

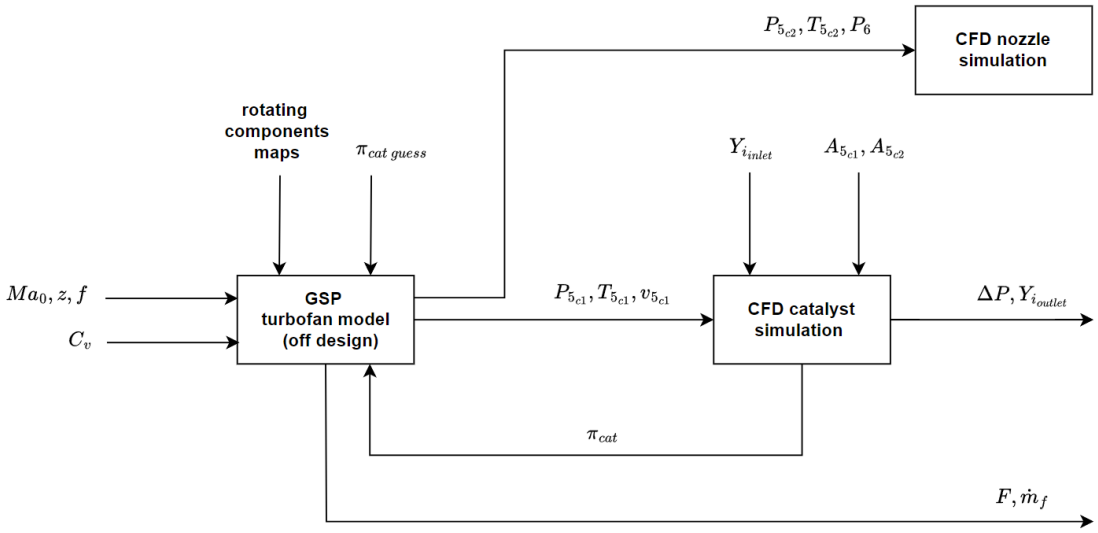

Figure 69: Algorithm for turbofan performance and NOx emissions simulation

$P_{5_{c1}}$, $T_{5_{c1}}$, $v_{5_{c1}}$ and catalyst inlet gas composition ($Y_{i_{inlet}}$) are then utilized to define the boundary conditions for the CFD catalyst simulation (as illustrated in Section 7.1.4). The CFD catalyst simulation provides an estimate of π_{cat} which is compared with the value of $\pi_{cat_{guess}}$: if $\pi_{cat} - \pi_{cat_{guess}} > \varepsilon$ (where ε is a very small quantity, chosen at will by the user) it is necessary to repeat the above steps, imposing $\pi_{cat_{guess}} = \pi_{cat}$ and generating through a new simulation of the GSP turbofan model a new set of $P_{5_{c1}}$, $T_{5_{c1}}$ and $v_{5_{c1}}$. Otherwise, if $\pi_{cat} - \pi_{cat_{guess}} < \varepsilon$, the value of π_{cat} has reached convergence. It can be seen that convergence and good accuracy of the result is usually achieved in 3 iterations. The CFD catalyst simulation provides now the ΔP as well as the species mass fractions of the gas leaving the catalyst ($Y_{i_{outlet}}$). Value of $P_{5_{c2}}$, $T_{5_{c2}}$ and P_6 are then used to perform the CFD simulation for the nozzle flow (as in Section 7.1.5) in order to determine the flow properties on the outflow section. While the maps scaling operations are performed only once (for the design condition), the operations contained in Fig. 69 are performed for every desired flight condition (Ma_0, z and f).

7.2 Results

The results obtained from the simulation performed according to the scheme depicted in Section 7.1.9 are now presented: these quantities are compared, for the different flight conditions in Tab. 48, with the assumptions made in Section 7.1.7 in order to verify the accuracy of the proposed method. In Section 7.2.2, a comparison of F, $\dot{m}_{fuel}$, $TSFC$ and $T_{5_{c2}}$ provided

by a catalyst-equipped turbofan in different flight performance is made. These performance are then compared with that of a conventional turbofan having the same design parameters.

7.2.1 Simulation errors

Table 48: Simulation flight conditions

Flight cond.	$z[m]$	Ma_0	f
cruise	11000	0.85	0.0238
climb	4000	0.45	0.0280
take off	0	0.20	0.0300

Tab. 48 shows the flight conditions for which simulations are carried out. For each of these flight condition, 3 iteration of the variable π_{cat}, in the algorithm of Section 7.1.9, have been performed: their values are shown in Tab. 49.

Table 49: Value of π_{cat} in the various iterations of the algorithm in Fig. 69

	Cruise			**Climb**			**Take off**		
	1° iter.	2° iter.	3° iter.	1° iter.	2° iter.	3° iter.	1° iter.	2° iter.	3° iter.
π_{cat}[adim]	0.8600	0.8875	0.8824	0.8600	0.9078	0.8978	0.8600	0.9142	0.9030

At the third iteration, the values of the variables $P_{5_{c1}}$, Ma_6 and P_6 provided by the GSP turbofan model and the CFDs of the nozzle and catalyst were taken (Tab. 50): from these, the percentage error (error %) was then calculated, which is an indication of the error in the estimation of a given variable. As can be seen from Tab. 50, there is virtually zero error in the estimation of Ma_6 and a maximum error of about 1.6% in the determination of $P_{5_{c1}}$. In contrast, the maximum error in estimating P_6 turns out to be higher, around 5.5%, but nevertheless is acceptable in the overall turbofan performance estimation.

Table 50: Simulation errors

	Cruise			**Climb**			**Take off**		
	GSP 12	CFD	error %	GSP 12	CFD	error %	GSP 12	CFD	error %
$P_{5_{c1}}$ $[Pa]$	94742	95089	0.365	190752	193860	1.6293	282392	283280	0.3145
Ma_6 $[adim]$	1.00	1.00	0.0	1.00	1.00	0.0	1.00	1.00	0.0
P_6 $[Pa]$	39787	42008	5.58	83435	87648	5.04	123202	129250	4.91

7.2.2 Turbofan performances

The results obtained make it possible to state that, at least limited to the flight conditions considered, there is a low pressure loss ΔP between inlet and outlet of the catalyst, which is found to be almost constant around $5000Pa$ (Tab. 51).

Table 51: Value of ΔP for different flight conditions

	Cruise	**Climb**	**Take off**
ΔP $[Pa]$	-4545	-5108	-5488

Concerning the overall performance of the turbofan, the values of F, $TSFC$ and $\dot{m}_{fuel}$ present similar trends (Tab. 52) to those of a conventional turbofan at varying flight conditions (Ma_0, z and f).

Table 52: Performance turbofan with catalyst

	Cruise	**Climb**	**Take off**
$F\ [KN]$	64.133	176.138	321.52
$TSFC\ [\frac{N}{Kg \cdot h}]$	0.06007	0.04993	0.04179
$\dot{m}_{fuel}\ [\frac{Kg}{s}]$	1.0701	2.4428	3.7327
$T_{cat}\ [K]$	843	960	1017

A comparison of the performance of a catalyst-equipped turbofan versus a conventional one having the same design parameters as in Tab. 46a - 46b is made in Tab. 53: as expected there is a modest decrease in F, which is more pronounced in cruise conditions (-4.2791%) than in takeoff conditions (-2.7681%). A slight increase in $\dot{m}_{fuel}$ is also noted. For $TSFC$ similar considerations made for F apply.

Table 53: Performance comparison

	Cruise	**Climb**	**Take off**
$\Delta F\ [N]$	-4.2791 %	-3.1890 %	-2.7681 %
$\Delta TSFC\ [\frac{N}{Kg \cdot h}]$	4.4696 %	3.7183 %	3.1852 %
$\Delta\dot{m}_{fuel}\ [\frac{Kg}{s}]$	0.0 %	0.4152 %	0.3603 %

7.2.3 Catalyst $DeNO_x$ and $NH_{3\,slip}$

The average mass fractions of NO ($\bar{Y}_{NO}$), NH_3 ($\bar{Y}_{NH_3}$), NO_2 ($\bar{Y}_{NO_2}$) and N_2O ($\bar{Y}_{N_2O}$), $DeNO_x$ and $NH_{3\,slip}$ at the catalyst outlet section are presented in Tab. 54 for cruise condition. The average mass fractions ($\bar{Y}$) are calculated through the area-weighted average formula while $DeNO_x$ and NH_3 values are calculated using Eq. 41 - 42.

$$DeNO = \left(\frac{\bar{Y}_{NO_{inlet}} - \bar{Y}_{NO_{outlet}}}{\bar{Y}_{NO_{inlet}}} \right) \cdot 100 \tag{41}$$

$$NH_{3\,slip} = \left(\frac{\bar{Y}_{NH_{3\,outlet}}}{\bar{Y}_{NH_{3\,inlet}}} \right) \cdot 100 \tag{42}$$

The CFD results show that, in general, NO and NH_3 concentration (Fig. 70 and Fig. 71) are highest near the bottom of the catalyst outlet and decrease proceeding in the $\vec{x}$ direction (where the $\vec{x}$ points in the forward direction of the engine) with the only exception of small areas located in the far left, where a sharp increase in the respective concentrations can be seen. These are determined, totally or in part, by the presence of a backflow: this condition appears to be caused by a mild flow vorticity, which results in the establishment of an adverse gradient that leads to reverse flow over a portion of the catalyst. The species mass fraction of the backflow were assumed to be the same as the catalyst inlet.

Table 54: Species average mass fractions at catalyst outlet

	$\bar{Y}_{NO}$	$\bar{Y}_{NH_3}$	$DeNO_x$	$NH_{3\,slip}$	$\bar{Y}_{NO_2}$	$\bar{Y}_{N_2O}$
cruise	$1.76 \cdot 10^{-5}$	$2.84 \cdot 10^{-5}$	90.22 %	21.84 %	$1.17 \cdot 10^{-6}$	$2.03 \cdot 10^{-5}$

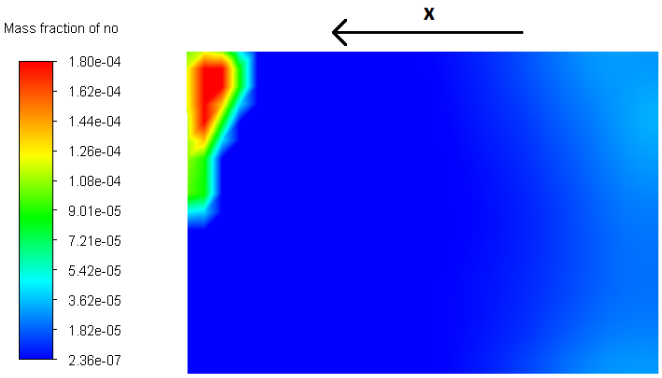

Figure 70: NO mass fraction distribution along the catalyst outlet in cruise

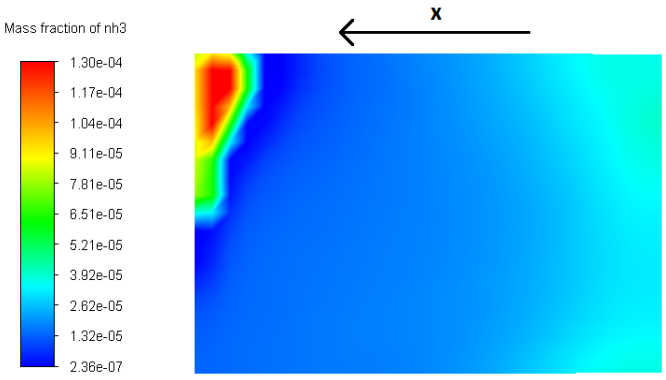

Figure 71: NH_3 mass fraction distribution along the catalyst outlet in cruise

One of the most onerous operating condition for the catalyst is the take-off phase: in fact, under such conditions, the temperature of the LP turbine efflux gases is near maximum, around $1000K$ for the present turbofan, leading to a drastic $DeNO$ reduction and a considerable $NH_{3_{slip}}$ increase. However, this condition cannot be simulated without major errors by CFD because the kinetic model used is tuned over a temperature range up to $775K$, which is much lower than the $1017K$ temperature reached by the catalyst.

7.2.4 Velocity distribution

The inhomogeneous concentration of NO_x and NH_3 in the outlet section should be attributed to the inhomogeneous velocity distribution throughout the catalyst. As can be seen in Fig. 72, the velocity is significantly higher in the areas near the bottom of the catalyst outlet (in the far right side) and tends to decrease, initially with a high gradient, moving away from it along the $\vec{x}$ axis. This situation appears comparable to the distribution of NO, which seems to imply a causal link with regions of higher velocity corresponding to regions of higher NO concentration and vice versa (although this relationship is highly nonlinear); similar observations can be made for the NH_3 concentration.

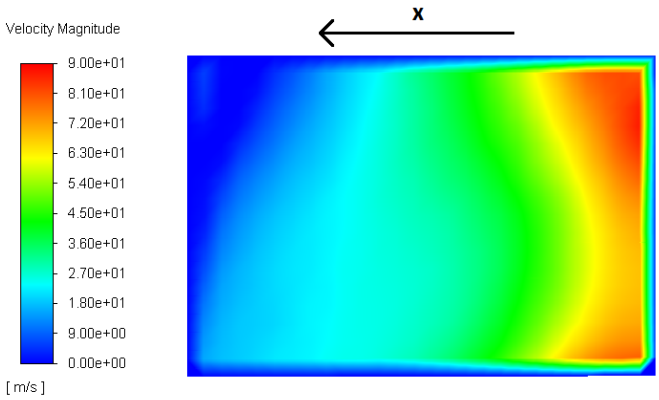

Figure 72: Velocity distribution along the catalyst outlet in cruise

7.3 Conclusions

Among the major disadvantages associated with the use of a catalyst in a turbofan there is the substantial increase in weight as well as moderate increment in engine front cross section, which would make its installation under the wing not desirable because of the significant increase in aerodynamic drag. To obviate this problem integrated turbofan solutions can be adopted [118]. The results obtained in this thesis show that, compared with a conventional turbofan having the same design parameters, there is a small reduction in thrust, of around 3% to 4%. Because of the limitations on temperature given by the kinetics of the SCR process on Cu-ZSM5, the possible conditions for application of this technology to turbofans are only near cruise condition. In this condition the use of the catalyst leads to an high GHSV, compared to those found in a normal car, and a large reduction in NO_x concentration (around 90%). However, all remaining flight phases (climb and take off) turn out to be incompatible, in terms of gas temperatures, with NO_x selective catalysis reduction processes: in such phases therefore, total ammonia flow interruption would be appropriate. Another important aspect is the formation of N_2O, which, although present in very small quantities, has a severe environmental impact due to its strong greenhouse effect. Future developments of this application will focus on similar design but more advanced catalyst materials that could allow NO_x reduction and NH_{3slip} values compatible with potential industrial applications in most of the flight conditions.

8 Funding Sources

This work was the supported by PON REACT-EU Ricerca e Innovazione 2014-2020 D.M.N. 1061 of 10 Agosto 2021, Azione IV.5 “Dottorati su Tematiche Green” (XXXVII ciclo) with grant DOT20KTEXX $n°3$.

A Appendix

- The Figures below (Fig. 73) are showing the concentration profiles of different species as the non-PZ mass flow distribution changes.

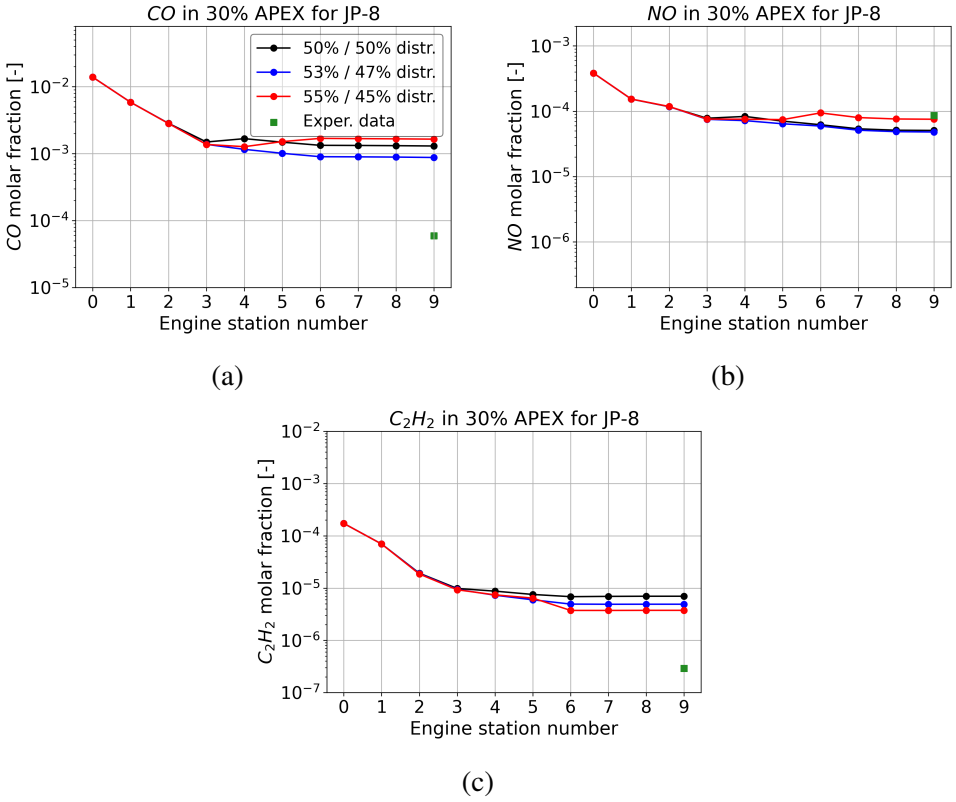

Figure 73: Concentration profile of CO, NO and C_2H_2 for different non-PZ mass flow distribution

- The Eq. (29) is derived from the definition of t (Eq. (43)) and the law of perfect gases (Eq. (44)).

$$t = \frac{\rho V}{\dot{m}} \tag{43}$$

$$P = \rho \bar{R} T \tag{44}$$

- Below are graphs for species C_2H_4, C_4H_6, C_2H_6, C_3H_8, CH_3OH, O_2 under APEX flight conditions.

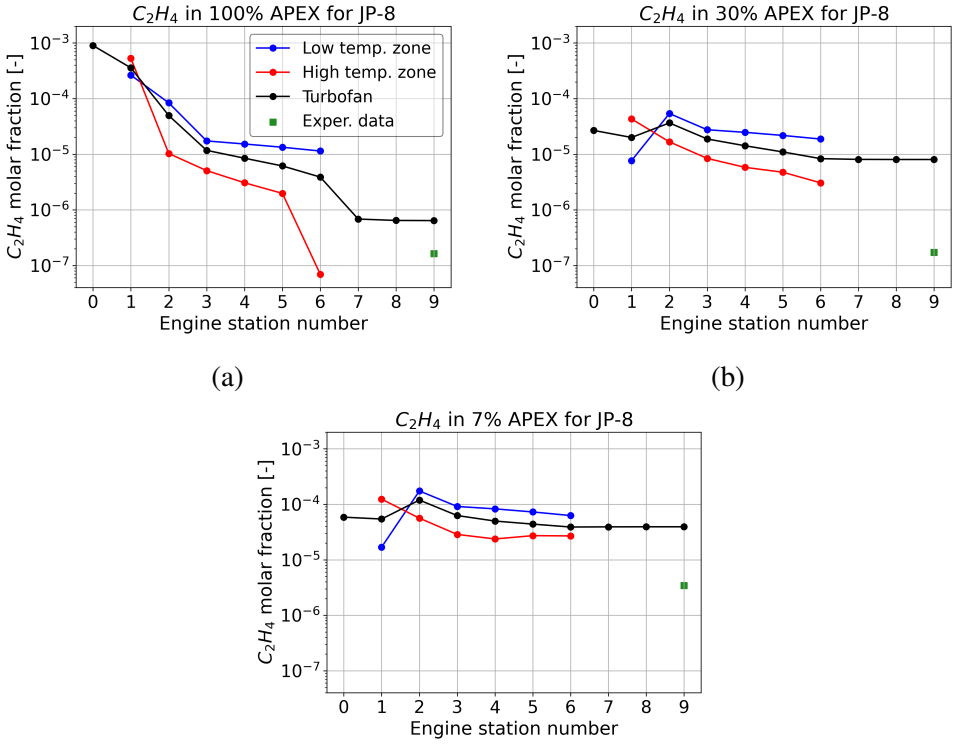

(a) (b)

(c)

Figure 74: C_2H_4 concentration profile in APEX conditions for decreasing throttle

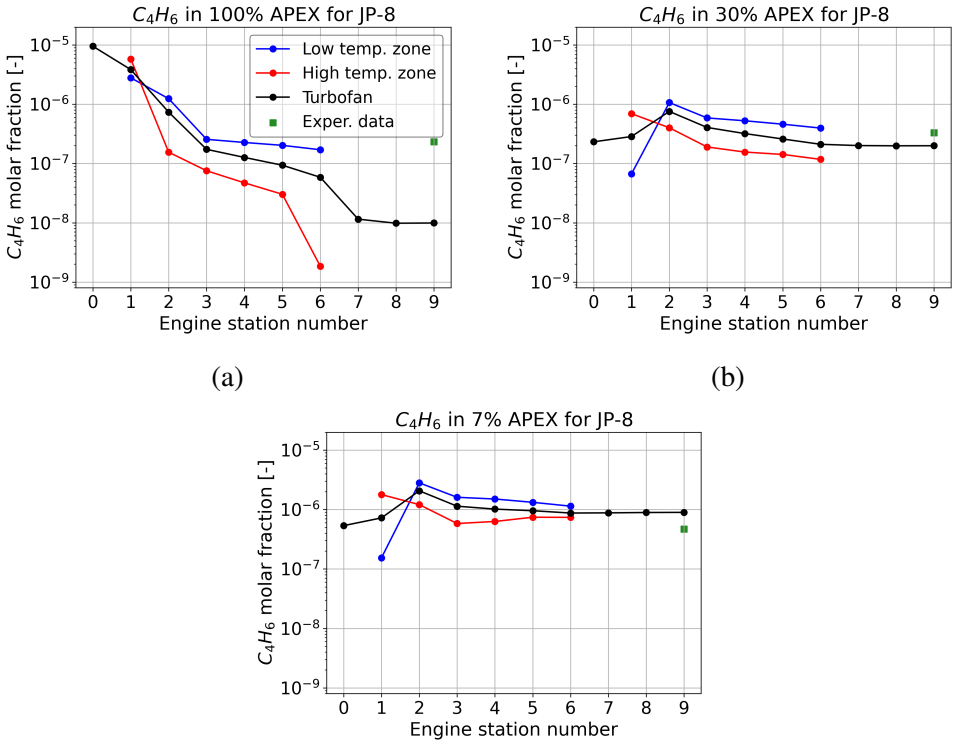

(a) (b)

(c)

Figure 75: C_4H_6 concentration profile in APEX conditions for decreasing throttle

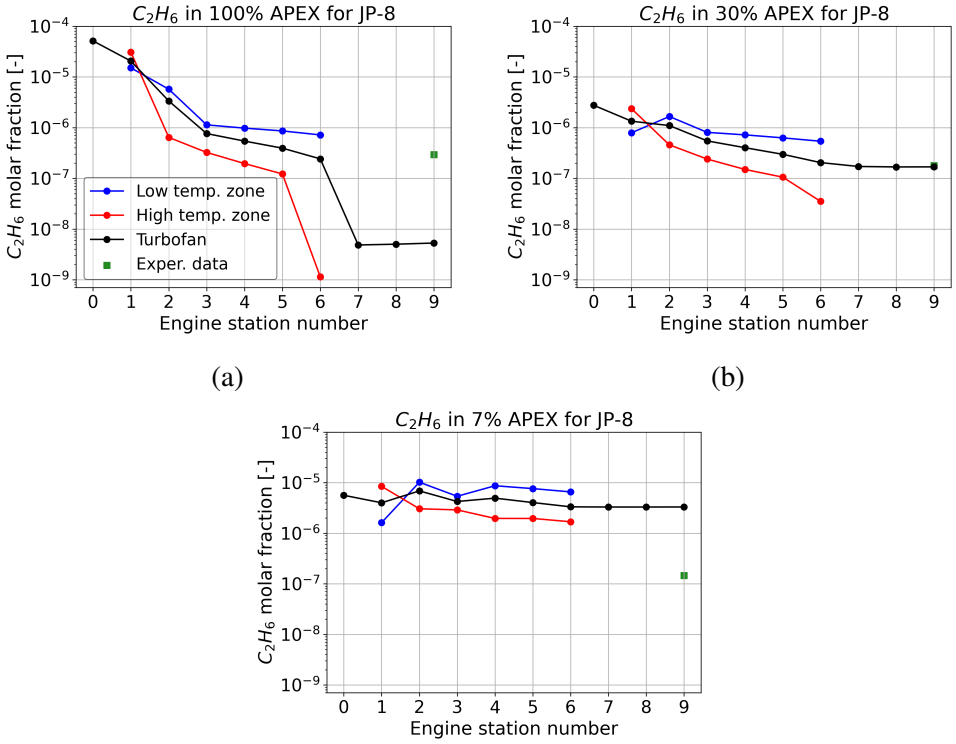

(a) (b)

(c)

Figure 76: C_2H_6 concentration profile in APEX conditions for decreasing throttle

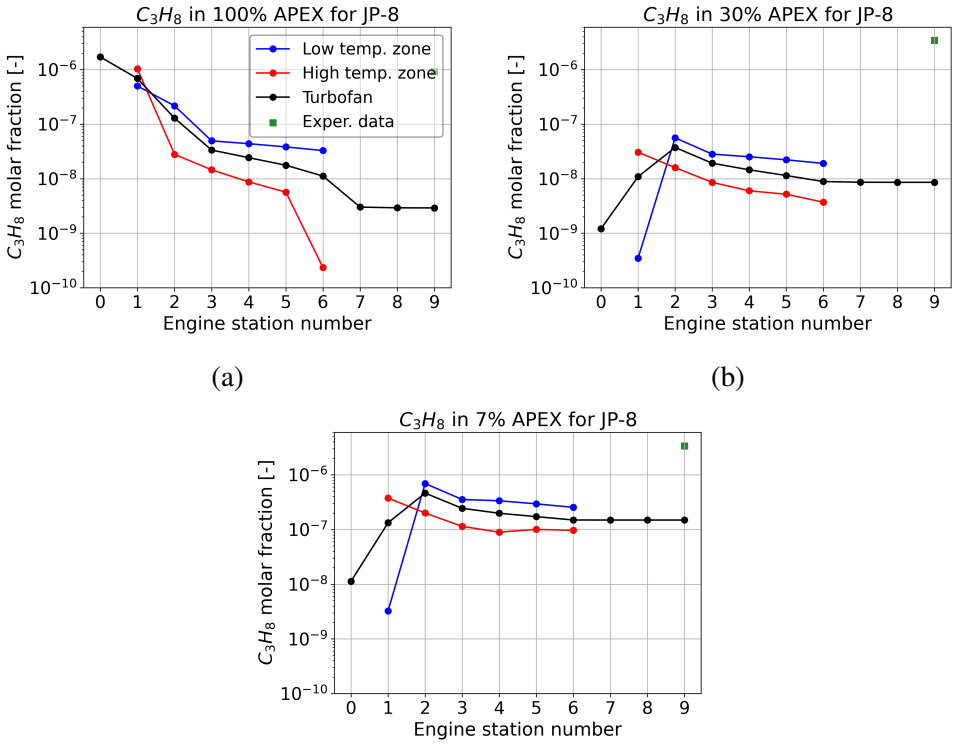

(a) (b)

(c)

Figure 77: C_3H_8 concentration profile in APEX conditions for decreasing throttle

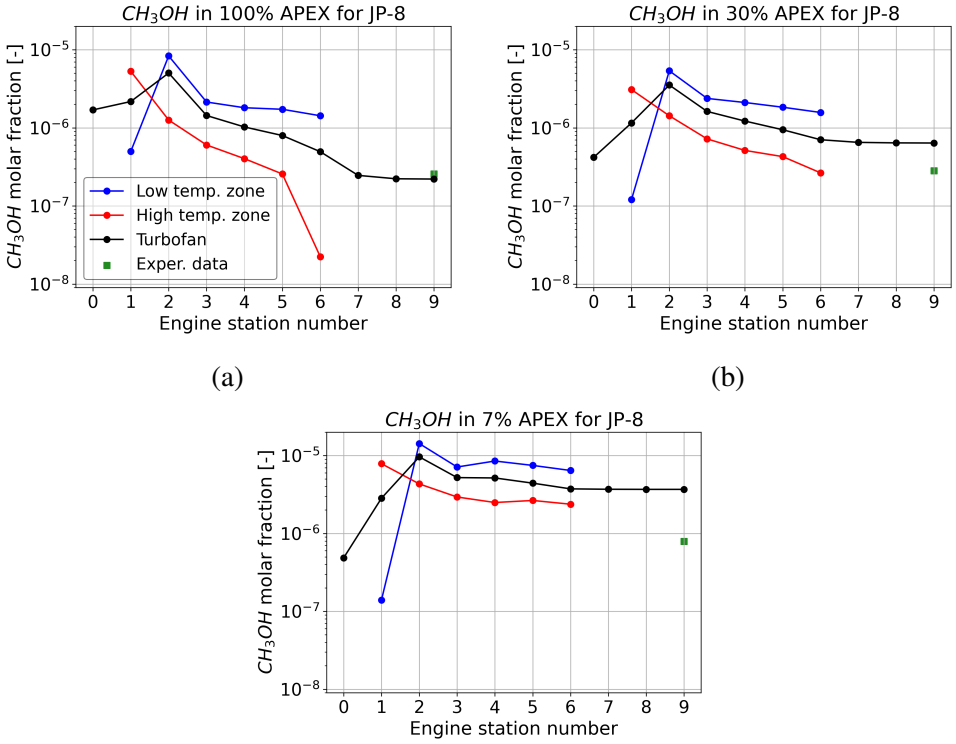

(a) (b)

(c)

Figure 78: CH_3OH concentration profile in APEX conditions for decreasing throttle

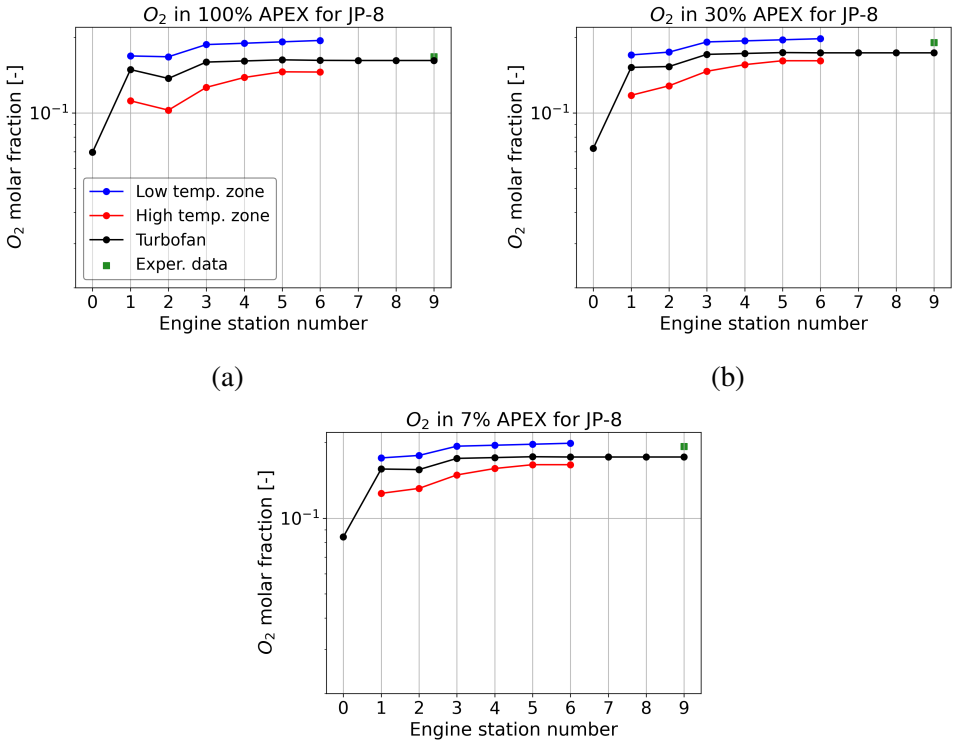

(a) (b)

(c)

Figure 79: O_2 concentration profile in APEX conditions for decreasing throttle

- The model inputs and parameters for Case 1 and Case 2 conditions (Table 55) are derived using using the turbofan model detailed in Section 5.1.6 and are listed in Table 56.

Table 55: Case 1 and Case 2 flight conditions

Flight condition	Ma_0 $[adim]$	z $[m]$	f $[adim]$	Fuel type used
Case 1	0.6	12000	0.025	JP-8
Case 2	0	0	0.025	JP-8

Table 56: Parameters and inputs for model validation on Case 1 and Case 2

Input type	Case 1	Case 2
P_{comb} $[Pa]$	$5.79 \cdot 10^5$	$19.05 \cdot 10^5$
T_{comb} $[K]$	712	763
f $[adim]$	0.0250	0.0250
$\dot{m}_{fuel}$ $[\frac{Kg}{s}]$	0.403	1.315
π_{tHP} $[adim]$	3.146	3.121
π_{tLP} $[adim]$	5.240	4.657
π_e $[adim]$	1.883	1.342
$\dot{m}_{PZ}$ $[\%]$	24.40	24.40
t_{PZ} $[msec]$	2.5	2.2
$\dot{m}_{SZ}$ $[\%]$	25.76	25.76
t_{SZ} $[msec]$	0.8*	0.8*
$\dot{m}_{DZ}$ $[\%]$	21.82	21.82
t_{DZ} $[msec]$	0.8*	0.8*
$\dot{m}_{cool}$ $[\%]$	28.01	28.01

*Note: 0.3 for PSR near SZ holes

The radial temperature profiles for the Case 2 condition are shown here (Fig. 80).

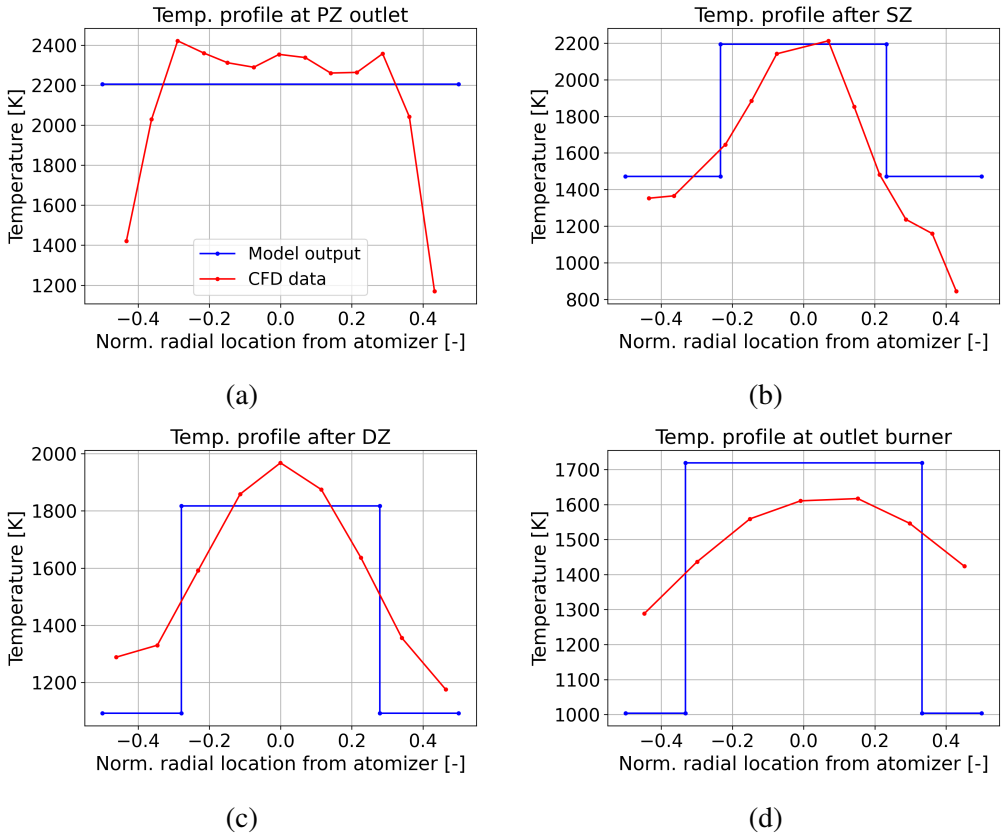

Figure 80: Validation plot on CFD simulations at $z = 0m$, $Ma_0 = 0$ and $f = 0.025$ (Case 2)

- The single-step combustion kinetic model used for the CFD calculation is shown in Equation 45.

$$C_{11}H_{23} + O_2 \rightarrow CO_2 + H_2O \tag{45}$$

Table 57: Turbofan model sections calculated by GSP12

A_{tHP} inlet $[mm^2]$	A_{tLP} inlet $[mm^2]$	A_e inlet $[mm^2]$	A_e outlet $[mm^2]$
574	1236	3516	3490

Table 58: Pressure ratios provided by GSP12 off-design performance

Flight condition	π_{tHP} $[adim]$	π_{tLP} $[adim]$	π_e $[adim]$
7% APEX	2.86	2.27	1.05
30% APEX	2.89	2.33	1.05
100% APEX	3.13	4.01	1.21
Low power ACCESS	3.16	4.67	1.34
Medium power ACCESS	3.15	4.93	1.44
High power ACCESS	3.13	5.18	1.61

Table 59: Tear Stream Control settings

Algorithm	Absolute tolerance	Relative tolerance	Max iterations	Relaxation factor
Relaxation	10^{-11}	10^{-6}	3000	0.4

References

[1] K. Kuklinska, L. Wolska, J. Namiesnik, Air quality policy in the u.s. and the eu – a review, Atmospheric Pollution Research 6 (1) (2015) 129–137. doi:10.5094/APR.2015.015.

[2] ACARE, Fly the green deal, europe's vision for sustainable aviation, https://www.acare4europe.org/wp-content/uploads/2022/06/20220815_Fly-the-green-deal_LR-1.pdf, (2022).

[3] A. Evans, G. Follen, C. Naiman, I. Lopez, Numerical propulsion system simulation's national cycle program, 34th AIAA/ASME/SAE/ASEE Joint Propulsion Conference and Exhibit (1998). doi:10.2514/6.1998-3113.

[4] W. Visser, Generic analysis methods for gas turbine engine performance: The development of the gas turbine simulation program gsp, Ph.D. thesis, TU Delft, https://doi.org/10.4233/uuid:f95da308-e7ef-47de-abf2-aedbfa30cf63, (2015).

[5] Ohio Aerospace Institute, Npss user guide, http://www.wolverine-ventures.com/userdocs/version241_docs/UserGuide.pdf (2012).

[6] G. A. Mist'e, E. Benini, Improvements in off design aeroengine performance prediction using analytic compressor map interpolation, Int. journal of turbo and jet engine 29 (2) (2012) 69–77. doi:10.1515/tjj-2012-0012.

[7] G. Liu, X. Han, K. Y. Lam, A combined genetic algorithm and nonlinear least squares method for material characterization using elastic waves, Computer Methods in Applied Mechanics and Engineering 191 (2002) 1909–1921.

[8] J. R. McCusker, K. Danai, Selection of Outputs for Gas-Turbine Engines by Parameter Signatures ASME 2010 Dynamic Systems and Control Conference, Volume 2 (2010) 239–246. doi:10.1115/DSCC2010-4148.

[9] J. L.Kerrebrock, Aircraft Engines and Gas Turbines, 2nd Edition, MIT Press, Cambridge - Massachusetts, 1992, Ch. Chapter 3.

[10] R. D. Flack, Fundamental of Jet Propulsion with Applications, 1st Edition, Cambridge University Press, New Yor, 2005, Ch. Chapter 9.

[11] EASA, Type certificate data sheet for trent 1000 engines series, https://www.easa.europa.eu/en/downloads/7733/en, (2022).

[12] ICAO, Icao aircraft engine emissions databank, https://www.easa.europa.eu/en/domains/environment/icao-aircraft-engine-emissions-databank (2021).

[13] I. Asoliman, M. Ehab, A. Mahrous, A. El-Sayed, M. Emeara, Performance analysis of high bypass turbofan engine trent 1000-a *, 2018.

[14] A. Pourrajabian, R. Ebrahimi, M. Mirzaei, M. Shams, Applying genetic algorithms for solving nonlinear algebraic equations, Applied Mathematics and Computation 219 (24) (2013) 11483–11494. doi:10.1016/j.amc.2013.05.057.

[15] A. M. . U. M. Mangla, C., Optimization of complex nonlinear systems using genetic algorithm, Int. j. inf. tecnol. 13 (2021) 1913–1925. doi:10.1007/s41870-020-00421-z.

[16] Z. Wu, L. Kang, A fast and elitist parallel evolutionary algorithm for solving systems of non-linear equations, in: The 2003 Congress on Evolutionary Computation, 2003. CEC '03., Vol. 2, 2003, pp. 1026–1028 Vol.2. doi:10.1109/CEC.2003.1299780.

[17] Y. Yu, L. Chen, F. Sun, C. Wu, Neural-network based analysis and prediction of a compressor's characteristic performance map, Applied Energy 84 (1) (2007) 48–55. doi:10.1016/j.apenergy.2006.04.005.

[18] M. Gholamrezaei, K. Ghorbanian, Compressor map generation using a feed-forward neural network and rig data, Proceedings of The Institution of Mechanical Engineers Part A-journal of Power and Energy - PROC INST MECH ENG A-J POWER 224 (2010) 97–108. doi:10.1243/09576509JPE792.

[19] Matlab Manual, Ga function, `https://www.mathworks.com/help/gads/ga.html` (2022).

[20] A. Rexhepi, A. Maxhuni, A. Dika, Analysis of the impact of parameters values on the genetic algorithm for tsp, International Journal of Computer Science Issues Volume 10 (2013) pp 158–164.

[21] Matlab Manual, lsqnonlin function, `https://www.mathworks.com/help/optim/ug/lsqnonlin.html` (2022).

[22] GasTurb 13, Design and Off-Design Performance of Gas Turbines, `https://www.gasturb.com/Downloads/Manuals/GasTurb13.pdf`.

[23] A. Joksimović, S. Duplaa, y. bousquet, X. Carbonneau, N. Tantot, Local and global analysis of a variable pitch fan turbofan engine, 2017. doi:10.29008/ETC2017-073.

[24] R. Mazzawy, Performance study for the benefits of a variable pitch composite fan, 2010. doi:10.1115/GT2010-22148.

[25] Mechanical Design of a Variable Pitch Fan for Turbofan Engines, Vol. Volume 1: Aircraft Engine; Ceramics; Coal, Biomass and Alternative Fuels; Education; Electric Power; Manufacturing Materials and Metallurgy of Turbo Expo: Power for Land, Sea, and Air. doi:10.1115/GT2010-22969.

[26] R. Mazzawy, J. Virkler, Variable pitch fan - the solution to achieving high propulsive efficiency turbofan engines, 2009. doi:10.4271/2009-01-3103.

[27] S.-G. L. *et al.*, Numerical study on the effect of the tip clearance of a 100 hp axial fan on the aerodynamic performance and unsteady stall characteristics, Journal of Mechanical Science and Technology 34 (2020) 5117–5137. doi:10.1007/s12206-020-1115-2.

[28] S. Liu, Y. Guo, Y. Zhang, C. Gu, L. Yang, Effects of tip clearance and impeller eccentricity on the aerodynamic performance of mixed flow fan, Symmetry 15 (1) (2023). doi:10.3390/sym15010201.

[29] W. W. Copenhaver, E. R. Mayhew, C. Hah, A. R. Wadia, The effect of tip clearance on a swept transonic compressor rotor, Journal of Turbomachinery 118 (2) (1996) 230–239. doi:10.1115/1.2836630.

[30] J. Large, A. Pesyridis, Investigation of micro gas turbine systems for high speed long loiter tactical unmanned air systems, Aerospace 6 (5) (2019). doi:10.3390/aerospace6050055.

[31] D. Nark, E. Envia, C. Burley, On Acoustic Source Specification for Rotor-Stator Interaction Noise Prediction. doi:10.2514/6.2010-3713.

[32] École Centrale de Lyon, Catana project (2020).
URL http://catana.ec-lyon.fr/

[33] V. Pagès, P. Duquesne, S. Aubert, L. Blanc, P. Ferrand, X. Ottavy, C. Brandstetter, Uhbr open-test-case fan ecl5/catana, International Journal of Turbomachinery, Propulsion and Power 7 (2) (2022). doi:10.3390/ijtpp7020017.

[34] Cenaero, Rotor 67 cad geometry.
URL https://how4.cenaero.be/content/c2-nasa-rotor-67

[35] A. S. *et al.*, Laser anemometer measurements in atransonic axial-flow fan rotor, NASA Technical Paper 2879 (1989).
URL https://ntrs.nasa.gov/citations/19900001929

[36] B. Xinyu, Cfd validation of nasa stage 67 with a rotor wake modelling approach and an unequal periodic boundary treatment, PhD Thesis (2023).

[37] M. Hathaway, Unsteady flows in a single-stage transonic axial-flow fan stator row (01 1987).

[38] N. Yilmaz, Comparative energy and environmental assessment of battery technologies and alternative fuels in sustainable aviation, International Journal of Green Energy 0 (0) (2022) 1–10. doi:10.1080/15435075.2022.2075226.

[39] T. Schripp, F. Herrmann, P. Oßwald, M. Köhler, A. Zschocke, D. Weigelt, M. Mroch, C. Werner-Spatz, Particle emissions of two unblended alternative jet fuels in a full scale jet engine, Fuel 256 (2019) 115903. doi:10.1016/j.fuel.2019.115903.

[40] R. Moore, *et al.*, Biofuel blending reduces particle emissions from aircraft engines at cruise conditions, Nature 543 (2017) 411–415. doi:10.1038/nature21420.

[41] T. L. Anna L. Oldani, Alexandra E. Solecki, Evaluation of physicochemical variability of sustainable aviation fuels, Frontiers in Energy Research 10 (2022). doi:10.3389/fenrg.2022.1052267.

[42] V. Calemma, C. Gambaro, W. O. Parker, R. Carbone, R. Giardino, P. Scorletti, Middle distillates from hydrocracking of ft waxes: Composition, characteristics and emission properties, Catalysis Today 149 (1) (2010) 40–46, international Symposium on Catalysis for Ultra-Clean Fuels, Dalian, China, July 21-24, 2008. doi:10.1016/j.cattod.2009.03.018.

[43] E. Furimsky, Hydroprocessing challenges in biofuels production, Catalysis Today 217 (2013) 13–56. doi:10.1016/j.cattod.2012.11.008.

[44] J. Yang, C. Caldwell, K. Corscadden, Q. S. He, J. Li, An evaluation of biodiesel production from camelina sativa grown in nova scotia, Industrial Crops and Products 81 (2016) 162–168. doi:10.1016/j.indcrop.2015.11.073.

[45] X. Zhang, K. K. Yalamanchi, S. M. Sarathy, A functional-group-based approach to modeling real-fuel combustion chemistry – i: Prediction of stoichiometric parameters for lumped pyrolysis reactions, Combustion and Flame 227 (2021) 497–509. doi:10.1016/j.combustflame.2020.10.038.

[46] X. Zhang, S. M. Sarathy, A functional-group-based approach to modeling real-fuel combustion chemistry – ii: Kinetic model construction and validation, Combustion and Flame 227 (2021) 510–525. doi:10.1016/j.combustflame.2020.10.039.

[47] Y. Li, C.-W. Zhou, K. P. Somers, K. Zhang, H. J. Curran, The oxidation of 2-butene: A high pressure ignition delay, kinetic modeling study and reactivity comparison with isobutene and 1-butene, Proceedings of the Combustion Institute 36 (1) (2017) 403–411. doi:10.1016/j.proci.2016.05.052.

[48] C.-W. Zhou, *et al.*, An experimental and chemical kinetic modeling study of 1,3-butadiene combustion: Ignition delay time and laminar flame speed measurements, Combustion and Flame 197 (2018) 423–438. doi:10.1016/j.combustflame.2018.08.006.

[49] H. Wang, X. You, A. Joshi, S. Davis, A. Laskin, F. Egolfopoulos, C. Law, High-temperature combustion reaction model of h2/co/c1-c4 compounds, USC Mech version II (2007).
URL `http://ignis.usc.edu/USC_Mech_II.htm`

[50] S. D. C. Department of Mechanical and Aerospace Engineering, Univ. of California, Chemical-kinetic mechanisms for combustion applications (accessed on May 2024).
URL `http://web.eng.ucsd.edu/mae/groups/combustion/mechanism.html`

[51] C. R. Zhou, K. Sendt, B. S. Haynes, Experimental and kinetic modelling study of h2s oxidation, Proceedings of the Combustion Institute 34 (1) (2013) 625–632. doi:10.1016/j.proci.2012.05.083.

[52] C. G. Moniruzzaman, F. Yu, A 0d aircraft engine emission model with detailed chemistry and soot microphysics, Combustion and Flame 159 (4) (2012) 1670–1686. doi:10.1016/j.combustflame.2011.11.006.

[53] J. Bisson, P. Seers, M. Huegel, F. Garnier, Numerical prediction of gaseous aerosol precursors and particles in an aircraft engine, Journal of Propulsion and Power 32 (4) (2016) 918–928. doi:10.2514/1.B35943.

[54] Ansys, Ansys chemkin-pro getting started guide 1 (2022) 118–119.

[55] Ansys, Ansys chemkin input manual 1 (2023).

[56] S. K. Muduli, R. K. Mishra, P. C. Mishra, Computational assessment of performance parameters of an aero gas turbine combustor for full flight envelope operation, International Journal of Turbo Jet-Engines 40 (4) (2023) 481–491. doi:10.1515/tjj-2021-0034.

[57] J. D. Oliveira, Cfd analysis of the combustion of bio-derived fuels in the cfm56-3 combustor, Thesis, Universidade da Beira Interior, Engenharia (2016).
URL https://ubibliorum.ubi.pt/bitstream/10400.6/6527/1/4691_9311.pdf

[58] J. B. Heywood, T. Mikus, Parameters controlling nitric oxide emissions from gas turbine combustors, AGARD Propulsion and Energetics Panel 41st Meeting on "Atmospheric Pollution by Aircraft Engines", London, England, 1973.

[59] C. Wey, *et al.*, Aircraft particle emissions experiment (apex), NASA thecnical report (2006) 531.
URL https://ntrs.nasa.gov/citations/20060046626

[60] GSP Development Team members, Gsp 12 user manual (accessed on May 2024).
URL https://www.gspteam.com/GSPsupport/OnlineHelp/index.html?documentation.htm

[61] W. Visser, Generic analysis methods for gas turbine engine performance: The development of the gas turbine simulation program gsp, Ph.D. thesis, TU Delft, https://doi.org/10.4233/uuid:f95da308-e7ef-47de-abf2-aedbfa30cf63 (2015).

[62] R. Xu, H. Wang, M. Colket, T. Edwards, Thermochemical properties of jet fuels, Stanford University (2015) 23.
URL https://web.stanford.edu/group/haiwanglab/HyChem/approach/Report_Jet_Fuel_Thermochemical_Properties_v6.pdf

[63] G. B. Bessee, S. A. Hutzler, G. R. Wilson, Propulsion and power rapid response research and development (rd) support, Interim Report Air Force Research Laboratory propulsion directorate Wright-Patterson Air Force Base (2011) 251.
URL https://apps.dtic.mil/sti/citations/ADA547232

[64] US-Environmental-Protection-Agency, Method 8260b volatile organic compounds by gas chromatography/mass spectrometry (gc/ms) (accessed on May 2024).
URL https://19january2017snapshot.epa.gov/sites/production/files/2015-12/documents/8260b.pdf

[65] US-Environmental-Protection-Agency,

[66] A. G. Abdul Jameel, N. Naser, A.-H. Emwas, S. Dooley, S. M. Sarathy, Predicting fuel ignition quality using 1h nmr spectroscopy and multiple linear regression, Energy & Fuels 30 (11) (2016) 9819–9835. doi:10.1021/acs.energyfuels.6b01690.

[67] C. Shao, Q. Wang, W. Zhang, *et al.*, Elucidating the polycyclic aromatic hydrocarbons involved in soot inception, Communications Chemistry 6 (223) (2023). doi:10.1038/s42004-023-01017-x.

[68] S. J. Klippenstein, J. A. Miller, From the time-dependent, multiple-well master equation to phenomenological rate coefficients, The Journal of Physical Chemistry A 106 (40) (2002) 9267–9277. doi:10.1021/jp021175t.

[69] M. Frenklach, R. I. Singh, A. M. Mebel, On the low-temperature limit of haca, Proceedings of the Combustion Institute 37 (1) (2019) 969–976. doi:10.1016/j.proci.2018.05.068.

[70] T. Malewicki, S. Gudiyella, K. Brezinsky, Experimental and modeling study on the oxidation of jet a and the n-dodecane/iso-octane/n-propylbenzene/1,3,5-trimethylbenzene surrogate fuel, Combustion and Flame 160 (1) (2013) 17–30. doi:10.1016/j.combustflame.2012.09.013.

[71] J. Guo, P. Liu, E. Quadarella, K. Yalamanchi, I. Alsheikh, C. Chu, F. Liu, S. M. Sarathy, W. L. Roberts, H. G. Im, Assessment of physical soot inception model in normal and inverse laminar diffusion flames, Combustion and Flame 246 (2022) 112420. doi:10.1016/j.combustflame.2022.112420.

[72] J. Appel, H. Bockhorn, M. Frenklach, Kinetic modeling of soot formation with detailed chemistry and physics: laminar premixed flames of c2 hydrocarbons, Combustion and Flame 121 (1) (2000) 122–136. doi:10.1016/S0010-2180(99)00135-2.

[73] G. Lombardo, P. Lo Greco, I. Benedetti, Turbofan performance estimation using neural network component maps and genetic algorithm-least squares solvers, International Journal of Turbomachinery, Propulsion and Power 9 (3) (2024). doi:10.3390/ijtpp9030027.

[74] J. L.Kerrebrock, Aircraft Engines and Gas Turbines, 2nd Edition, MIT Press, Cambridge - Massachusetts, 1992, Ch. Chapter 3.

[75] D. Burrus, P. E. Sabla, D. W. Bahr, Energy efficient engine component development and integration: Single-annular combustor technology report, NASA Lewis Research Center, Cleveland, OH (1980) 118.
URL https://ntrs.nasa.gov/citations/19900019252

[76] M. Foust, D. Thomsen, R. Stickles, C. Cooper, W. Dodds, Development of the GE Aviation Low Emissions TAPS Combustor for Next Generation Aircraft Engines, 2012. doi:10.2514/6.2012-936.

[77] C. Gong, S. Zhao, W. Chen, W. Li, Y. Zhou, M. Qiu, Numerical study on the combustion process in a gas turbine combustor with different reference velocities, Advances in Aerodynamics 5 (1) (2023) 24. doi:10.1186/s42774-023-00154-0.

[78] EASA, Type-certificate data sheet for cfm56-2 cfm56-3 series engines (2023).
URL https://www.easa.europa.eu/en/downloads/7691/en

[79] R. Busen, M. Kuhn, A. Petzold, F. Schroeder, U. Schumann, D. Baumgardner, S. Borrmann, D. Hagen, P. Whitefield, J. Stroem, Experiments on contrail formation from fuels with different sulfur content, International colloquium: Impact of aircraft emissions upon the atmosphere, France (1997).
URL https://www.osti.gov/etdeweb/biblio/623593

[80] ICAO, Presentation of 2019 air transport statistical results, https://www.icao.int/annual-report-2019/Documents/ARC_2019_Air%20Transport%20Statistics.pdf (2020).

[81] IATA, Global outlook for air transport deep change, https://www.iata.org/en/iata-repository/publications/economic-reports/global-outlook-for-air-transport-june-2024-report/ (2024).

[82] D. Lee, D. Fahey, A. Skowron, M. Allen, U. Burkhardt, Q. Chen, S. Doherty, S. Freeman, P. Forster, J. Fuglestvedt, A. Gettelman, R. De León, L. Lim, M. Lund, R. Millar, B. Owen, J. Penner, G. Pitari, M. Prather, R. Sausen, L. Wilcox, The contribution of global aviation to anthropogenic climate forcing for 2000 to 2018, Atmospheric Environment 244 (2021) 117834. doi:10.1016/j.atmosenv.2020.117834.

[83] A. Innocenti, A. Andreini, D. Bertini, B. Facchini, M. Motta, Turbulent flow-field effects in a hybrid cfd-crn model for the prediction of nox and co emissions in aero-engine combustors, Fuel 215 (2018) 853–864. doi:10.1016/j.fuel.2017.11.097.

[84] T. H. Nguyen, Improved chemical reactor network application for predicting the emission of nitrogen oxides in a lean premixed gas turbine combustor, Combustion, Explosion, and Shock Wave 55 (2019) 267. doi:10.1134/S0010508219030031.

[85] F. Grimm, Low-order reactor-network-based prediction of pollutant emissions applied to flox® combustion, Energies 15 (5) (2022). doi:10.3390/en15051740.

[86] A. Åkerblom, C. Fureby, Les modeling of the dlr generic single-cup spray combustor: Validation and the impact of combustion chemistry, Flow, Turbulence and Combustion 112 (2024) 557. doi:10.1007/s10494-023-00512-4.

[87] T. Malewicki, S. Gudiyella, K. Brezinsky, Experimental and modeling study on the oxidation of jet a and the n-dodecane/iso-octane/n-propylbenzene/1,3,5-trimethylbenzene surrogate fuel, Combustion and Flame 160 (1) (2013) 17–30. doi:10.1016/j.combustflame.2012.09.013.

[88] Ansys, CAD Integration, r2 Edition, 2024, Ch. 121-126.

[89] L. Jiang, Rans modelling of turbulence in combustors, in: K. Volkov (Ed.), Turbulence Modelling Approaches, IntechOpen, Rijeka, 2017, Ch. 7. doi:10.5772/intechopen.68361.

[90] Ansys, Ansys Fluent User's Guide, r1 Edition, 2022.

[91] C. S. C. R. e. a. Shanmugadas, K.P., Characterization of wall filming and atomization inside a gas-turbine swirl injector, Experiments in Fluids 59 (10) (2018) 151. doi:10.1007/s00348-018-2606-0.

[92] S. McAllister, J.-Y. Chen, A. C. Fernandez-Pello, DropletEvaporationandCombustion, Ch. 8, p. 304. doi:10.1007/978-1-4419-7943-8.

[93] H. Y. Wang, V. G. McDonell, S. Samuelsen, Influence of Hardware Design on the Flow Field Structures and the Patterns of Droplet Dispersion: Part I—Mean Quantities, Journal of Engineering for Gas Turbines and Power 117 (2) (1995) 282–289. doi:10.1115/1.2814092.

[94] A. A. Rizkalla, A. H. Lefebvre, The influence of air and liquid properties on airblast atomization, Journal of Fluids Engineering 97 (3) (1975) 316–320. doi:10.1115/1.3447309.

[95] Analysis and Comparison of Primary Droplet Characteristics in the Near Field of a Prefilming Airblast Atomizer, Vol. Volume 1A: Combustion, Fuels and Emissions of Turbo Expo: Power for Land, Sea, and Air. doi:10.1115/GT2013-94033.

[96] L.-P. Hsiang, G. Faeth, Near-limit drop deformation and secondary breakup, International Journal of Multiphase Flow 18 (5) (1992) 635–652. doi:10.1016/0301-9322(92)90036-G.

[97] Q. P. Zheng, A. K. Jasuja, A. H. Lefebvre, Structure of airblast sprays under high ambient pressure conditions, Journal of Engineering for Gas Turbines and Power 119 (3) (1997) 512–518. doi:10.1115/1.2817014.

[98] M. El-Shanawany, A. Lefebvre, Airblast atomization: Effect of linear scale on mean drop size, Journal of Energy 4 (4) (1980) 184–189. doi:10.2514/3.62472.

[99] H. WANG, V. MCDONELL, G. SAMUELSEN, The influence of spray angle on the continuous- and discrete-phase flowfield downstream of an engine combustor swirl cup. doi:10.2514/6.1992-3231.

[100] H. WANG, V. MCDONELL, W. SOWA, G. SAMUELSEN, Characterization of a two-phase flow field downstream of a 3x-scale gas turbine co-axial, counter-swirling, combustor dome swirl cup. doi:10.2514/6.1992-229.

[101] H. Wang, V. G. McDonell, W. A. Sowa, S. Samuelsen, Experimental study of a model gas turbine combustor swirl cup, part ii: Droplet dynamics, Journal of Propulsion and Power 10 (4) (1994) 446–452. doi:10.2514/3.51391.

[102] H. Wang, X. You, A. V. Joshi, S. G. Davis, A. Laskin, F. Egolfopoulos, C. K. Law, Usc mech version ii. high-temperature combustion reaction model of h2/co/c1-c4 compounds (2007).
URL `http://ignis.usc.edu/USC_Mech_II.htm`

[103] H. G. G. Lammel, Greenhouse effect of nox, Environ. Sci. Pollut. Res. 2 (1995) 40–45. doi:10.1007/BF02987512.

[104] M. A. Pacheco, E. E. Petersen, On a general correlation for catalyst fouling, Journal of Catalysis 86 (1) (1984) 75–83. doi:10.1016/0021-9517(84)90349-X.

[105] Y. Liu, X. Sun, V. Sethi, D. Nalianda, Y.-G. Li, L. Wang, Review of modern low emissions combustion technologies for aero gas turbine engines, Progress in Aerospace Sciences 94 (2017) 12–45. doi:10.1016/j.paerosci.2017.08.001.

[106] P. Prashanth, R. L. Speth, S. D. Eastham, J. S. Sabnis, S. R. H. Barrett, Post-combustion emissions control in aero-gas turbine engines, Energy Environ. Sci. 14 (2021) 916–930. doi:10.1039/D0EE02362K.

[107] A. Blinov, N. Malastowski, L. Myagkov, Development of the model for a diesel engine catalytic converter, E3S Web of Conferences 140 (2019) 06013. doi:10.1051/e3sconf/201914006013.

[108] D. Kim, C. Lee, Scr performance evaluations in relation to experimental parameters in a marine generator engine, Journal of Marine Science and Engineering 7 (2019) 67. doi:10.3390/jmse7030067.

[109] A. Pant, S. J. Schmieg, Kinetic model of nox scr using urea on commercial cuzeolite catalyst, Industrial & Engineering Chemistry Research 50 (9) (2011) 5490–5498. doi:10.1021/ie200060s.

[110] L. Olsson, H. Sjövall, R. J. Blint, A kinetic model for ammonia selective catalytic reduction over cu-zsm-5, Applied Catalysis B: Environmental 81 (3) (2008) 203–217. doi:10.1016/j.apcatb.2007.12.011.

[111] Ansys Fluent, Help System, Modeling species transport and finite-rate chemistry, , Inc. (ANSYS).

[112] Ansys Fluent, Help System, Porous media conditions, , Inc. (ANSYS).

[113] S. Dammalapati, P. Aghalayam, N. Kaisare, Modeling the effect of nonuniformities from urea injection on scr performance using cfd, Industrial & Engineering Chemistry Research 58 (44) (2019) 20247–20258. doi:10.1021/acs.iecr.9b04149.

[114] F. Greifzu, C. Friebe, M. Heinrich, R. Schwarze, Cfd-simulation of isothermal turbomachinery - a comparison of results from ansys fluent and openfoam, 2014. doi:10.1115/GT2014-26338.

[115] F. Ekström, B. Andersson, Pressure drop of monolithic catalytic converters experiments and modeling, SAE Transactions 111 (2002) 425–433.
URL http://www.jstor.org/stable/44734532

[116] J. Dill, G. Samuelsen, Evaluation of selective non-catalytic reduction of nox for jet engine test cells, UCI Combustion Laboratory (1995).

[117] K. Kadoya, N. Matsunaga, A. Nagashima, Viscosity and thermal conductivity of dry air in the gaseous phase, Journal of Physical and Chemical Reference Data 14 (4) (1985) 947–970. doi:10.1063/1.555744.

[118] Cheryl L. Bowman and Ty V. Marien and James L. Felder, Turbo- and hybrid-electrified aircraft propulsion for commercial transport, aIAA/IEEE Electric Aircraft Technologies Symposium, https://doi.org/10.2514/6.2018-4984 (2018).